Elucidating Buried Interfacial Structures Of Complex Materials Using Advanced Spectroscopic And Microscopic Techniques

by

Minyu Xiao

A dissertation submitted in partial fulfillment
of the requirements for the degree of
Doctor of Philosophy
(Chemistry)
in the University of Michigan
2018

Doctoral Committee:

Professor Zhan Chen, Chair
Professor Jay L. Guo
Professor Stephen Maldonado
Professor Anne J. McNeil

myxiao@umich.edu
ORCID iD: 0000-0003-0083-4243
2018

DEDICATION

To my family

ACKNOWLEDGEMENTS

I would first like to sincerely thank my Ph.D. advisor Prof. Zhan Chen. My past five years in at Michigan is nothing but a fantastic journey. From Prof. Chen, I learned not only how to become an efficient and independent researcher in the field of chemistry, but also how to truly embrace and digest failures. The amount of freedom and support I got from Prof. Chen is just incredible: he would always support any new ideas I came across, no matter if it's good or bad, he would sit down and discuss the problems with me whenever I felt lost, and he would also direct me to external resources outside our lab if I need special experiments to be done. I still remember couple month ago when I received my job offer from management consulting industry, it was him who encouraged me to accept the offer and embrace the change. Looking back now before my graduation, no words can describe how lucky I was to have made the decision to join Prof. Chen's lab.

Secondly, I want to thank all my friends and lab fellows. I still remember how much I learned from senior lab members when I joined the lab in 2014. Especially Dr. Chi Zhang and Dr. Joshua Jasensky, you two were the first two senior lab member I came across and you two really set a high standard and expectation for me from day one. I also like to thank Dr. Xiaoxian Zhang for her extraordinary knowledge in semiconductors, a lot of my problems wouldn't have been so

easily resolved without your help. I also want to thank Dr. Lauren Soblosky, Dr. Jeanne Hankett, Dr. Chuan Leng, Dr. John Myers, Dr. Yaoxin Li, Dr. Pei Yang, Dr. Xinquan Zou and Nathan Ulrich for all your help and insightful discussion in the past five years.

Thirdly, I also want to thank Prof. Stephen Maldonado, Prof. Anne J. McNeil and Prof. Jay L. Guo for being my thesis committee members. An important thanks to Prof. McNeil and Prof. Guo who provided help and guidance to my research. I also want to thank department of chemistry for providing me departmental fellowships for two summers and one spring semester.

Finally, I would like to thank my family and my beloved girlfriend: my mother Dr. Yunfeng Xuan, my father Prof. Shoujun Xiao and my girlfriend Xuefei Zhang. Mom and dad, I finally will become the last doctor in our family! It was you two who showed me the beauty of chemistry, taught me the excitement of discover unknowns, and supported me on all the choices I made in my life. My mother Dr. Yunfeng Xuan obtained her Ph.D. degree after she started working, her personal experience taught nothing is impossible if I'm willing to try hard. My father Prof. Shoujun Xiao often criticized my research, but I know it's just his harsh love :) Just like how an old saying goes: no pain, no gain. To Xuefei Zhang, my beloved girlfriend: words can't describe how happy I was when you decided to come Michigan for your Ph.D. study three years ago. Ann Arbor witnessed so much of our happiness, and I knew you would always be the one that support me and cheer me up whenever I came across difficulties and pressure.

Minyu Xiao

03/14/2018

TABLE OF CONTENTS

LIST OF FIGURES

LIST OF TABLES

ABSTRACT

Modern electronic devices are engineered to be compact, many device functions are often encapsulated into multiple layers within one thin device. Such technological advance trend creates multiple buried interfaces between different layers in single electronic device. Optimizing overall device function and lifetime often relies on understanding each layer independently, however approaches used to understand such buried interfaces nondestructively are still lacking, making it intrinsically difficult to perform failure analysis on many devices to fully understand the device failure mechanisms. This thesis combines an interface sensitive technique, sum frequency generation (SFG) vibrational spectroscopy, with various other analytical techniques to elucidate interfacial structure-function correlations related to complex electronic devices and systems.

By studying the surface structure and behavior of organic semiconductor (Poly 3-hexyl thiophene, P3HT) thin films prepared using different solvents, it was found that the P3HT molecules at the polymer/air interface would lie down as more acetone was added into the casting solvent, demonstrating the feasibility of varying semiconductor thin film surface structure by altering the solvent composition for thin film preparation. SFG research also elucidated how the properties of the underneath substrate and semiconductor polymer sidechain could affect the

orientation of polythiophene at the polymer/air and polymer/substrate interface of a thin polythiophene film. This research provided systematic understanding of the effects of sample preparation solvent, substrate hydrophobicity, and polymer side chain composition on the surface and buried interfacial structures of semiconductor polymer thin films.

SFG has also been applied to study interfacial structures of semiconductor polymer thin films in photovoltaics: the interfacial orientations of polythiophene molecules at the perovskite/polythiophene hole transport layer interface were successfully correlated to the overall perovskite device power conversion efficiency. The experimental results indicated that subtle of the tilt angle of the polythiophene backbone at the perovskite/polythiophene interface could lead to over 100% difference on device efficiency. This example demonstrated that the understanding of the interfacial structure of a semiconductor thin film could improve the property of photovoltaic device.

SFG has also been used to probe the molecular structures of buried interfaces of polymer-based adhesives to understand the structure-function correlations of such polymer adhesives for microelectronics packaging. In this study, pristine polyethylene and grafted polyethylene were examined. It was found that ordered C=O grafted groups and standing up methylene group at buried polymer adhesive interface could lead to better adhesion strength for polyethylenes.

This thesis also developed a microscopic-SFG platform which can collect SFG spectrum and obtain optical/fluorescence image simultaneously from the same sample. With this analytical platform, molecular interactions between biological molecules and 2D material MoS_2 were revealed. This research developed a generally applicable approach to design the sequence of a peptide with a preferred orientation on MoS_2. The microscope-SFG platform was also used to study the bacterial killing mechanism of surface-immobilized antimicrobial peptides *via* covalent

attachment. SFG was used to monitor the structural change of these peptides upon interacting with bacteria, and the microscope was used to collect the live/dead bacterial information on the surface *in situ* with fluorescence image, demonstrating the feasibility to probe structure and function of interfacial biological molecules simultaneously.

Overall, this thesis developed important approaches using SFG to study buried interfaces related to electronics. Such approaches are general and can be applied to study complex interfaces to understand their structure-function correlations, providing important knowledge for constructing interfaces with improved properties.

CHAPTER 1 Introduction

1.1. Motivation

Surface and buried interfacial structure of matters has long been an important topic to researchers because of its scientific importance. To name a few, interfacial structure of semiconductors and photovoltaics has become increasingly important due to the multi-layer thin film architecture of the fabricated devices; interfacial structure of organic adhesives has been shown to be one of the dominant factors to affect adhesion strength, and surface property of single-layered 2-dimentional (2D) materials could greatly mediate the electric property of those materials. However, surfaces and interfaces usually only involve very small amount of materials, and many interfaces are buried, therefore their structures are extremely difficult to study. Analytical techniques have been developed to probe interfacial structures, such attenuated total reflectance infrared spectroscopy (ATR-FTIR), grazing incidence X-ray diffraction (GIXRD) etc. But many of these techniques could not provide monolayer surface/interfacial sensitivity, and could not probe buried interfaces.

Vibration spectroscopy is known for its noninvasive character and chemical specificity, providing molecular insight into various sample systems. As high-power pulse laser technique and nonlinear optical instrumentation have been developed, nonlinear vibrational spectroscopies were found to be an ideal analytical platform to study surface and interface properties of various sample systems. One advantage nonlinear vibrational spectroscopies process is the intrinsic surface sensitivity (second order nonlinear effects). The research in this thesis covers Sum Frequency Generation (SFG) vibrational spectroscopic studies on surface and interfacial structures and their correlations to properties of organic semiconductors and photovoltaics, polymer-based adhesives, interfacial biological molecules and 2D materials.

Surface, bulk, and interfacial structures of organic semiconductors all play vital roles in their performance for many important applications, including organic field effect transistors (OFETs),[1-3] organic photovoltaics (OPVs),[4-6] and organic light emitting diodes (OLEDs).[7] In OFET, it has been reported that an edge-on backbone structure in the film bulk results in an increase in hole conduction and therefore leads to a higher hole-mobility.[2,8] In OPV, it has been reported that interfacial molecular orientation can affect interfacial charge transport efficiency. While in OLED, the molecular orientation alters the ratio between air-mode and plasma-mode emission profile.[1,7,9,10] Device performance issues often arise from the relatively low conductive nature of organic materials (due to unfavorable molecular orientations), where charge tends to accumulate at the surface/interface of thin organic films. Therefore, it is important to carefully design polymer chemical structure and control the surface/interface structures of such thin films. However, such an objective is challenging due to the difficultly in controlling the surface/interfacial structure of an organic semiconducting thin film, and it is also difficult to model, characterize, and quantify such a structure at a molecular level due to the lack of proper analytical

techniques. Many applicable and widely used characterization methods for these thin film materials have some disadvantages: Transmission electron microscope (TEM) requires a relatively complicated sample preparation procedure and cannot probe a buried interface; scanning electron microscope (SEM) and atomic force microscope (AFM) only provide information of surface morphology and lack the ability to characterize chemical or electronic structures; and X-ray diffraction provides structural information of the bulk material, not the surface or interface. Furthermore, the X-ray diffraction signal from such thin films is usually too weak to provide concrete information because such films normally lack crystallinity. In this thesis, SFG will be applied to study surfaces and interfaces of semiconductor polymer thin films, providing important knowledge for the field of organic semiconductors and photovoltaics.

Adhesives, especially polymer-based adhesives, have broad applications. Adhesives exist almost in every aspect of our daily life, from food packing to automobiles, from furniture to cellphone packaging. Adhesives often fail because of effects of temperature, humidity, or aging; therefore, understanding interfacial structure-function correlation is extremely important because the majority of the adhesion failure happened at interfaces. This thesis research examined the molecular structures of buried interfaces in situ and found structure-function relations of such interfaces, providing in-depth understanding on adhesion.

Interfacial structures of biological molecules such as peptides and proteins determine their functions. Peptides physically adsorbed and chemically immobilized on surfaces have been widely used for biosensing and antimicrobial coating. This research investigate peptides physically adsorbed on 2D materials and interactions between surface immobilized peptides and live bacteria. In such studies, SFG spectroscopy was applied in combination of an optical/fluorescence

microscope. Such studies demonstrated the successful investigations of molecular structures of heterogenous interfaces and simultaneous study of structure-function relations of interfacial biological molecules.

1.2. Sum Frequency Generation (SFG) Vibrational Spectroscopy

1.2.1. SFG Background

SFG is a second-order nonlinear optical process where two photons are combined to generate a third photon that sums the energy of the two incoming photons. The selection rule of SFG dictates that this photon combining process can only occur in a medium which lacks inversion symmetry. Most bulk media have inversion symmetry, therefore no SFG signal can be generated. For surfaces and interfaces, inversion symmetry is broken, thus the SFG process can occur allowing for SFG spectroscopy to be an intrinsic surface/interface specific technique. In our SFG vibrational spectroscopic studies, the two incoming beams include a visible (532 nm) beam and a frequency tunable infrared (IR) beam. By tuning the IR beam frequency, one can selectively probe various functional groups on a surface or at an interface. Determination of the molecular orientation of such functional groups is achieved by controlling the polarization of each incoming beam as well as the generated SFG beam. Recent progress in SFG research has shown that SFG is a powerful tool to investigate surfaces and interfaces of many systems such as biological systems,[11-16] organic molecules,[17,18] water,[14,19-24] as well as organic semiconductor materials.[2,3,25-29] A schematic of SFG experimental setup and energy diagram of an SFG process is shown in Figure 1-1.

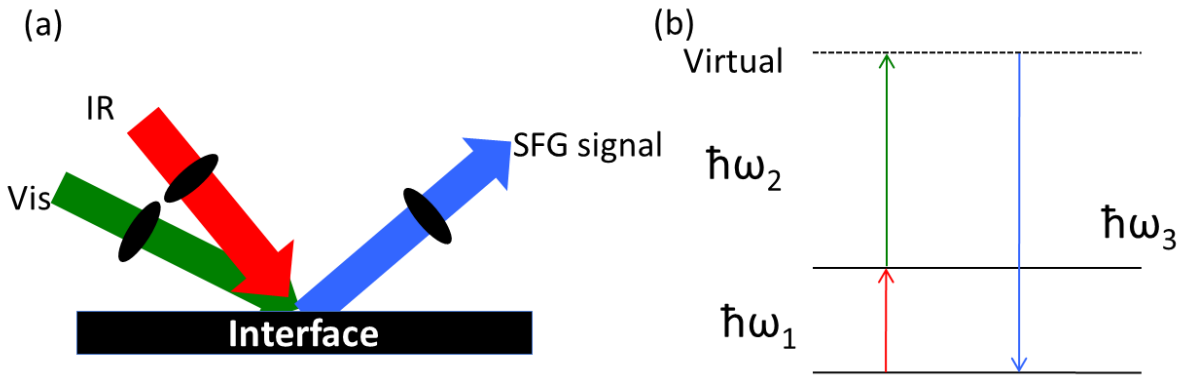

Figure 1-1 Schematic of SFG experimental setup and energy diagram

1.2.2. Basic SFG Theory

SFG theory, data interpretation, and surface selectivity have been extensively published previously.[30-39] Briefly, SFG output intensity can be expressed as:

$$I_{SFG} \propto \left|\chi_{eff}^{(2)}\right|^2 I_{IR} I_{vis} \tag{1-1}$$

where I_{IR} and I_{vis} are the input IR and visible beam intensities. $\chi_{eff}^{(2)}$ is the effective second-order nonlinear optical susceptibility of the surface/interface, expressed as:

$$\chi_{eff}^{(2)} = \chi_{NR}^{(2)} + \sum_q \frac{A_q}{\omega_{IR} - \omega_q + i\Gamma_q} \tag{1-2}$$

$\chi_{NR}^{(2)}$ is the nonresonant contribution from the sample. The resonant part of equation 1-2 can be fitted as a sum of Lorentzian peaks with a peak strength of A_q, frequency of ω_q, and a peak width of Γ_q for the peak q. All the SFG spectra in this paper are fitted with equation 1-2. $\chi_{eff}^{(2)}$ is the effective second-order nonlinear susceptibility tensor of the sample (e.g., a surface or an interface),

which is correlated to the second-order nonlinear susceptibility tensor $\chi^{(2)}$ defined in the lab fixed coordinate system. Therefore, different tensor components of $\chi^{(2)}$ can be deduced from different components of $\chi^{(2)}_{eff}$. To do so, it is necessary to measure different components of $\chi^{(2)}_{eff}$ using different output/input beam polarization combinations in the SFG experiment. In this thesis, the incident angles of the input visible and IR beams are 60° and 55° versus the surface normal unless otherwise advised.

1.2.3. Analysis of SFG contribution from multiple interfaces

SFG signal collected from a thin film on a solid substrate may originate from both the surface in air and the buried film/substrate interface. Such a signal is dependent on the thickness of the film.[40,41] Detailed data analysis methods on SFG spectra collected from a thin film with various models have been reported previously.[42-44] Here, the method for SFG data analysis is presented so that the results discussed in later sections can be understood more easily.

As discussed above, $\chi^{(2)}_{eff}$ is the effective second-order nonlinear optical susceptibility at the interface. Different $\chi^{(2)}_{eff}$ components can be measured through different polarization combinations of the input and signal beams (for instance, ssp: s polarized signal beam, s polarized visible input beam, and p polarized input IR beam, or sps: s polarized signal beam, p polarized visible input beam, and s polarized input IR beam), and we call them $\chi^{(2)}_{eff,ssp}$ and $\chi^{(2)}_{eff,sps}$, just to name some examples. We then have:

$$\chi^{(2)}_{eff,ssp} = L_{yy}(\omega)L_{yy}(\omega_1)L_{zz}(\omega_2)sin\beta_2\chi_{yyz} \quad (1\text{-}4)$$

$$\chi^{(2)}_{eff,sps} = L_{yy}(\omega)L_{zz}(\omega_1)L_{yy}(\omega_2)sin\beta_1\chi_{yzy} \quad (1\text{-}5)$$

where χ_{yyz} and χ_{yyz} are different components of $\chi^{(2)}$ defined in the laboratory-fixed coordinate system with the z-axis lying along the interface normal and x-axis in the input beam incident plane. L_{ii} (i=*x, y or z*) are the Fresnel coefficients and β_1 and β_2 are angles between the surface normal and the input visible/infrared beams respectively.

The above data analysis method will be used in analyzing SFG results obtained experimentally. Take chapter 3 as an example, we aim to study the buried polythiophene (PT)/perovskite interface. Samples prepared using a thin layer of polythiophene (PT) spun onto a perovskite surface will generate SFG signal from both the PT/air surface and PT/perovskite interface. Since the PT layer is thin (a thick PT layer cannot be used here – otherwise the IR beam will be attenuated or blocked which cannot access the buried interface to study the structure there), we are unable to separate the signals contributed from the surface and the interface spatially. Often a polymer/air interface generates a much stronger SFG signal compared to that from a buried interface, causing large errors for structural studies of the buried interface. Here we deposited a thin layer of poly(methyl methacrylate) (PMMA) on top of the PT layer. This allows for signals at the PMMA/PT interface (interface I) and the perovskite/PT interface (interface II) to have similar intensities. By varying the PT film thickness, we are able to modulate the interference of the SFG signals from the interface I and interface II in order to separate the signal contribution of each interface. The detected SFG signal from the PT layer can be written as:

$$\chi^{(2)}_{eff,ssp} = \mathrm{L}_{yy}^{interface\ I}(\omega)\mathrm{L}_{yy}^{interface\ I}(\omega_1)\mathrm{L}_{zz}^{interface\ I}(\omega_2)sin\beta_2\chi_{yyz}^{interface\ I} +$$

$$\mathrm{L}_{yy}^{interface\ II}(\omega)\mathrm{L}_{yy}^{interface\ II}(\omega_1)\mathrm{L}_{zz}^{interface\ II}(\omega_2)sin\beta_2\chi_{yyz}^{interface\ II} + \chi_{NR}e^{i\varphi ssp} \quad (1\text{-}5)$$

To simplify equation (1-5), Fresnel coefficients of different polarization combinations can be written as:

$$F_{yyz}^{interface\ I} = \left|\mathrm{L}_{yy}^{interface\ I}(\omega)\mathrm{L}_{yy}^{interface\ I}(\omega_1)\mathrm{L}_{zz}^{interface\ I}(\omega_2)sin\beta_2\right| \quad (1\text{-}6)$$

$$F_{yyz}^{interface\ II} = \left|\mathrm{L}_{yy}^{interface\ II}(\omega)\mathrm{L}_{yy}^{interface\ II}(\omega_1)\mathrm{L}_{zz}^{interface\ II}(\omega_2)sin\beta_2\right| \quad (1\text{-}7)$$

Combining equations 1-4, 5 and 6, we have:

$$I_{SFG} \propto C\left|F_{yyz}^{interface\ I}\chi_{yyz}^{interface\ I}e^{i\phi} + F_{yyz}^{interface\ II}\chi_{yyz}^{interface\ II} + \chi_{NR}e^{i\varphi}\right|^2 \quad (1\text{-}7)$$

where Φ and φ are the phase difference between the SFG signals generated from the interface I and the interface II, and the phase difference between the nonresonant background and the interface II, respectively. The nonresonant background term can be obtained from SFG spectral fitting, and in this case it is negligible. Previous studies showed that SFG signal has a strong dependence on the interference of light caused by different thicknesses of the object films.[45-48] In this case the Fresnel coefficients of different interfaces in the above equations can be calculated using a three-layer interference model.[41,44,47,49] The Fresnel coefficients are also dependent on the PT film thickness (the thickness is embedded in the phase term of eq.1-7). In order to deconvolute $\chi_{yyz}^{interface\ I}$ and $\chi_{yyz}^{interface\ II}$ from the overall collected SFG signal intensity, we need two I_{SFG} measurements from films of two different thicknesses. Combining the measured SFG signals of the PT layers with two different thicknesses with calculated Fresnel coefficients of the two interfaces for each sample, we can deduce the $\chi_{yyz}^{interface\ I}$ and $\chi_{yyz}^{interface\ II}$ and furthermore

reconstruct the SFG spectra originating from each layer (which will be shown in the results presented in chapters 2 and 3 below).

1.2.4. Molecular Orientation Calculation Using Polarized SFG Spectroscopy

The above section described how to deconvolute SFG signal contributed from an interface of interest. To extract the molecular orientation information from the deduced χ one needs to take one step further, as presented below.

In the above equations 1-4 and 1-5, L_{yy} and L_{zz} represent the Fresnel coefficients that are dependent on the laser input angles and the refractive indices of materials, and θ_{IR} represents the incident angle of the IR beam. The second order nonlinear optical susceptibility components (e.g., χ_{yyz}) of a vibration of a functional group can be correlated to various components of the molecular hyperpolarizability β (e.g., β_{aac}, β_{bbc}, or β_{ccc}) defined in the molecular fixed frame (a, b, c) through orientations of the functional group. Therefore by measuring χcomponents, orientation information of a functional group on surface/at interface can be deduced.

Orientation analysis of various different functional groups has been published in details. Such functional groups include methyl group,[50,51] methylene group, C-H stretch of phenyl group, α-helical and β-sheet secondary structures in protein and peptides. This thesis performed orientation analysis of methyl group (chapter 4), methylene group (chapter 4), thiophene ring (chapter 2, 3) and peptide α-helical structure (chapter 5). Here, the orientation calculation of thiophene ring on PT backbone will be introduced as an example for SFG orientation analysis.

As described previously, orientation analysis of a functional group in SFG study relies on the correlation between the second order nonlinear surface susceptibility χ and molecular hyperpolarizability β (or the correlation between lab-fixed frame and the molecular fixed frame). To define a functional group's orientation at an interface, three angles in the lab-fixed frame were utilized: the azimuthal angle ϕ, the twist angle ψ, and the tilt angle θ. Any functional group's orientation at an interface can be described by these three angles. Since in the lab-fixed frame the surface (x-y) plane can be assumed to be isotropic, then the azimuthal angle ϕ can be averaged from 0° to 360°. This leaves only two parameters to deduce: the twist angle ψ and the tilt angle θ. Because a thiophene backbone group adopts a C_{2v} symmetry, Moad et al. and Anglin et al. have shown the simplified molecular hyperpolarizability under C_{2v} molecular symmetry.

For C_{2v} symmetry:

$$\chi_{XXZ} = \chi_{YYZ} = \frac{1}{2} N_s \times \begin{Bmatrix} \langle \sin^2\theta\cos\theta \rangle (\beta_{zzz}) + \langle \cos\theta \rangle (\beta_{xxz} + \beta_{yyz}) \\ -\langle \sin^2\theta\cos\theta\sin^2\psi \rangle (\beta_{yyz} + \beta_{yzy} + \beta_{zyy}) \\ -\langle \sin^2\theta\cos\theta\sin^2\psi \rangle (\beta_{xxz} + \beta_{xzx} + \beta_{zxx}) \end{Bmatrix} \tag{1-8}$$

$$\chi_{XZX} = \frac{1}{2} N_s \times \begin{Bmatrix} \langle \sin^2\theta\cos\theta \rangle (\beta_{zzz}) + \langle \cos\theta \rangle (\beta_{xzx} + \beta_{yzy}) \\ -\langle \sin^2\theta\cos\theta\sin^2\psi \rangle (\beta_{yyz} + \beta_{yzy} + \beta_{zyy}) \\ -\langle \sin^2\theta\cos\theta\sin^2\psi \rangle (\beta_{xxz} + \beta_{xzx} + \beta_{zxx}) \end{Bmatrix} \tag{1-9}$$

$$\chi_{ZXX} = \frac{1}{2} N_s \times \begin{Bmatrix} \langle \sin^2\theta\cos\theta \rangle (\beta_{zzz}) + \langle \cos\theta \rangle (\beta_{zxx} + \beta_{zyy}) \\ -\langle \sin^2\theta\cos\theta\sin^2\psi \rangle (\beta_{yyz} + \beta_{yzy} + \beta_{zyy}) \\ -\langle \sin^2\theta\cos\theta\sin^2\psi \rangle (\beta_{xxz} + \beta_{xzx} + \beta_{zxx}) \end{Bmatrix} \tag{1-10}$$

$$\chi_{ZZZ} = N_s \times \begin{Bmatrix} \langle \cos^3\theta \rangle (\beta_{zzz}) \\ + \langle \sin^2\theta \cos\theta \sin^2\psi \rangle (\beta_{yyz} + \beta_{yzy} + \beta_{zyy}) \\ + \langle \sin^2\theta \cos\theta \cos^2\psi \rangle (\beta_{xxz} + \beta_{xzx} + \beta_{zxx}) \end{Bmatrix} \quad (1\text{-}11)$$

From eq 1-8, eq 1-9, eq 1-10, eq 1-11, $\left|\chi^{(2)}_{eff,PPP} / \chi^{(2)}_{eff,SSP}\right|$ which can be measured experimentally by using different polarization combinations, can be expressed as:

$$\left|\chi^{(2)}_{eff,PPP} / \chi^{(2)}_{eff,SSP}\right| = \frac{\left|\begin{array}{l} -L_{xx}(\omega)L_{xx}(\omega_1)L_{zz}(\omega_2)\cos\beta\cos\beta_1\sin\beta_2\chi_{xxz} \\ -L_{xx}(\omega)L_{zz}(\omega_1)L_{xx}(\omega_2)\cos\beta\sin\beta_1\cos\beta_2\chi_{xzx} \\ +L_{zz}(\omega)L_{xx}(\omega_1)L_{xx}(\omega_2)\sin\beta\cos\beta_1\cos\beta_2\chi_{zxx} \\ +L_{zz}(\omega)L_{zz}(\omega_1)L_{zz}(\omega_2)\sin\beta\sin\beta_1\sin\beta_2\chi_{zzz} \end{array}\right|}{\left|L_{yy}(\omega)L_{yy}(\omega_1)L_{zz}(\omega_2)\sin\beta_2\chi_{yyz}\right|} \quad (1\text{-}12)$$

Please refer to chapter 2 for detailed Fresnel coefficient values, and hyperpolarizability tensor component values have been published elsewhere:[2,3] $\frac{\beta_{aac}}{\beta_{ccc}} \approx 70$ and $\frac{\beta_{bbc}}{\beta_{ccc}} \approx -1$. By inserting all these numbers and relations to the above eqns, we could see that the $\left|\chi^{(2)}_{eff,PPP} / \chi^{(2)}_{eff,SSP}\right|$ ratio depends on the tilt angle θ and the twist angle ψ.

1.3. Presented Research

Chapters 2 and 3 will focus on using SFG to deduce surface and buried interface structure of organic semiconductors in both semiconductor and photovoltaics applications. Surface and interfacial molecular structures of a series of PT derivatives will be investigated. This research elucidated the effects of solvent used for film preparation, hydrophobicity of the substrate for film deposition, polymer side chain composition on the interfacial structure of semiconductor polymers,

Such research also provides in-depth understanding on the correlations between interfacial structures of the semiconductor polymer and the performance of the solar cells made using such polymers.

Chapter 4 will report the results on interfacial structures of two types of polyethylene (PE) at polymer/oxide and polymer/polymer interfaces. To enhance adhesion of PE, one type of PE was incorporated with maleic anhydride (MAH). SFG will be used to probe how such a modification impacts on the interfacial structure. The structure will also be correlated with the measured adhesion property. Interfacial structure of organic adhesives is also crucial because mechanical failure of organic adhesives mostly happened at interfaces. While measuring adhesion strength is relatively straightforward, non-destructively probing the interfacial molecular structure has been a long-lasting question. The research performed in this chapter was in collaboration with researchers at Dow Chemical.

Chapter 5 will present two different applications of a Microscope-SFG platform, a multimodal analytical platform including an SFG spectrometer and an optical/fluorescence microscope. By using this analytical platform, one can extend SFG's application to selectively probe desired spot on heterogeneous surfaces, or to monitor structure (using SFG) and function (using fluorescence imaging) of biological processes at interfaces *in situ* in real time.

This thesis research developed important applications of SFG nonlinear vibrational spectroscopy, which contributes to research fields including molecular spectroscopy, lasers, and nonlinear optics. In addition, the research results reported here will impact many other fields such as semiconductor polymers, solar cells, 2D materials, polymer adhesives, biosensing, and antimicrobial coating.

1.4. Reference

(1) Yamamoto, K.; Ochiai, S.; Wang, X.; Uchida, Y.; Kojima, K.; Ohashi, A.; Mizutani, T. *Thin Solid Films* **2008**, *516*, 2695.

(2) Anglin, T. C.; Speros, J. C.; Massari, A. M. *The Journal of Physical Chemistry C* **2011**, *115*, 16027.

(3) Dhar, P.; Khlyabich, P. P.; Burkhart, B.; Roberts, S. T.; Malyk, S.; Thompson, B. C.; Benderskii, A. V. *The Journal of Physical Chemistry C* **2013**, *117*, 15213.

(4) Videlot, C.; El Kassmi, A.; Fichou, D. *Solar energy materials and solar cells* **2000**, *63*, 69.

(5) Tumbleston, J. R.; Collins, B. A.; Yang, L.; Stuart, A. C.; Gann, E.; Ma, W.; You, W.; Ade, H. *Nature Photonics* **2014**, *8*, 385.

(6) Wu, J.-L.; Chen, F.-C.; Hsiao, Y.-S.; Chien, F.-C.; Chen, P.; Kuo, C.-H.; Huang, M. H.; Hsu, C.-S. *ACS nano* **2011**, *5*, 959.

(7) Yokoyama, D. *Journal of Materials Chemistry* **2011**, *21*, 19187.

(8) Sirringhaus, H.; Brown, P. J.; Friend, R. H.; Nielsen, M. M.; Bechgaard, K.; Langeveld-Voss, B. M. W.; Spiering, A. J. H.; Janssen, R. A. J.; Meijer, E. W.; Herwig, P. *Nature* **1999**, *401*, 685.

(9) Flämmich, M.; Gather, M. C.; Danz, N.; Michaelis, D.; Bräuer, A. H.; Meerholz, K.; Tünnermann, A. *Organic Electronics* **2010**, *11*, 1039.

(10) Agrawal, M.; Sun, Y.; Forrest, S. R.; Peumans, P. *methods* **2007**, *16*, 18.

(11) Li, Y.; Zhang, X.; Myers, J.; Abbott, N. L.; Chen, Z. *Chemical Communications* **2015**, *51*, 11015.

(12) Li, Y.; Wei, S.; Wu, J.; Jasensky, J.; Xi, C.; Li, H.; Xu, Y.; Wang, Q.; Marsh, E. N. G.; Brooks III, C. L. *The Journal of Physical Chemistry C* **2015**, *119*, 7146.

(13) Wang, J.; Even, M. A.; Chen, X.; Schmaier, A. H.; Waite, J. H.; Chen, Z. *Journal of the American Chemical Society* **2003**, *125*, 9914.

(14) Okuno, M.; Ishibashi, T.-a. *The Journal of Physical Chemistry C* **2015**, *119*, 9947.

(15) Ho, J.-J.; Skoff, D. R.; Ghosh, A.; Zanni, M. T. *The Journal of Physical Chemistry B* **2015**, *119*, 10586.

(16) Ding, B.; Jasensky, J.; Li, Y.; Chen, Z. *Accounts of chemical research* **2016**.

(17) Leng, C.; Hung, H.-C.; Sieggreen, O. A.; Li, Y.; Jiang, S.; Chen, Z. *The Journal of Physical Chemistry C* **2015**, *119*, 8775.

(18) Hu, D.; Chou, K. C. *Journal of the American Chemical Society* **2014**, *136*, 15114.

(19) van der Post, S. T.; Hsieh, C.-S.; Okuno, M.; Nagata, Y.; Bakker, H. J.; Bonn, M.; Hunger, J. *Nature communications* **2015**, *6*.

(20) Lis, D.; Backus, E. H.; Hunger, J.; Parekh, S. H.; Bonn, M. *Science* **2014**, *344*, 1138.

(21) Zhang, Y.; Furyk, S.; Bergbreiter, D. E.; Cremer, P. S. *Journal of the American Chemical Society* **2005**, *127*, 14505.

(22) Anim-Danso, E.; Zhang, Y.; Dhinojwala, A. *Journal of the American Chemical Society* **2013**, *135*, 8496.

(23) Sagle, L. B.; Cimatu, K.; Litosh, V. A.; Liu, Y.; Flores, S. C.; Chen, X.; Yu, B.; Cremer, P. S. *Journal of the American Chemical Society* **2011**, *133*, 18707.

(24) Zhang, Y.; Cremer, P. S. *Current opinion in chemical biology* **2006**, *10*, 658.

(25) Xiao, M.; Zhang, X.; Bryan, Z. J.; Jasensky, J.; McNeil, A. J.; Chen, Z. *Langmuir* **2015**, *31*, 5050.

(26) Sohrabpour, Z.; Kearns, P. M.; Massari, A. M. *The Journal of Physical Chemistry C* **2016**.

(27) Xiao, M.; Jasensky, J.; Zhang, X.; Li, Y.; Pichan, C.; Lu, X.; Chen, Z. *Physical Chemistry Chemical Physics* **2016**, *18*, 22089.

(28) Ye, H.; Abu-Akeel, A.; Huang, J.; Katz, H. E.; Gracias, D. H. *Journal of the American Chemical Society* **2006**, *128*, 6528.
(29) Walter, S. R.; Youn, J.; Emery, J. D.; Kewalramani, S.; Hennek, J. W.; Bedzyk, M. J.; Facchetti, A.; Marks, T. J.; Geiger, F. M. *Journal of the American Chemical Society* **2012**, *134*, 11726.
(30) Shen, Y. R. *Nature* **1989**, *337*, 519.
(31) Wang, J.; Chen, C.; Buck, S. M.; Chen, Z. *The Journal of Physical Chemistry B* **2001**, *105*, 12118.
(32) Su, X.; Cremer, P. S.; Shen, Y. R.; Somorjai, G. A. *Physical review letters* **1996**, *77*, 3858.
(33) Su, X.; Cremer, P. S.; Shen, Y. R.; Somorjai, G. A. *Journal of the American Chemical Society* **1997**, *119*, 3994.
(34) Chen, Z.; Shen, Y. R.; Somorjai, G. A. *Annual review of physical chemistry* **2002**, *53*, 437.
(35) Kim, J.; Cremer, P. S. *Journal of the American Chemical Society* **2000**, *122*, 12371.
(36) Cong, X.; Poyton, M. F.; Baxter, A. J.; Pullanchery, S.; Cremer, P. S. *Journal of the American Chemical Society* **2015**, *137*, 7785.
(37) Yan, E. C. Y.; Fu, L.; Wang, Z.; Liu, W. *Chemical reviews* **2014**, *114*, 8471.
(38) Perry, A.; Ahlborn, H.; Space, B.; Moore, P. B. *The Journal of chemical physics* **2003**, *118*, 8411.
(39) Perry, A.; Neipert, C.; Space, B.; Moore, P. B. *Chemical reviews* **2006**, *106*, 1234.
(40) Myers, J. N.; Zhang, X.; Bielefeld, J. D.; Lin, Q.; Chen, Z. *The Journal of Physical Chemistry B* **2015**.
(41) Lu, X.; Shephard, N.; Han, J.; Xue, G.; Chen, Z. *Macromolecules* **2008**, *41*, 8770.
(42) Backus, E. H. G.; Garcia-Araez, N.; Bonn, M.; Bakker, H. J. *The Journal of Physical Chemistry C* **2012**, *116*, 23351.
(43) Tong, Y.; Zhao, Y.; Li, N.; Osawa, M.; Davies, P. B.; Ye, S. *The Journal of chemical physics* **2010**, *133*, 034704.
(44) Lu, X.; Clarke, M. L.; Li, D.; Wang, X.; Xue, G.; Chen, Z. *The Journal of Physical Chemistry C* **2011**, *115*, 13759.
(45) FitzGerald, W. R.; Jena, K. C.; Hore, D. K. *Journal of Molecular Structure* **2015**, *1084*, 368.
(46) Kearns, P. M.; O'Brien, D. B.; Massari, A. M. *The journal of physical chemistry letters* **2015**.
(47) Myers, J. N.; Zhang, X.; Bielefeld, J.; Lin, Q.; Chen, Z. *The Journal of Physical Chemistry B* **2015**, *119*, 1736.
(48) Zhang, X.; Myers, J. N.; Huang, H.; Shobha, H.; Chen, Z.; Grill, A. *Journal of Applied Physics* **2016**, *119*, 084101.
(49) Lu, X.; Li, D.; Kristalyn, C. B.; Han, J.; Shephard, N.; Rhodes, S.; Xue, G.; Chen, Z. *Macromolecules* **2009**, *42*, 9052.
(50) Zhang, C.; Chen, Z. *The Journal of Physical Chemistry C* **2013**, *117*, 3903.
(51) Bao, Z.; Dodabalapur, A.; Lovinger, A. J. *Applied Physics Letters* **1996**, *69*, 4108.

CHAPTER 2 Surface And Interfacial Structure Of Organic Semiconductors

Materials covered in this chapter were published in *Langmuir* **2015**, *31*, 5050 and *Physical Chemistry Chemical Physics* **2016**, *18*, 22089. This research was in collaboration with Prof. Anne McNeil's group.

2.1. Background and Motivation

Organic semiconducting materials have generated strong interest due to their low fabrication cost, tunable charge transport property, and ability to facilitate large-area device fabrication.[1-3] In contrast, the extent of crystallinity in these materials is low which decreases hole mobility and leads to an increasing (unfavorable) resistivity.[4-6] Unlike many amorphous polymers such as poly (methyl methacrylate) (PMMA) and poly (ethylene terephthalate) (PET), conductive polymers usually form semi-crystalline materials induced by intermolecular π-π stacking.[7] For these materials, resistivity is comparatively low along the conjugated polymer backbone. However, between the amorphous polymer chains, resistivity increases dramatically as electrons hop between polymer chains.[8] Because most current organic field-effect transistors adapt a thin-film structure, surface and interfacial structure such as structural ordering should greatly alter its hole mobility. Therefore, it is important to carefully design polymer chemical structure and control the surface/interface structures of such thin films.

However, such an objective is challenging due to the difficultly in controlling the structure of an organic semiconducting thin film, and it is also difficult to model, characterize, and quantify

such a structure at a molecular level due to the unavailability of proper analytical techniques. Many applicable and widely used characterization methods for these thin film materials have some disadvantages: Transmission electron microscope (TEM) requires a relatively complicated sample preparation procedure and cannot probe a buried interface; scanning electron microscope (SEM) and atomic force microscope (AFM) only provide information of surface morphology and lack the ability to characterize chemical or electronic structures; and X-ray diffraction provides information from the bulk, not the surface or interface. Furthermore, the X-ray diffraction signal from such thin films is usually too weak to provide concrete information because such films usually lack crystallinity.

Recent research shows that the hole mobility in organic semiconductors can be enhanced by various methods (e.g., through film fabrication such as alteration of the structural design of such materials (via polymer regioregularity, molecular weight, side chain engineering etc.),[9-14] annealing, or utilizing different solvent combinations). Designing an optimized organic dielectric layer that has direct contact with the semiconducting organic thin film has also been proposed as an alternative method.[15-18]

Among many different kinds of organic semiconducting materials, poly-3-hexylthiophene (P3HT) is an appealing polymer that has been investigated extensively due to its high hole mobility, good solubility in a variety of organic solvents, and especially its unique self-assembly property.[19,20] By tuning P3HT's regioregularity, its charge transport efficiency can be tuned.[2,9,21] The charge transport efficiency can also be varied by changing the P3HT molecular weight,[10] and improved by annealing the spin-coated P3HT films.[22] In this chapter, an in-depth study will be carried out to study the effects of casting solvent, underneath dielectric layer, and side chain chemical environment on P3HT molecular structures.

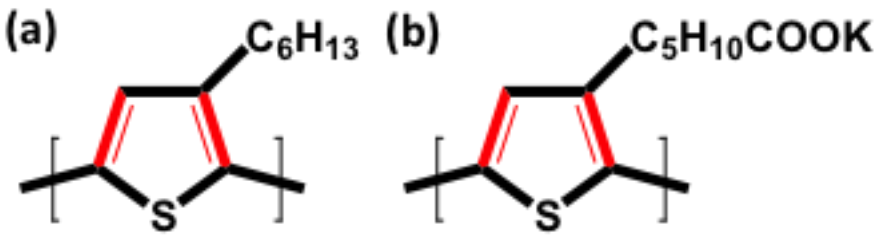

Figure 2-1 Molecular structures of (a) poly(3-hexyl thiophene) (P3HT), (b) poly(3-potassium-6-hexanoate thiophene) (P3KHT)

Recently, it was found that the addition of a small amount of a poor solvent into a good solvent could improve poly-3-hexylthiophene's (P3HT) conductivity.[23] It was believed that a small amount of poor solvent could introduce hydrogen bonds into the solution and stimulate the self-assembly property of P3HT to create a higher crystallinity thin film after spin-coated on a substrate. It was also found that the surface property of underneath dielectric layer could also dramatically alter the hole mobility of P3HT films. For field-effect transistors, P3HT material is mainly used in the form of polymer thin-films. Since surface and interface properties of this film can greatly influence its function and performance, it is crucial to characterize the surface morphology and surface molecular structure of P3HT films using surface-sensitive *in situ* measurements.[24,25] Beside surface and interfacial structure, bulk structure of polythiophene films would also be studied. In this study, SFG was used to investigate molecular structures of P3HT on surfaces and at interfaces, while X-ray diffraction and UV-vis spectroscopy were used to examine the P3HT bulk structure. In addition to P3HT, a polythiophene with a more hydrophilic side chain, poly (3-potassium-6-hexanoate thiophene) (P3KHT), was also investigated. It was found that the buried interfacial structure of a polythiophene thin film is dependent on the side chain hydrophobicity

and the hydrophobicity of the underneath substrate surface. Such buried interfacial structure also influences the bulk and the surface structure of the polymer thin film.

2.2. Solvent Effect on the Surface, Bulk and Buried Interfacial Structures of Poly (3-Hexylthiophene) Thin Film

2.2.1. Materials Used and Sample Preparation

Two types of P3HT samples with different molecular weights were studied. The 70 kDa P3HT sample was purchased from Sigma Aldrich and used without further purification. The 19 kDa P3HT sample was synthesized as reported previously (M_n = 18.8kDa, PDI = 1.23, regioregularity = 80%).[13,26] Acetone and chloroform (Sigma Aldrich) were used as received.

SFG was used to probe molecular structures of the surface and buried interface of P3HT films. Similar SFG sample geometries were used in this study to those reported previously.[27,28] Right angle CaF_2 prisms (Altos Photonics, Inc.) and CaF_2 windows (ESCO Products, Inc.) were used as thin film substrates in SFG measurements. They were sequentially cleaned using toluene, acetone, soap water, rinsed with deionized water, methanol and dried with nitrogen gas. They were further cleaned by 1 min glow discharge air plasma (PE-50 series Plasma System, Plasma Etch, Inc.) to remove any organic contaminates before polymer thin film deposition. All P3HT samples were prepared using P3HT solutions with a concentration of 10.0 mg/mL. A P-600 spin coater (Speedline Technologies) was used to prepare all the P3HT thin films on both prisms and windows. Film thicknesses were measured by a depth profilometer (Dektak 6 M Stylus Surface Profilometer, Veeco).

2.2.2. Solvent Effect on the Surface and Buried Interfacial Structures of Poly (3-Hexylthiophene) Thin Film

SFG signals detected from a P3HT film have strong contributions from the C=C symmetric stretch at 1445 cm^{-1} [29,30], and the C-H ($-CH_2$, $-CH_3$) Fermi resonance and asymmetric stretch at 2920 cm^{-1} and 2955 cm^{-1} respectively [31]. Because the C=C bonds along the P3HT aromatic backbone contribute substantially to the electron transport, and the hexyl side chains mainly help to dissolve the P3HT molecules to organic solvents [32], this work mainly focuses on the C=C backbone at 1445 cm^{-1}.

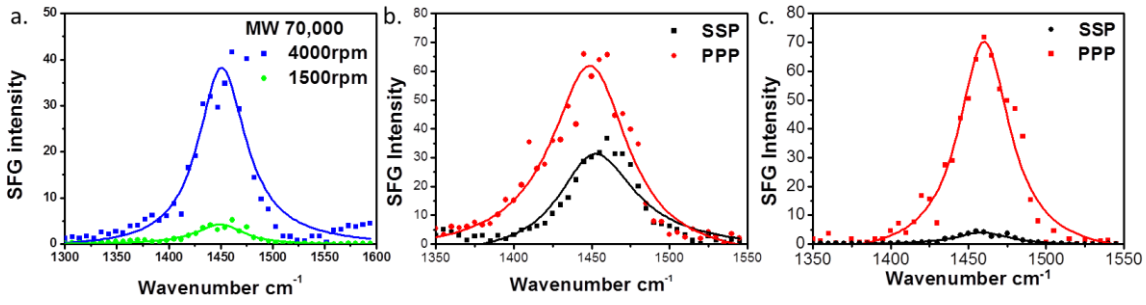

Figure 2-2 (a) SFG spectra (ssp: s-polarized SFG signal beam, s-polarized visible input beam, p-polarized IR input beam) detected from P3HT thin films with different film thicknesses (4000rpm: 42 nm thick; 1500 rpm: 70 nm thick); (b) SFG ssp and ppp spectra from a P3HT thin film before plasma treatment; (c). SFG ssp and ppp spectra collected from the sample studied in (b) after 5s plasma treatment. P3HT films were deposited on CaF_2 prism substrates and SFG spectra were collected using the prism geometry.

To determine the surface and bulk origins of the SFG signal, thickness-dependent studies were performed on P3HT thin films (Fig. 2-2). Results show that SFG signal intensity increases with decreasing polymer film thickness, indicating that the SFG signal does not contain substantial contributions from the P3HT bulk, which would correlate to thicker films generating stronger SFG signals. Therefore we believe that the observed SFG signal must have contributions primarily from

the polymer film surface, or the polymer/substrate interface, or both, which will be studied in more detail below.

Brief plasma exposure can destroy the surface structure of a thin film, but has minimal to no effect on the buried interface between the polymer film and the substrate. By applying 5s oxygen plasma to a P3HT film surface, the ssp SFG signal intensity decreased dramatically, while the ppp SFG spectra remained almost unchanged (Fig 2-2).[33,34] This result indicates that not only does the ssp SFG signal originate from the polymer surface rather than the buried interface, but that the surface structure of the P3HT thin film was damaged by the oxygen plasma. In contrast, the buried polymer film/substrate interface contributes primarily to the observed ppp SFG signal and was not affected by a brief plasma treatment.

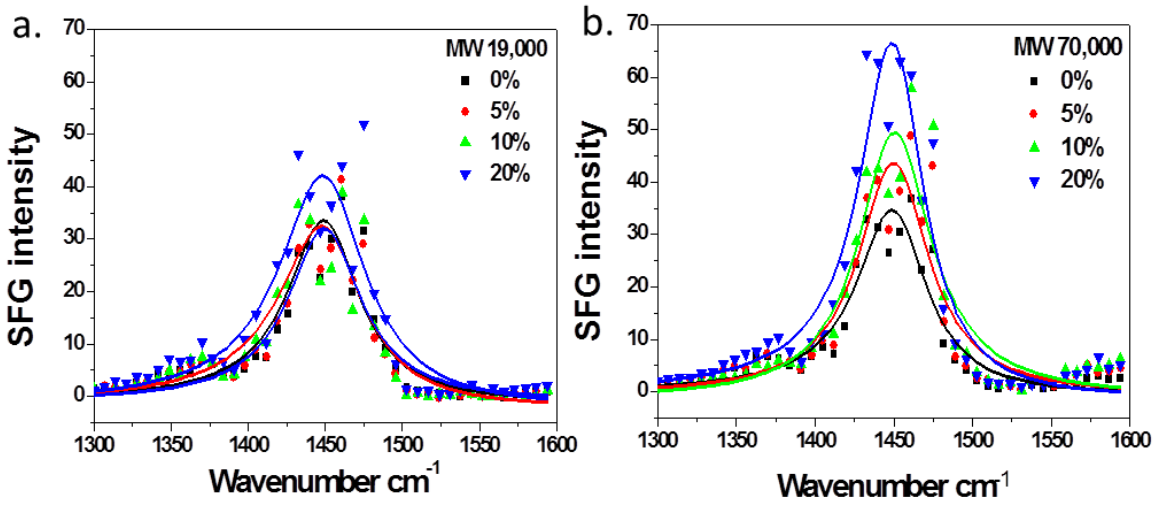

Figure 2-3 (a) SFG ssp spectra collected from the P3HT films prepared with solutions containing different acetone ratios using P3HT with a MW of 19 kDa; (b) SFG ssp spectra collected from the P3HT films prepared with solutions containing different acetone ratios using P3HT with a MW of 70 kDa. The polymer films were deposited on the CaF_2 prisms

As discussed above, it was found previously in the literature that adding a small amount of poor solvent to the solution can increase the conjugate polymer's hole mobility,[23] but the in-depth understanding on the surface/bulk structure to further explain such an observed phenomenon is missing. Here we used SFG to study P3HT films prepared from P3HT solutions containing different ratios of "bad" solvent acetone. SFG ssp spectra collected from such films prepared using P3HT with different molecular weights, 19 kDa and 70 kDa, are shown in Fig 2-3a and Fig 2-3b, respectively. Results of Fig 2-3a show that the SFG signal intensity slightly increased from the P3HT film as the acetone ratio in solution increased. Fig 2-3b shows that such an increase was much more obvious for a higher molecular weight P3HT. Therefore the C=C stretching signal increase is not because more C=C groups aggregate to the surface by replacing C-H groups. It is well known that due to the slightly different dihedral angles between neighboring thiophene rings along the P3HT polymer backbone, the net transition dipole of the C=C stretching mode is perpendicular to the polymer backbone (Fig 2-4).[29,35] In more detail, IR dipole transition of such a symmetric stretching of a single thiophene ring lies in the ring plane, however, because of the alternating arrangement of the large thiophene conjugation system of the regioregular thiophene conjugate system, neighboring thiophene ring has a dihedral angle (∠S-C-C-S) of around 165°. In plane vibrational dipole transition moment cancels out in this case, and the net transition dipole at 1445 cm^{-1} therefore aligns perpendicularly to the thiophene backbone.[35] Molecular orientation of the P3HT molecule can be determined by relating the macroscopic susceptibility tensor elements to their microscopic hyperpolarizability tensor elements.

Figure 2-10 shows the dependence of χ_{yyz} on the polythiophene dipole orientation angle. Therefore, from a consistent 1445 cm^{-1} ssp SFG signal increase as more acetone is blended into

the solution used to prepare the P3HT film, we believe that the net C=C stretching transition dipole was more ordered along the surface normal (or standing up more – the same meaning) of the P3HT film surface. (Fig 2-4) Combining with the ssp results discussed above, this means that the P3HT polymer tends to more lie down on the surface as the poor solvent content used to prepare the P3HT film increases. The hole mobility study in the literature was correlated well to this result: as P3HT lies down more (010), its hole mobility is higher than the standing up mode (100).[20] Our results also indicated that a higher molecular weight of P3HT leads to a more distinct P3HT film surface order (along the surface normal) – P3HT solvent dependence. Likely the observed molecular weight effect is due to the increased intermolecular π-π stacking between polymer chains as the chain length increases.[36]

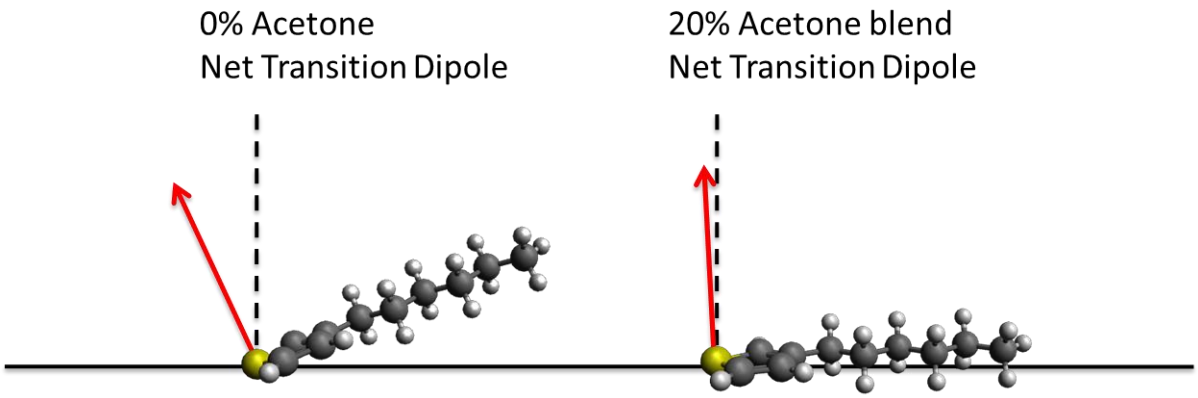

Figure 2-4 Illustrations of different orientations (or orderings) of P3HT molecules on the surfaces of the P3HT films prepared using different solvents.

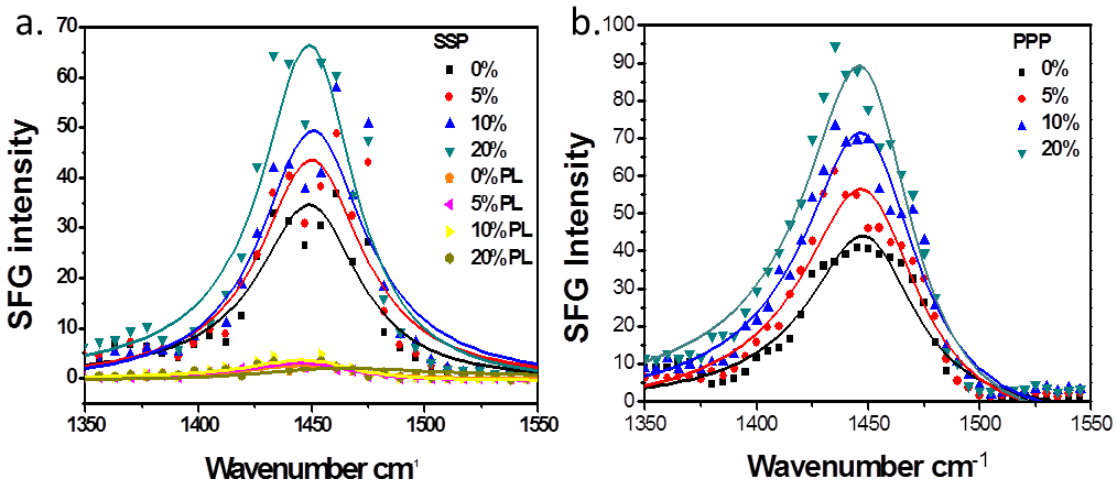

Figure 2-5 (a) SFG ssp spectra collected from P3HT (MW: 70 kDa) films prepared using mixed solvents with different acetone contents before and after plasma treatment; (b) SFG ppp spectra collected from P3HT (MW: 70 kDa) films using mixed solvents with different acetone contents. Polymer films were deposited on CaF_2 prisms.

To ensure that the above SFG ssp signals shown in Fig 2-3 are contributed by the P3HT film surfaces, we exposed some of these polymer thin films (MW: 70kDa) to oxygen plasma for 5s. All the SFG ssp signals dropped significantly after the plasma treatment, showing that the original signals were detected from the surfaces, and the surfaces were damaged by a short time plasma treatment. SFG ppp spectra in Fig 2-5 also showed a consistent increasing trend as the concentration of the polar solvent increased. As we stated above, the SFG ppp spectra are believed to be contributed mainly from the buried interface, which indicates an edge on pose of net transition dipole for the P3HT molecules at buried interface when the solution contains more acetone. [37,38]

We designed another experiment to further confirm the surface orientation difference for the P3HT films prepared with different solvents in the P3HT solution. After preparing a P3HT film with P3HT solution in chloroform by spin coating (4000 rpm, 30s) on to a CaF_2 window, a small amount of a solvent with 80% chloroform and 20% acetone was placed in the middle of the above P3HT film on a CaF_2 window. We ensured that only the center region of the film was exposed to the later mixture solvent by adding the solvent to a small container (with no bottom) placed in the center region of the P3HT film (Fig 2-6). We then slightly annealed the sample. The P3HT film center region should be dissolved in the mixed solvent and recrystallized after the solvent evaporated. After that, we placed this P3HT sample onto a step motor-based sample stage (TDC001, Z825, Thorlabs). SFG signal intensity was monitored while the sample was moving at 0.025mm/s. (Fig 2-6, Fig 2-7)

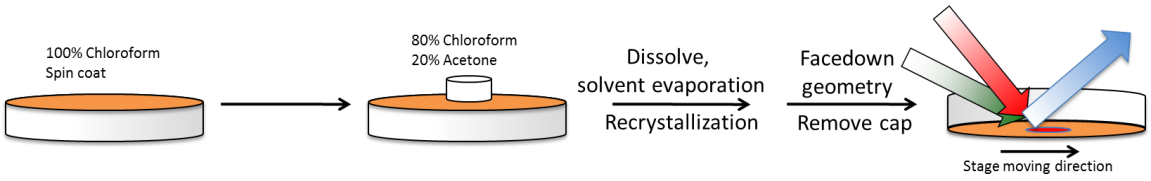

Figure 2-6 Schematic showing the treatment of the center region of the sample with mixed solvent. SFG spectra were collected from the sample while the sample is moving.

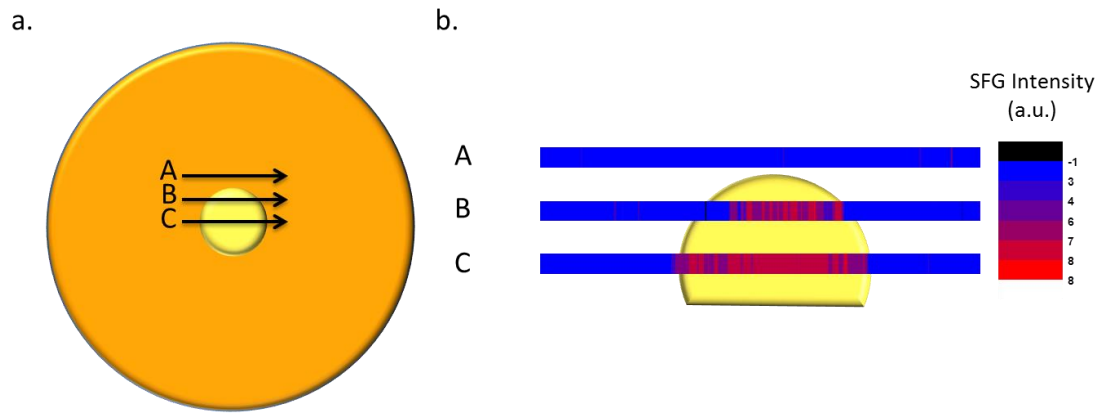

Figure 2-7 (a) Schematic showing the locations on the P3HT film where SFG spectra were collected (Spectra were collected along the lines with arrows); (b) SFG signal intensity detected at 1445 cm^{-1} on different locations on the P3HT film surface.

According to our previous discussion, the recrystallized P3HT film region with a mixed solvent containing a poor solvent should lead to a more ordered surface structure. That is to say, the SFG signal should be stronger from this region. Figure 2-7 shows that indeed the SFG signal was observed to be stronger in the re-crystalized region on the P3HT surface. This experiment again confirms that the surface of the P3HT film prepared using the solvent containing poor solvent is more ordered along the surface normal.

2.2.3. Solvent Effect on the Bulk Structure of Poly (3-Hexylthiophene) Thin Film

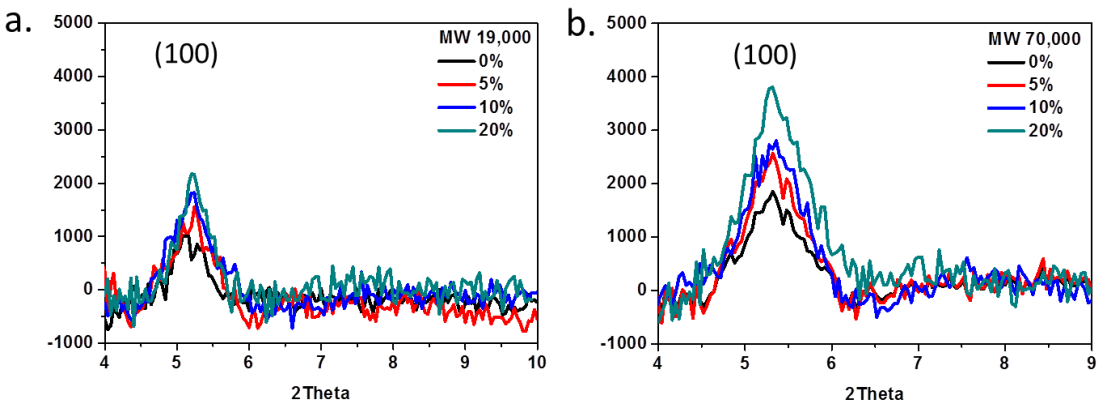

Figure 2-8 (a) X-ray diffraction data of P3HT films prepared using solutions with different solvents (MW: 19 kDa); (b) X-ray diffraction data of P3HT films prepared using solutions with different solvents (MW: 70 kDa).

As stated above, here SFG ssp spectra were contributed from the P3HT thin film surface while SFG ppp spectra were generated from the buried P3HT/CaF_2 interface. We also want to study the bulk structural difference when the film is prepared using mixed solvents. Here the bulk crystallinity was examined by a (100) diffraction pattern observed with X-Ray diffraction.[39] X-ray diffraction data (Fig 2-8) were collected from P3HT films prepared using solutions containing different ratios of poor solvent acetone to good solvent chloroform. One peak centered at 2Theta of 5 degree was observed in each spectrum. This is the diffraction signal from the (100) plane.[40] For both P3HT samples with MW of 19 kDa and 70 kDa, the X-ray diffraction signal increased when the ratio of the poor solvent increased in the P3HT solution used for polymer film preparation. Such increase shows that the P3HT film bulk crystallinity increased when more poor solvent was added to the P3HT solution to prepare the P3HT thin films. This effect is more obvious for P3HT films prepared with a higher molecular weight P3HT. We confirmed that the stronger X-ray

diffraction signals detected are not due to the thicker films. The measured film thicknesses are very similar: 47 nm, 46 nm, 47 nm, and 49 nm for P3HT films prepared using the solvent containing 0%, 5%, 10%, and 20% acetone respectively.

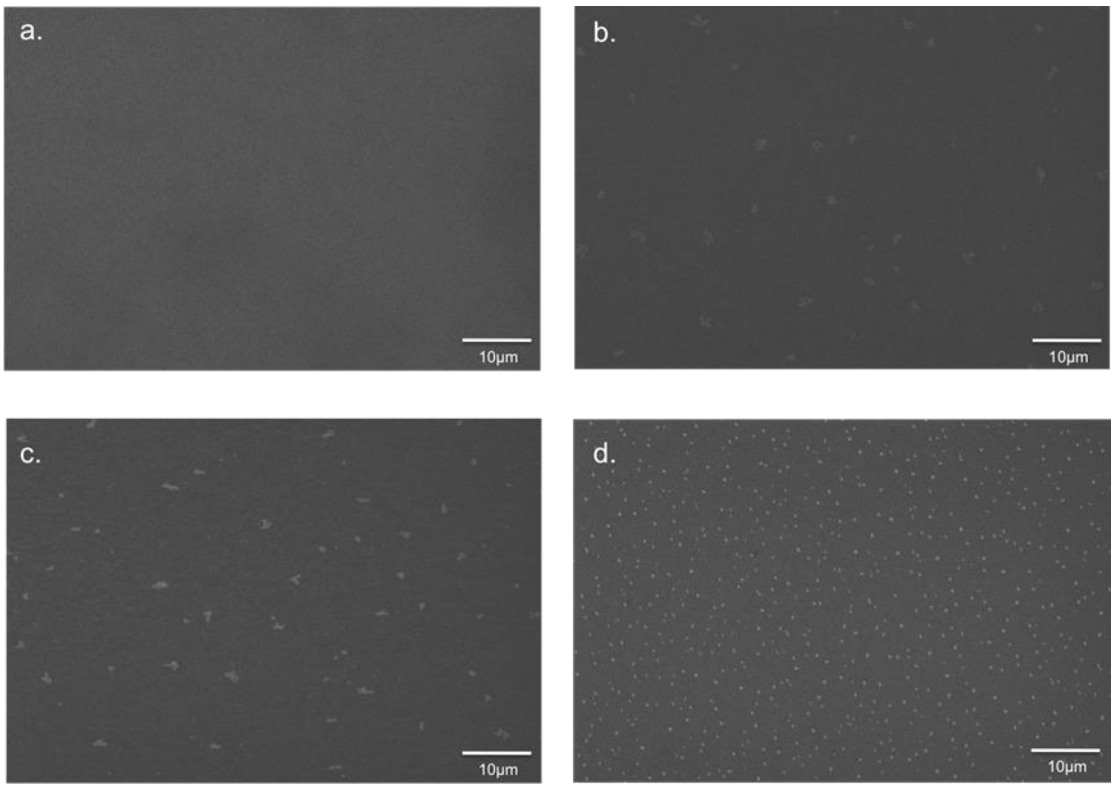

Figure 2-9 SEM pictures of P3HT thin films prepared by spin coating with 70kDa P3HT solutions containing different poor solvent contents: (a) 0% acetone; (b) 5% acetone; (c) 10% acetone; (d) 20% acetone.

The above SFG results indicate that the P3HT backbone will adopt a stand up pose when a higher ratio of acetone is in the solution for polymer film preparation. Fig 2-9 shows the surface morphology difference of the P3HT films prepared using different poor solvent acetone ratios in

the solution. While the solvent contained no acetone, the resulting P3HT film is quite smooth (Fig 2-9a). After the introduction of acetone to the solvent, even only 5%, an island structure could be observed (Fig 2-9b). When more poor solvent was blended, the resulting P3HT film had more islands on the surface, even though finally each individual island became smaller. Such island structure is believed to be induced by acetone and formed during the spin-coating process. After the poor solvent was added, in the spin-coating process, acetone evaporated at a different rate compared to chloroform, leading to the island formation. Perhaps these islands are highly crystallized P3HT, with both higher bulk crystallinity and surface ordering.

As we discussed above, conjugate polymer's performance relies heavily on its surface/interface ordering and bulk crystallinity, and therefore how to measure surface/interface and bulk structures becomes an increasing concern. XRD can give average information from the polymer film bulk, while other widely used techniques such as SEM, AFM and EDX do not provide any information regarding to the surface ordering and surface crystallinity. Analytical methods like Raman or fiber enhanced surface Raman is useful to probe polymer surfaces, but in terms of studying surface ordering or surface crystallinity, their usages may be limited.[41,42] In this study, we demonstrated that SFG is a powerful tool to probe both the polymer/air surface and the buried interface, while X-ray diffraction gives us bulk ordering information. This combined SFG and X-ray diffraction study provided a more complete picture in understanding polymer thin film structures.

2.3. Effects of Substrate and Polymer Side Chain on the Interfacial Structures of Polythiophene

2.3.1. Materials Used and Sample Preparation

Poly (3-hexylthiophene) (P3HT) and poly (3-potassium-6-hexanoate thiophene) (P3KHT) samples used in this study were purchased from Rieke Metal. Trichloro (octadecyl) silane (OTS), trichloro (phenyl) silane, (3-aminopropyl) triethoxysilane, Trichloro (1H, 1H, 2H, 2H-perfluorooctyl) silane, 1-heptanethiol, 12-mercaptododecanoic acid, ethanol, toluene, chlorobenzene, and 100 nm gold coated glass slides were purchased from Sigma Aldrich and used without further purification.

Single side-polished silicon wafers (Boron doped, resistivity < 0.1Ω/cm^2, University Wafer) were cleaned by Contrex, Millipore water, acetone, and isopropyl alcohol for 30 min each, followed by 1 min glow discharge oxygen plasma (P3-50 series Plasma System, Plasma Etch, Inc.). Silicon wafers were then immersed overnight into a glass jar containing 10 mM trichloro (octadecyl) silane (OTS), trichloro (phenyl) silane, (3-aminopropyl) triethoxysilane, or trichloro (1H, 1H, 2H, 2H-pertrifluoromethyloctyl) silane in anhydrous toluene to prepare self-assembled monolayers (SAMs) with different end groups on silicon. SAMs on gold were prepared by immersing gold substrates into a glass jar containing 10 mM 1-heptanethiol or 12-mercaptododecanoic acid in ethanol for 48 h. Thin polymer films on Si were prepared by spin coating PDMS or PVA onto silicon wafer surfaces. Before spin coating polymer, all SAM surfaces (on Si or Au) were carefully washed by toluene, followed by Millipore water. The PVA films were measured to be about 15 nm thick. All P3HT/P3KHT thin films on silane SAMs, PDMS, and PVA surfaces were prepared by spin coating 5.0 mg/1 mL P3HT solution in chlorobenzene at 1500 rpm or 5.0 mg/1mL P3KHT solution in 8:2 chlorophenol/DMSO solution at 500 rpm onto the previously prepared substrates (with SAM or 15 nm polymer film). All P3HT and P3KHT thin films on thiol SAM surfaces were prepared in a similar fashion. A P-600 spin coater (Speedline Technologies) was used to prepare all P3HT and P3KHT thin films. Once spun onto their

respective substrates, polymer films were then stored under vacuum overnight to eliminate the solvent residue. The film thicknesses of all the samples were measured by a depth profilometer (Dektak 6 M Stylus Surface Profilometer, Veeco). SFG signals were collected from P3HT thin films deposited on SAMs or polymer films on silicon wafer substrate or Au surface.

2.3.2. Polythiophene Backbone Orientation Determination Method

The orientation of polythiophene (PT) molecules on the polymer surface in air can be determined using SFG spectra collected using ssp and ppp polarization combinations. It was reported that the SFG signal detected from P3HT centered at 1445 cm^{-1} originates from the polythiophene's C=C symmetric stretch (total symmetric representation of C_{2V} symmetry) as highlighted in Fig 2-1a and 1b.[29,35] In the research reported in the previus section, we qualitatively discuss the polythiophene backbone ordering alomg the surface normal (or standing up orientation). In the following study, the ratio of χ_{SSP} and χ_{PPP} would be used to relate SFG data to the orientation of the P3HT thiophene backbone.[43] IR dipole transition of such a symmetric stretching of a single thiophene ring lies in the ring plane, however, because of the alternating arrangement of the large thiophene conjugation system of the regioregular thiophene conjugate system, neighboring thiophene ring has a dihedral angle (∠S-C-C-S) of around 165°. In plane vibrational dipole transition moment cancels out in this case, and the net transition dipole at 1445 cm^{-1} therefore aligns perpendicularly to the thiophene backbone.[35] Molecular orientation of the P3HT molecule can be determined by relating the macroscopic susceptibility tensor elements to their microscopic hyperpolarizability tensor elements.

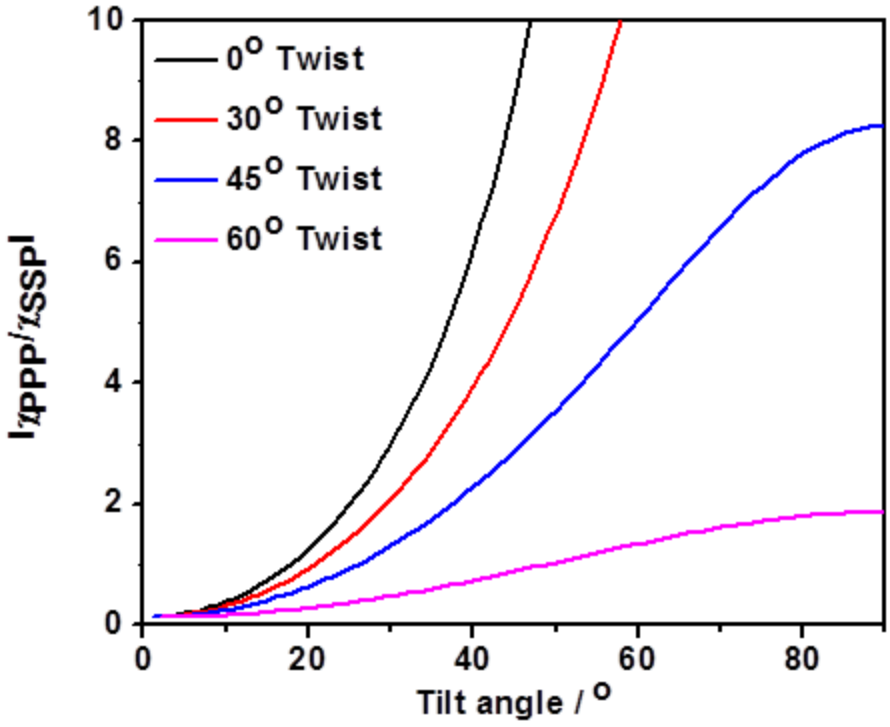

Figure 2-10 Relationship between the χ_{PPP}/χ_{SSP} ratio of the 1445 cm^{-1} peak and the tilt angle of the net transition dipole of P3HT backbone vs. the surface normal.

Fig 2-10 illustrates the relationship between measured χ_{PPP}/χ_{SSP} ratio of the 1445 cm^{-1} peak and the tilt angle (θ) of P3HT thiophene ring[29,44] within the polymer backbone at the P3HT surface vs. the surface normal at different twist angles. At the same twist angle, the tilt angle increased as the χ_{PPP}/χ_{SSP} ratio increased. Since here we only have one measurement, which is the χ_{ppp}/χ_{ssp} ratio, we cannot determine the tilt angle and the twist angle simultaneously. Even though the twist angle is not well characterized, variations of the twist angle will only cause a change in the range for χ_{PPP}/χ_{SSP} (y-axis), but not alter the trend itself.

Fig 2-11 shows SFG ppp and ssp spectra collected from the P3HT films deposited on different SAM and polymer surfaces. As was discussed above, all SFG spectra are comprised of signals from the P3HT/air surface. Each of the SFG spectra was fitted with a single peak centered at 1445 cm^{-1}. Detailed fitting parameters are shown in Table 2-1. It is important to point out that the χ_{ppp}/χ_{ssp} ratio of the P3HT film changes when the hydrophobicity of the substrate surface to deposit the P3HT film varies. The χ_{ppp}/χ_{ssp} ratio decreases as the substrate surface becomes more hydrophilic. Such a decrease leads to a decrease of the tilt angle in the net transition dipole so that the P3HT backbone lies down more. The χ_{ppp}/χ_{ssp} ratios of the SFG spectra collected from the P3HT films on the methyl group ended SAM surface and PDMS surface appear to be the largest (1.73 and 1.72 respectively), while the χ_{ppp}/χ_{ssp} ratio of the SFG spectra collected from the P3HT films on the silicon surface (most hydrophilic substrate, contact angle too low to record) is the smallest (0.95). Assuming a 60° twist angle, the tilt angle of the net transition dipole of P3HT backbone on the P3HT film surface changes from ~72° for the film deposited on a hydrophobic surface to ~45° for the film on a hydrophilic surface.

$-CH_3$ (ppp/ssp) 1.73		$-CF_3$ (ppp/ssp) 1.63		PDMS (ppp/ssp) 1.72	
A	17.1/9.9	A	17.8/9.7	A	8.6/5.0
χ	1445/1445	χ	1445/1445	χ	1445/1445
W	22.7/22.7	W	27.0/23.9	W	22.0/22.0
$-C_6H_5$ (ssp/ssp) 1.35		$-NH_2$ (ppp/ssp) 1.19		PVA (ppp/ssp) 1.19	
A	17.8/13.2	A	16.2/13.6	A	5.7/4.8
χ	1445/1445	χ	1445/1445	χ	1445/1445
W	25.6/25.6	W	22.6/22.6	W	23.9/23.8
Si (ppp/ssp) 0.95		P3KHT 50%CH_3 50%NH_2 1.98		P3KHT –C_6H_5 1.52	

A	17.7/17	A	16.8/8.2	A	17.3/11.4
χ	1445/1445	χ	1440/1440	χ	1440/1440
W	23.2/23.5	W	20.2/19.9	W	20.0/20.0
P3KHT –NH_2 1.36		P3KHT Si 1.09			
A	17.9/12.8	A	14.7/13.8		
χ	1440/1440	χ	1440/1440		
W	19.2/20.1	W	20.4/20.5		

Table 2-1 Fitting parameters of the SFG spectra presented in Fig 2-11 and Fig 2-12

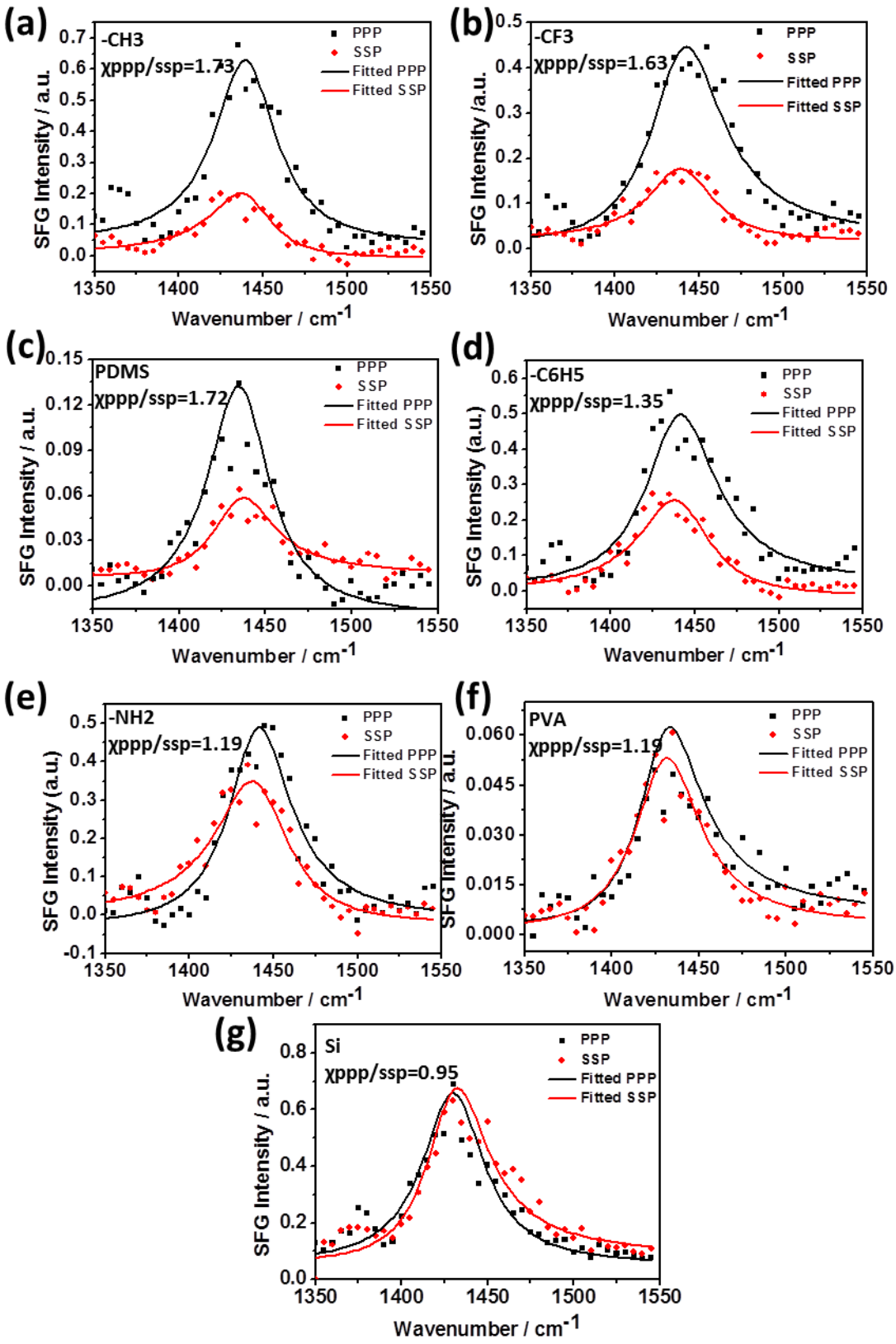
(a)
-CH3
χppp/ssp=1.73
PPP
SSP
Fitted PPP
Fitted SSP
SFG Intensity / a.u.
Wavenumber / cm-1
(b)
-CF3
χppp/ssp=1.63
SFG Intensity /a.u.
(c)
PDMS
χppp/ssp=1.72
(d)
-C6H5
χppp/ssp=1.35
SFG Intensity (a.u.)
(e)
-NH2
χppp/ssp=1.19
(f)
PVA
χppp/ssp=1.19
(g)
Si
χppp/ssp=0.95

Figure 2-11 SFG ssp and ppp spectra detected from P3HT thin films on (a) methyl group ended SAM substrate, (b) trifluoromethyl group ended SAM substrate. (c) PDMS coated substrate, (d) phenyl group ended SAM substrate, (e) amine group ended SAM substrate, (f) PVA coated substrate, and (g) silicon surface.

In addition to the P3HT film surface, surface structures of P3KHT films deposited on different dielectric layers have also been studied using the same approach to understand the polythiophene side chain effect. The same data analysis methodology discussed above was applied. As shown in Fig 2-12, SFG ssp and ppp signals from P3KHT films on four different substrates have been collected. The measured χ_{ppp}/χ_{ssp} ratio of a P3KHT film is the highest when the film is deposited on a mixed methyl and amine SAM surface, while the measured χ_{ppp}/χ_{ssp} ratio is the lowest for a P3KHT film deposited on a silicon surface. It was interesting to observe that SFG χ_{ppp}/χ_{ssp} ratios detected from P3KHT films change as a function of the substrate hydrophobicity, and the trend for such changes is the same as that of P3HT films. The experiments showed that like P3HT, P3KHT's thiophene backbone would also stand up more on the surface in air for a P3KHT film deposited on a hydrophobic substrate, while lie down more on a hydrophilic substrate. If we compare the measured SFG χ_{ppp}/χ_{ssp} ratios of a P3HT film and a P3KHT film on the same substrate, e.g, SAMs prepared with phenyl terminated silane, amine terminated silane, or just bare silicon, we can see that the χ_{PPP}/χ_{SSP} ratio of a P3KHT film is larger. This indicates that the polythiophene ring in the backbone on the P3KHT surface in air stands up more compared to that of the P3HT film deposited on the same substrate,

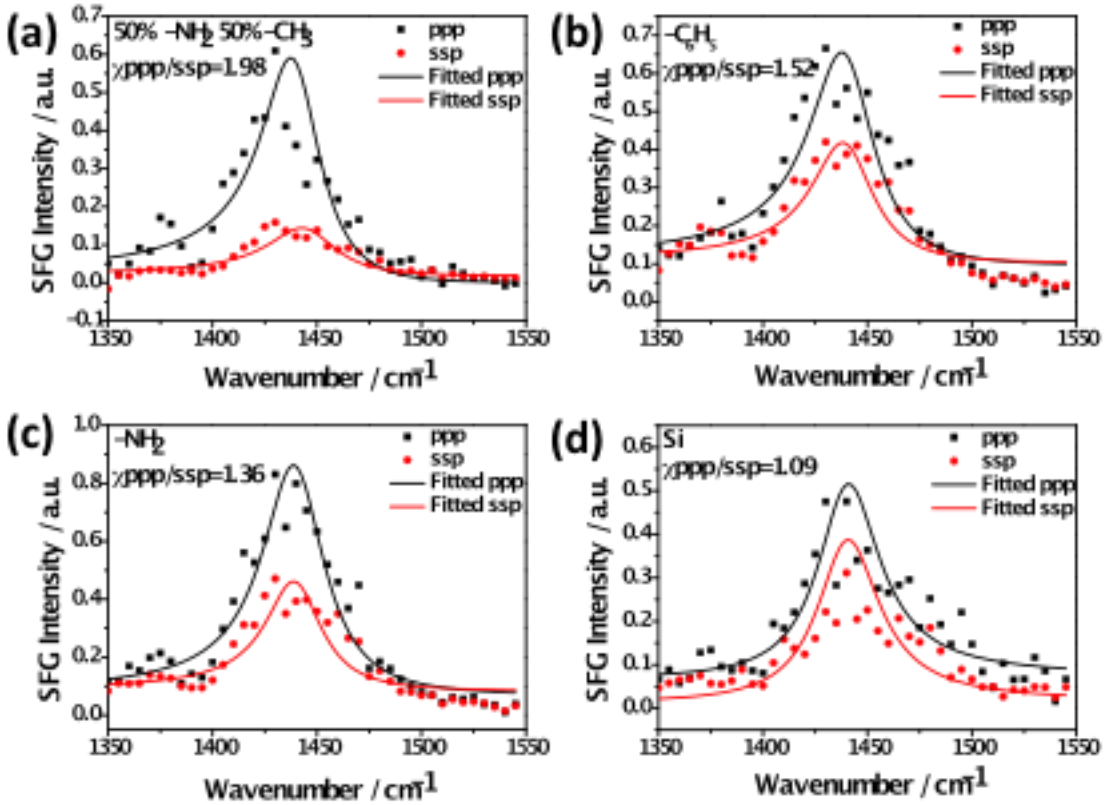

Figure 2-12. SFG ssp and ppp spectra detected from P3KHT thin films on (a) 50% methyl group 50% amine ended SAM substrate, (b) phenyl group ended SAM substrate, (c) amine group ended SAM substrate, (d) pure silicon surface

2.3.3. Results and Discussions of the Studies on Buried Interfacial Structures of Polythiophene Thin Films

It was interesting to observe that both the bulk structures (Fig 2-13 determined by X-ray diffraction) and surface structures in air (determined by SFG) of P3HT and P3KHT thin films vary with changes of the hydrophobicity of the substrate for film deposition. Such substrate

hydrophobicity differences lead to different polythiophene-substrate interactions at the interface, resulting in different P3HT and P3KHT thin film structures in bulk and on the surface. Clearly the different interactions at the interfaces should lead to different interfacial structures as well, which may be able to more substantially influence the performance of the polythiophene films. Therefore, in addition to study polymer surface in air and polymer bulk, we also investigated the buried interfacial structures of P3HT and P3KHT films deposited on different substrates.

P3KHT films are below the detection limit of X-ray diffraction.

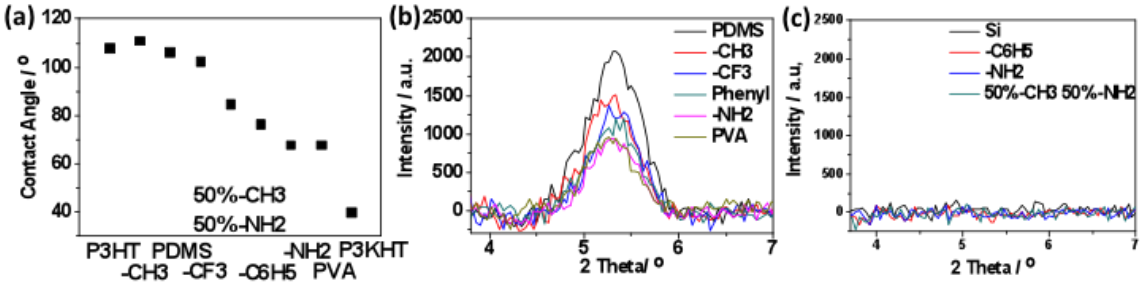

Figure 2-13 (a) Water contact angles on surfaces of different materials including P3HT and P3KHT films prepared on Si wafer. -CH3, -CF3, -C6H5, -NH2 represent SAMs with respective end group. PDMS: poly(dimethylsiloxane). PVA: poly (vinyl alcohol). (b) X-ray diffraction patterns of P3HT thin films prepared on different surfaces: P3HT film on Si. -CH3, -CF3, -C6H5, -NH2: P3HT films on SAMs prepared with respective silane end groups on Si, PDMS: P3HT film on poly(dimethylsiloxane). PVA: P3HT film on poly (vinyl alcohol). (c) X-ray diffraction patterns of P3KHT thin films prepared on different surfaces: Si, -C6H5, -NH2 represent silicon wafer surface, SAMs prepared with respective silane end groups on Si; 50%-CH3 50%-NH2 represents the surface of mixed SAM prepared with 50% methyl terminated and 50% amine terminated silanes.

It has been extensively demonstrated that SFG signals collected from a thin film deposited on a substrate surface in air can originate from both the film surface in air and the substrate/film interface.[37,45] The interference between the surface signal and interface signal of the thin film causes the Fresnel coefficient to vary as a function of film thickness. The values of Fresnel coefficients at different surfaces/interfaces influence the detected SFG signal. Refractive indices of various media involved in SFG experiments are needed to calculate these Fresnel coefficients. Since the SAM layer and the PDMS or PVA layer are both very thin, their effects on Fresnel coefficient calculation can be ignored. Fig 2-14a, b and c show the calculated values of the Fresnel coefficients for SSP and PPP SFG spectra at both the P3HT/air surface and the P3HT/substrate buried interface as a function of the P3HT film thickness (with the visible beam at 60° and the IR beam at 55° vs. the surface normal). Therefore, all polythiophene films were measured to be around 150 nm. Fig 3 shows clearly that at this film thickness, the buried interface SSP and PPP Fresnel coefficients are small, and the signals contributed form the buried interface can likely be ignored. Therefore, we believe that the SFG signals collected from P3HT films deposited on SAMs or polymer thin films on silicon wafer in our study are only generated from the P3HT film/air surface.[37,46,47]

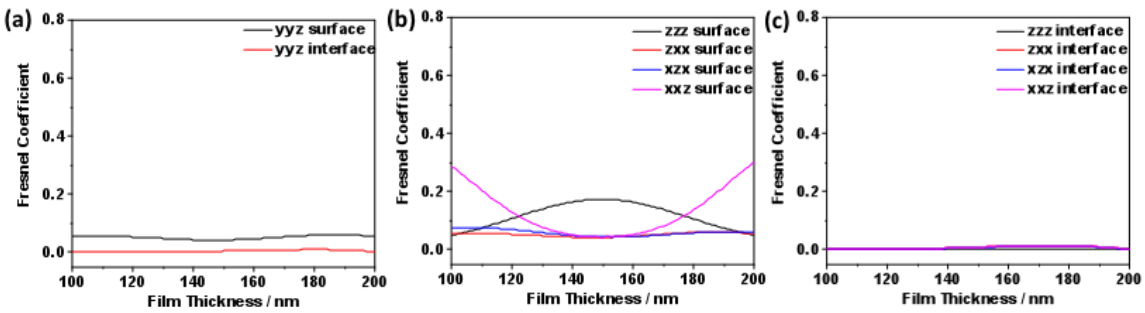

Figure 2-14 (a) Fresnel coefficient values of yyz susceptibility tensor element as a function of P3HT film thickness at the P3HT/air surface and the buried interface; (b) Fresnel coefficient values of zzz, zxx, xzx, xxz susceptibility tensor elements as a function of P3HT film thickness at the P3HT/air surface; (c) Fresnel coefficient values of zzz, zxx, xzx, xxz susceptibility tensor elements as a function of P3HT film thickness at the buried P3HT/substrate interface.

As discussed above, SFG signals collected from a polymer film of 150 nm thick deposited on a SAM or polymer film on silicon wafer mainly originate from the surface in air. Therefore we cannot use the same sample and the same experimental geometry to study the buried polymer/substrate interface with SFG. To selectively probe the buried interface, we used 100 nm gold thin film coated glass slides as substrates to prepare SAM surfaces. It has been shown that metal plasmonic effect can enhance SFG signal from the buried metal interface.[48,49] A layer of SAM was grown on gold surface using thiols and then we deposited a thin film of P3HT or P3KHT (150 nm) on such a SAM surface. Two SAMs were prepared on Au, with methyl and carboxylic acid-terminated thiols. Water contact angles measured on these two surfaces show that the methyl terminated SAM on Au is hydrophobic with a water contact angle of 106.2°, while the carboxylic acid terminated SAM on Au is hydrophilic with a water contact angle of 35.5°.

As stated before, Fresnel coefficients of different interfaces can vary as a function of the film thickness.[37,45] We treat a thin P3HT or P3KHT film on gold using an air/polymer/gold three-layer model to calculate the Fresnel coefficients. Details of the Fresnel coefficient calculations using the three-layer model have been published elsewhere.[37,45] Here, Fresnel coefficients of different χ components as a function of P3HT or P3KHT film thickness are calculated using a three-layer model according to previously developed methodology.[37] When a P3HT or P3KHT

film is 150 nm thick, the SFG PPP signal should originate from both the polymer/air and polymer/SAM (on gold) interfaces. Previously, we showed that the SFG ppp signal from the buried polymer/metal interface can be enhanced by the metal, therefore SFG ppp signal can be dominated by the contribution from the polymer/metal interface.[50] Here, to ensure that we use SFG signal contributed from the buried interface to characterize the buried interfacial structure, we exposed the polythiophene samples to air plasma for a short period of time to disorder the top P3HT/air interface or P3KHT/air interface. After the plasma exposure, the ppp signals decreased but did not vanish. We believe that the SFG ppp spectra collected from the P3HT or P3KHT films after plasma exposure come from the buried P3HT/SAM or P3KHT/SAM (on gold) interface.

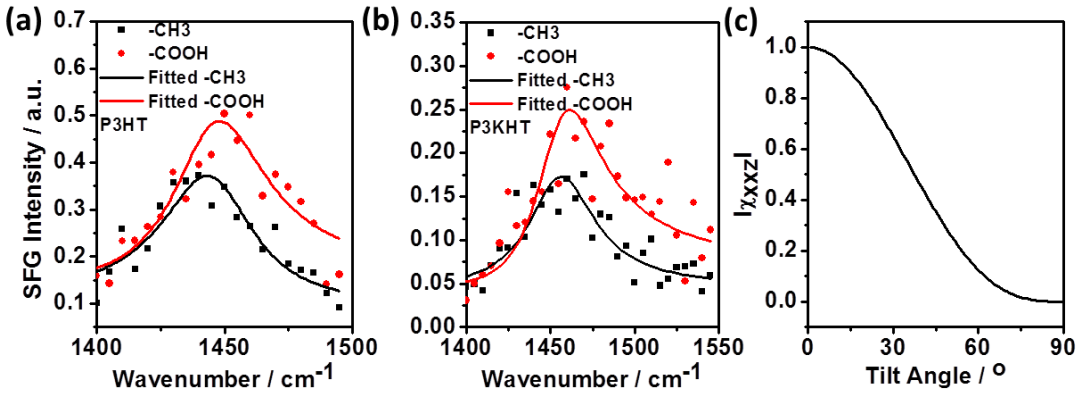

Figure 2-15 (a) SFG PPP spectra collected of a 10 s air plasma treated P3HT thin film (150 nm) on methyl terminated and carboxylic acid terminated thiol SAMs on 100 nm gold substrates; (b) SFG PPP spectra collected of a 10 s air plasma treated P3KHT thin film (150 nm) on methyl terminated and carboxylic acid terminated thiol SAMs on 100 nm gold substrates; (c) Relationship between χ_{xxz} and the tilt angle of net transition dipole in P3HT or P3KHT backbone.

Fig 2-15a and b showed clearly that SFG PPP signals contributed from the buried interfaces are different when the substrate hydrophobicity is different. The PPP signal intensity from a P3HT film on a hydrophobic surface is weaker than that deposited on a hydrophilic surface. Similar result was observed from P3KHT films. The SFG PPP signal intensity detected here is dominated by the contribution of the χ_{xxz} component, which is related to the molecular orientation (Fig 2-15c). Fig 2-15c demonstrated that a P3HT or P3KHT thiophene ring in the backbone that stands up more (meaning a larger transition dipole tilt angle) leads to a smaller χ_{xxz}, or a weaker PPP SFG signal. Combining Fig 2-15a, 13b, and Fig 2-15c, it could be concluded that P3HT or P3KHT thiophene ring in the backbone stands up more at a polymer/hydrophobic substrate interface, while lies down more at a polymer/hydrophilic substrate interface.

A possible explanation for the above observation on P3HT films is presented below: On a hydrophobic surface, it is likely the hydrophobic side chains can interact with the substrate surface more favorably, while the thiophene ring in the backbone interacts more favorably with neighboring thiophene ring in the backbone (π-π stacking etc.), therefore the P3HT backbone rings stand up more on a hydrophobic substrate surface. Differently, on a hydrophilic surface, the hydrophilic surface will interact more favorably with the thiophene backbone ring and thus perturb the intermolecular interaction of the different thiophene rings in the backbone, leading to an orientation that lies down more.

2.3.4. Further Discussion

Interestingly, the observed P3KHT molecular behavior differences at different buried polymer/substrate interfaces are similar to those of P3HT. That is, P3KHT stands more at a P3KHT/hydrophobic interface and lies down more at a P3KHT/hydrophilic interface. It can be

explained as follows: P3KHT has a more hydrophilic side chain that consists of a hydrophilic COOK end group and a hydrophobic alkyl chain. Therefore, this side chain may favorably interact with both hydrophobic and hydrophilic substrates, enabling the P3KHT backbone ring to stand up more at the interfaces. This is true: compared to the PPP signal from P3HT (Fig 2-15a), the PPP signal intensity from P3KHT is weaker, showing that the P3KHT side chains more favorably interact with the substrates, and the polythiophene rings in the backbone of P3KHT stand up more at the buried interface compared to P3HT molecules. For the P3KHT film itself on the two different substrate surfaces, likely the (hydrophobic part of the) side chain interacts with the hydrophobic substrate more favorably, therefore P3KHT backbone ring stands up more at the hydrophobic interface compared to the hydrophilic interface. Due to the (relatively) favorable interactions between the P3KHT side chain with a hydrophilic surface, the substrate hydrophilic surface functionality would not interfere with the polythiophene backbone ring interactions, therefore the P3KHT backbone ring stands up more at the interface, even more than the case of P3HT on a hydrophobic substrate surface. Previous research indicated that the P3HT crystallinity can be affected by the interfacial interaction.[51,52] Our results reported here demonstrated that the interfacial and surface structures are correlated.

Such polythiophene orientations at the buried interfaces influence the bulk P3HT orientations as well as the orientations on surface in air. The more standing up orientation of P3HT thiophene rings at the hydrophobic substrate interface could lead to a better crystallinity in the P3HT film bulk as well as a more standing up orientation on the film surface in air. Oppositely, the more lying down orientation of P3HT thiophene rings at the hydrophilic interface could lead to a less crystalized film and more tilted orientation of thiophene rings on the surface in air.

For P3KHT films, similar to P3HT films, the more standing up orientation of thiophene rings at the hydrophobic substrate interface could lead to a more standing up orientation on the film surface in air. Also, the more lying down orientation of thiophene rings at the hydrophilic interface could lead to a more tilted orientation of thiophene rings on the surface in air. Different from the P3HT films, no crystallinity was observed from P3KHT films using X-ray diffraction. However, we believe that the P3KHT films are not entirely amorphous; otherwise all the surface structures in air should be the same, regardless of the substrate hydrophobicity. The absence of X-ray diffraction pattern is likely due to the small degrees of crystallinity of the P3KHT films.

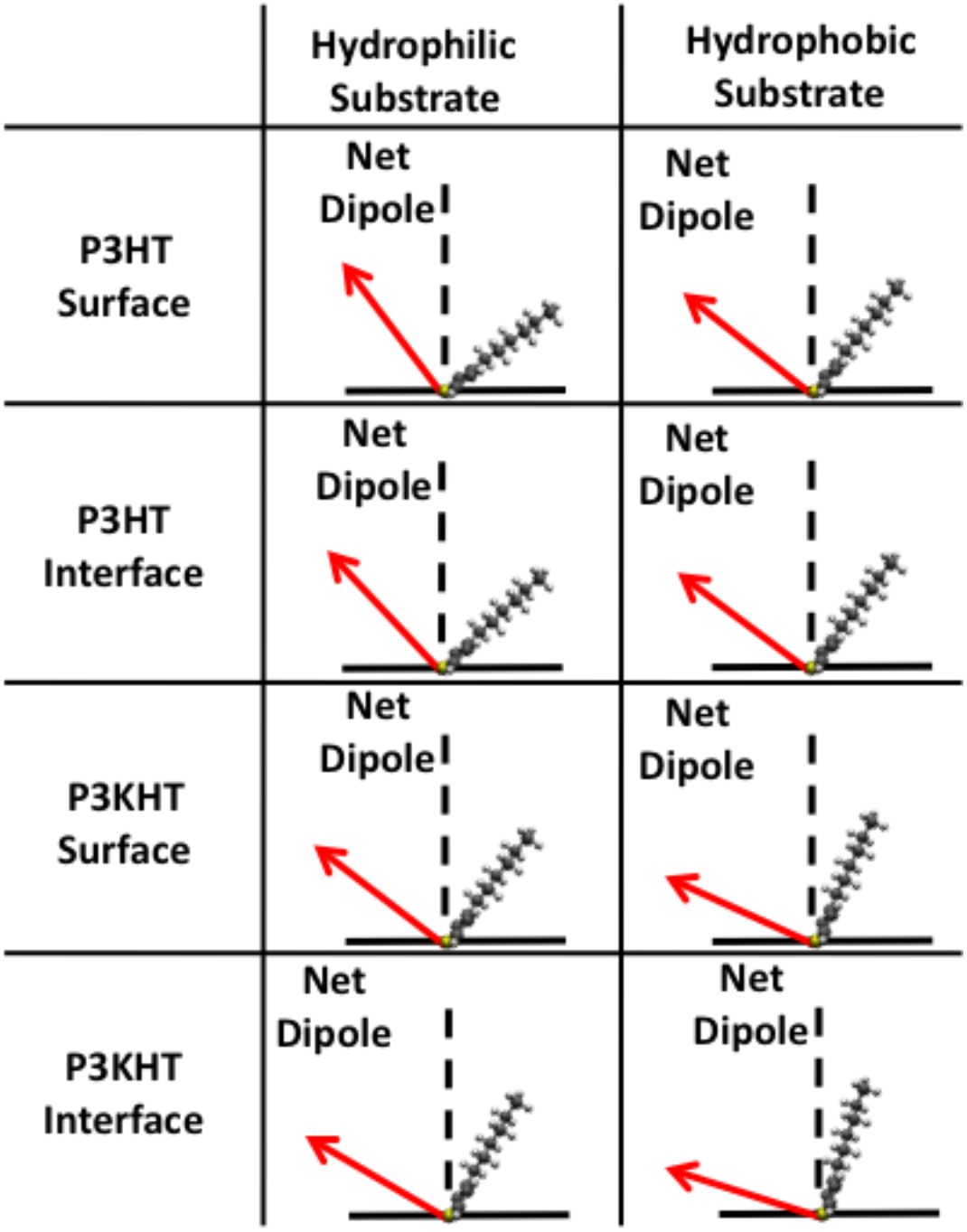

Figure 2-16. Schematics showing P3HT and P3KHT backbone orientations on surfaces and at interfaces as a function of polymer sidechain hydrophobicity and substrate hydrophobicity

For clarity, Figure 2-16 shows schematics of P3HT and P3KHT thiophene backbones on surfaces and at buried interfaces as a function of side chain hydrophobicity and substrate surface hydrophobicity. According to previous studies, it was believed that at buried interfaces, the standing-up P3HT polythiophene backbones can facilitate hole transportation, while a lying down P3HT backbone geometry may dampen hole transportation. Our results on P3HT backbone orientation at the buried interfaces are well correlated to those published previously, that is, P3HT backbones at the P3HT/hydrophobic substrate interface stand up more and they lie down more at the P3HT/hydrophilic substrate interfaces.[20,35]

2.4. Conclusion

It was widely known that the performance of organic semiconductors depends on numerous factors, but there is no consensus yet how those factors influence organic semiconductors from a structural perspective. Here three major factors that may influence the performance of organic semiconductor thin films including solvent used for thin film preparation, polymer side chain composition, and polymer film substrate hydrophobicity were investigated. Their effects on the surface, interface and bulk structure of polythiophene films were elucidated.

We first systematically studied the solvent effect on P3HT films using various techniques. SFG results indicate that both the surface and interfacial ordering increased when poor solvent acetone is blended into the P3HT solution to prepare the P3HT thin films. At the same time, X-ray diffraction results show that the thin film bulk crystallinity also increased when more and more poor solvent was added to the P3HT solution. This study clearly demonstrated that the poor solvent introduced to the P3HT solution influences the resulting P3HT thin films. Changes were observed in surface morphology, surface ordering, interfacial ordering, and bulk crystallinity.

Effects of dielectric underneath layer and side chain on PT polymers were then further studied. It was found that different polythiophene molecule can induce varied interactions between polythiophene and substrate surface, leading to different orientations. With a hydrophilic group terminated alkyl side chain, the polythiophene backbone at the buried interface (regardless of the substrate surface hydrophobicity) could stand up more compared to P3HT at the P3HT/substrate interface. For the same PT molecule, its backbone lies down more on hydrophobic surfaces regardless of the side chain property on the molecule.

The determination of molecular structures of PT films at buried interfaces is significant. The deduced buried interfacial structures can be well correlated to the performance of devices fabricated with PT films, which will be presented in the next chapter.

For more details of the work described in this chapter, please refer to the original publication.[53,54]

2.5. References

(1) Garnier, F.; Hajlaoui, R.; Yassar, A.; Srivastava, P. *Science* **1994**, *265*, 1684.

(2) Bao, Z.; Lovinger, A. J. *Chemistry of Materials* **1999**, *11*, 2607.

(3) Lobez, J. M.; Andrew, T. L.; Bulović, V.; Swager, T. M. *ACS Nano* **2012**, *6*, 3044.

(4) Goffri, S.; Müller, C.; Stingelin-Stutzmann, N.; Breiby, D. W.; Radano, C. P.; Andreasen, J. W.; Thompson, R.; Janssen, R. A. J.; Nielsen, M. M.; Smith, P. *Nature materials* **2006**, *5*, 950.

(5) Ha, J. S.; Kim, K. H.; Choi, D. H. *Journal of the American Chemical Society* **2011**, *133*, 10364.

(6) Street, R. A.; Northrup, J. E.; Salleo, A. *Physical Review B* **2005**, *71*, 165202.

(7) Hoeben, F. J. M.; Jonkheijm, P.; Meijer, E. W.; Schenning, A. P. H. J. *Chemical Reviews* **2005**, *105*, 1491.

(8) Coropceanu, V.; Cornil, J.; da Silva Filho, D. A.; Olivier, Y.; Silbey, R.; Brédas, J.-L. *Chemical Reviews* **2007**, *107*, 926.

(9) Bao, Z.; Dodabalapur, A.; Lovinger, A. J. *Applied Physics Letters* **1996**, *69*, 4108.

(10) Kline, R. J.; McGehee, M. D.; Kadnikova, E. N.; Liu, J.; Fréchet, J. M. J. *Advanced Materials* **2003**, *15*, 1519.

(11) Shkunov, M.; Simms, R.; Heeney, M.; Tierney, S.; McCulloch, I. *Advanced Materials* **2005**, *17*, 2608.

(12) Kao, C. Y.; Lee, B.; Wielunski, L. S.; Heeney, M.; McCulloch, I.; Garfunkel, E.; Feldman, L. C.; Podzorov, V. *Advanced Functional Materials* **2009**, *19*, 1906.

(13) Locke, J. R.; McNeil, A. J. *Macromolecules* **2010**, *43*, 8709.

(14) Lobez, J. M.; Andrew, T. L.; Bulovic, V.; Swager, T. M. *ACS nano* **2012**, *6*, 3044.

(15) Hamadani, B. H.; Corley, D. A.; Ciszek, J. W.; Tour, J. M.; Natelson, D. *Nano letters* **2006**, *6*, 1303.
(16) Calhoun, M. F.; Sanchez, J.; Olaya, D.; Gershenson, M. E.; Podzorov, V. *Nature materials* **2008**, *7*, 84.
(17) Wobkenberg, P. H.; Ball, J.; Kooistra, F. B.; Hummelen, J. C.; de Leeuw, D. M.; Bradley, D. D. C.; Anthopoulos, T. D. *Applied Physics Letters* **2008**, *93*, 13303.
(18) Ito, Y.; Virkar, A. A.; Mannsfeld, S.; Oh, J. H.; Toney, M.; Locklin, J.; Bao, Z. *Journal of the American Chemical Society* **2009**, *131*, 9396.
(19) Ong, B. S.; Wu, Y.; Liu, P.; Gardner, S. *Journal of the American Chemical Society* **2004**, *126*, 3378.
(20) Sirringhaus, H.; Brown, P. J.; Friend, R. H.; Nielsen, M. M.; Bechgaard, K.; Langeveld-Voss, B. M. W.; Spiering, A. J. H.; Janssen, R. A. J.; Meijer, E. W.; Herwig, P. *Nature* **1999**, *401*, 685.
(21) Kim, D. H.; Park, Y. D.; Jang, Y.; Yang, H.; Kim, Y. H.; Han, J. I.; Moon, D. G.; Park, S.; Chang, T.; Chang, C. *Advanced Functional Materials* **2005**, *15*, 77.
(22) Kim, Y.; Choulis, S. A.; Nelson, J.; Bradley, D. D. C.; Cook, S.; Durrant, J. R. *Applied Physics Letters* **2005**, *86*, 063502.
(23) Chang, M.; Choi, D.; Fu, B.; Reichmanis, E. *ACS nano* **2013**, *7*, 5402.
(24) O'Brien, D. B.; Anglin, T. C.; Massari, A. M. *Langmuir* **2011**, *27*, 13940.
(25) Li, Q.; Hua, R.; Chou, K. C. *The Journal of Physical Chemistry B* **2008**, *112*, 2315.
(26) Bryan, Z. J.; Smith, M. L.; McNeil, A. J. *Macromolecular rapid communications* **2012**, *33*, 842.
(27) Zhang, C.; Myers, J. N.; Chen, Z. *Soft matter* **2013**, *9*, 4738.
(28) Zhang, C.; Shephard, N. E.; Rhodes, S. M.; Chen, Z. *Langmuir* **2012**, *28*, 6052.
(29) Dhar, P.; Khlyabich, P. P.; Burkhart, B.; Roberts, S. T.; Malyk, S.; Thompson, B. C.; Benderskii, A. V. *The Journal of Physical Chemistry C* **2013**, *117*, 15213.
(30) Taliani, C.; Danieli, R.; Zamboni, R.; Ostoja, P.; Porzio, W. *Synthetic Metals* **1987**, *18*, 177.
(31) Wang, J.; Chen, C.; Buck, S. M.; Chen, Z. *The Journal of Physical Chemistry B* **2001**, *105*, 12118.
(32) Günes, S.; Neugebauer, H.; Sariciftci, N. S. *Chemical reviews* **2007**, *107*, 1324.
(33) Zhang, D.; Dougal, S. M.; Yeganeh, M. S. *Langmuir* **2000**, *16*, 4528.
(34) Chen, Z.; Shen, Y. R.; Somorjai, G. A. *Annual review of physical chemistry* **2002**, *53*, 437.
(35) Anglin, T. C.; Speros, J. C.; Massari, A. M. *The Journal of Physical Chemistry C* **2011**, *115*, 16027.
(36) Zen, A.; Pflaum, J.; Hirschmann, S.; Zhuang, W.; Jaiser, F.; Asawapirom, U.; Rabe, J. P.; Scherf, U.; Neher, D. *Advanced Functional Materials* **2004**, *14*, 757.
(37) Myers, J. N.; Zhang, X.; Bielefeld, J. D.; Lin, Q.; Chen, Z. *The Journal of Physical Chemistry B* **2015**.
(38) Hankett, J. M.; Lu, X.; Liu, Y.; Seeley, E.; Chen, Z. *Physical Chemistry Chemical Physics* **2014**, *16*, 20097.
(39) Yang, H.; Shin, T. J.; Yang, L.; Cho, K.; Ryu, C. Y.; Bao, Z. *Advanced Functional Materials* **2005**, *15*, 671.
(40) Ross, R. B.; Cardona, C. M.; Guldi, D. M.; Sankaranarayanan, S. G.; Reese, M. O.; Kopidakis, N.; Peet, J.; Walker, B.; Bazan, G. C.; Van Keuren, E. *Nature materials* **2009**, *8*, 208.
(41) Keen, I.; Rintoul, L.; Fredericks, P. M. *Applied Spectroscopy* **2001**, *55*, 984.
(42) Keen, I.; Rintoul, L.; Fredericks, P. M. In *Macromolecular Symposia*; John Wiley & Sons: 2002; Vol. 184, p 287.
(43) Moad, A. J.; Simpson, G. J. *The Journal of Physical Chemistry B* **2004**, *108*, 3548.
(44) Xiao, M.; Zhang, X.; Bryan, Z. J.; Jasensky, J.; McNeil, A. J.; Chen, Z. *Langmuir* **2015**, *31*, 5050.

(45) Lu, X.; Shephard, N.; Han, J.; Xue, G.; Chen, Z. *Macromolecules* **2008**, *41*, 8770.
(46) Icenogle, H. W.; Platt, B. C.; Wolfe, W. L. *Applied optics* **1976**, *15*, 2348.
(47) Lee, W. H.; Chuang, S. Y.; Chen, H. L.; Su, W. F.; Lin, C. H. *Thin Solid Films* **2010**, *518*, 7450.
(48) Lu, X.; Li, B.; Zhu, P.; Xue, G.; Li, D. *Soft matter* **2014**, *10*, 5390.
(49) Liu, W.-T.; Shen, Y. R. *Proceedings of the National Academy of Sciences* **2014**, *111*, 1293.
(50) Lu, X.; Xue, G.; Wang, X.; Han, J.; Han, X.; Hankett, J.; Li, D.; Chen, Z. *Macromolecules* **2012**, *45*, 6087.
(51) Kline, R. J.; McGehee, M. D.; Toney, M. F. *Nature Materials* **2006**, *5*, 222.
(52) Ho, P. H.; Chua, L. L.; Dipankar, M.; Gao, X.; Qi, D.; Wee, A. S.; Chang, J. F.; Friend, R. H. *Advanced Materials* **2007**, *19*, 215.
(53) Xiao, M.; Zhang, X.; Bryan, Z. J.; Jasensky, J.; McNeil, A. J.; Chen, Z. *Langmuir* **2015**, *31*, 5050.
(54) Xiao, M.; Jasensky, J.; Zhang, X.; Li, Y.; Pichan, C.; Lu, X.; Chen, Z. *Physical Chemistry Chemical Physics* **2016**, *18*, 22089.

CHAPTER 3 Eluciadating Structure-Function Correlation Between Interfacial Molecular Orientation And Power Conversion Efficiency In Perovskite Photovoltaics

Materials covered in this chapter were published in *J. Am. Chem. Soc.* **2017**, 139. This research was in collaboration with Prof. Jay Guo's group.

3.1. Background and Motivation

Organic semiconductors have important applications in photovoltaics. In this chapter, polymer based organic semiconductor polythiophenes (PTs) were incorporated into perovskite photovoltaics to further study how molecular orientations at buried interface would affect the overall performance of perovskite photovoltaics.

Perovskite based photovoltaics were chosen for study here because of the exceptional performance of perovskite in planar heterojunction solar cells. The perovskite solar cell power conversion efficiency (PCE) has increased from 3.8% in 2009 to over 20% last year.[1-3] A typical perovskite photoactive layer has a ABX_3 crystal structure, where A, B, and X are the organic cation, metal cation, and halide anion, respectively.[3] Recent research has shown various approaches that can be adopted to improve properties within the photoactive layer of perovskite, such as tuning bandgap by varying ABX_3's chemical composition,[3-6] using different solvent combinations to prepare the perovskite precursor which affects the perovskite crystal structure during the annealing

process,[7] and adopting rapid cooling rate after annealing to lead to a smooth and compact perovskite layer and to minimize void formation.[8] A typical planar heterojunction perovskite solar cell has a perovskite photoactive layer sandwiched between an electron transport layer (ETL) and a hole transport layer (HTL).[2,3,5,9-15] By absorbing incoming photons, electrons and holes are created inside the perovskite photoactive layer and extracted by the ETL and HTL respectively.

For a perovskite solar cell with a highly crystallized, smooth, and compact photoactive layer, it is believed that device performance is determined by how efficiently charge carriers are transported and extracted across the interfaces by both the ETL and HTL. In an inverted structure perovskite solar cell, the ETL is typically a metal oxide (e.g., zinc oxide, titanium oxide, etc.) and HTL is usually composed of organic molecules, such as Spiro-MeOTAD, benzodithiophene polymer (PTB7), or polythiophene (P3HT).[3,5,16-19] Some of these organic molecules have shown promising performance; the best PCE of those molecules ranges from 10% to 20%. It is relatively straightforward to analyze the structures of the ETL and perovskite photoactive layer due to their high crystallinity. However, structures of both the HTL bulk and the HTL interface are not well known and have remained under debate since the initial studies of organic photovoltaics (OPVs).[20,21] Due to a lack of crystallinity, very few techniques can be used to provide insight or meaningful information about the HTL bulk structure. The bulk structure of an organic layer may be investigated by some X-ray based techniques, e.g., X-ray absorption near edge spectroscopy or XANES, but such techniques can be quite complicated and are synchrotron-based. It is even more challenging to study molecular structure of the HTL interface, due to the lack of appropriate tools which can probe buried interfacial structures in situ. It is believed that interfacial molecular orientation plays a vital role in charge transport, charge separation, and/or charge recombination; the interfacial structure is usually assumed using bulk X-ray diffraction results. Here, for the first

time, we applied SFG [22] to investigate buried interfacial structure between perovskite and the HTL. Because the molecular orientation at the interfaces will ultimately affect the charge carrier dynamic, transient photocurrent (TPC) and transient photovoltage (TPV) would also be used to gain a complete understanding of the charge carrier dynamics and the trapping state density.

3.2. Effect of Interfacial Structure on the Power Conversion Efficiency in Perovskite Photovoltaics

3.2.1. Materials and Methods

All PT derivatives (Poly 3-hexylthiophene (P3HT), Poly 3-octylthiophene (P3OT), Poly 3-decylthiophene (P3DT), Poly 3-dodecylthiophene (P3DDT)) were purchased from Rieke Metals, and used as received. Methylammonium iodide (MAI) was ordered from Dyesol, and was also used as received. Lead chloride was bought from Aldrich-Sigma and was used without further purification. The TiO_2 layer was synthesized via a sol-gel method.[9] ITO glass substrates were sequentially washed with acetone, isopropanol, and distilled water (15 min each, assisted with ultra-sonication). ITO glass was further cleaned by a 2 min glow discharge oxygen plasma. The TiO_2 sol-gel precursor was then spin-coated onto the ITO substrate at 2000 r.p.m for 1 min to prepare the TiO_2 ETL. The TiO_2 ETL on ITO glass was then annealed in air at 150 °C for 15 min, followed by 500 °C for 30 min. The perovskite precursor solution (both 278 mg $PbCl_2$ and 478 mg MAI were dissolved in 1.7 g DMF, mixed at 70 °C overnight before use) was then spin-coated onto the TiO_2 coated ITO glass at 2000 r.p.m. for 60 s in a nitrogen-filled glovebox. After that, the spin coated perovskite layer was annealed at 110 °C for 60 min. After cooling down, the PT derivatives (P3HT at 1.5 wt%, P3OT at 1.75 wt%, P3DT at 2.0 wt%, P3DDT at 2.25 wt%) were spin coated onto the perovskite layer at 1500 r.p.m for 45 s. Finally, the counter electrode was deposited by thermal evaporation of silver (100 nm) with a thermal evaporator at a pressure of 3×10^{-6} Torr.

Samples for SFG experiments were prepared in the same fashion but without silver deposition. To probe the buried interface using SFG, a layer of spin coated poly (methyl methacrylate) (PMMA) (5 wt% in dichloromethane (DCM), spin coated at 1500 r.p.m. for 1 min) was deposited on top of the PT layer prepared for SFG study. Different PT film thickness is achieved by varying concentrations of PT solutions. SFG spectra were then collected from such samples using different polarizations of the input and output beams. SEM samples were prepared by spin coating PTs onto the perovskite surfaces and SEM images were obtained using a JEOL-7800FLV Scanning Electron Microscope. Film thickness was measured by a depth profilometer (Dektak 6M stylus Surface Profilometer, Veeco). The film thickness of a PT layer was deduced by taking the difference between the perovskite/PT film thickness and the pure perovskite film thickness.

PT derivatives spin-coated on quartz slides were used for UV-Vis spectroscopy. Spectra were collected using a Shimadzu UV-1601 UV-Vis spectrometer. Quartz slides were washed with acetone, isopropanol, contrex, and distilled water (15 min each, assisted with ultra-sonication), followed by a 1 min glow discharge oxygen plasma treatment.

3.2.2. Elucidating Interfacial Structure between Hole Transport Layer and Perovskite Photoactive Layer

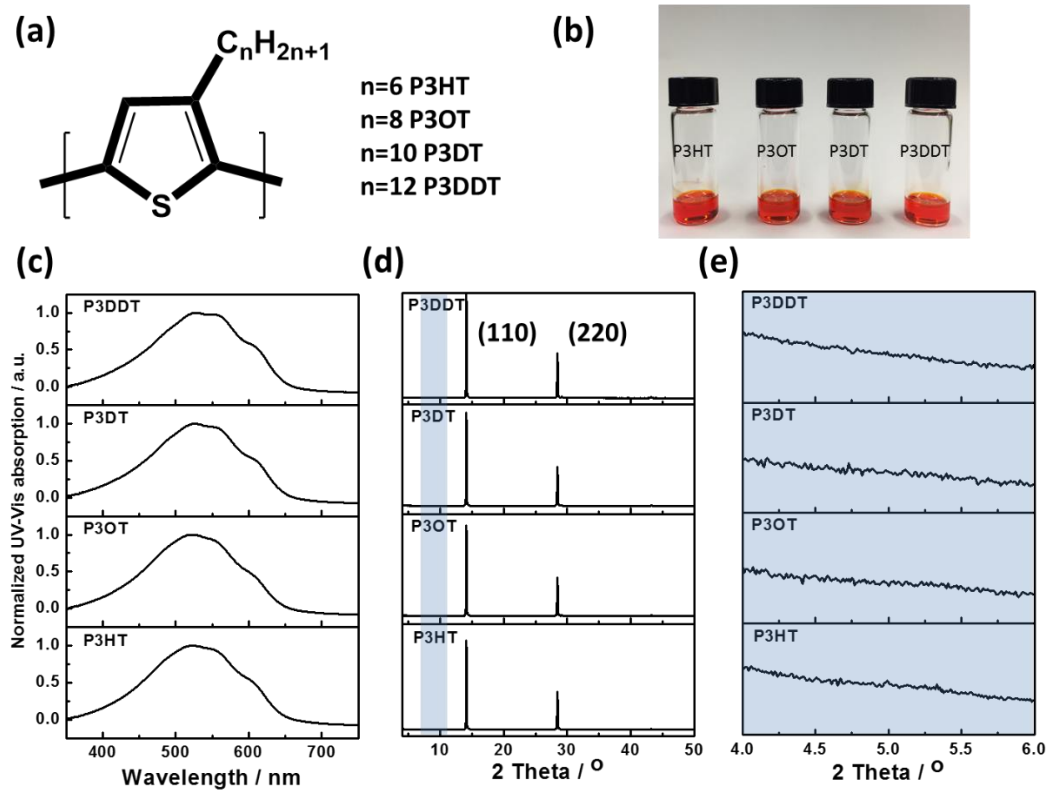

Figure 3-1 (a) Chemical formula of the PT derivatives used as the HTL material in this study; (b) PT derivatives dissolved in chlorobenzene show identical solution color; (c) UV-Vis spectra of spin coated PT derivative thin films; (d) X-ray diffraction patterns of fabricated perovskite solar cells without silver electrodes; (e) Zoomed in X-ray diffraction signals at 2 theta ranging from 4.0° to 6.0° of corresponding signals shown in (d).

As shown in Figure 3-1a, all PT derivatives used in this study only differ in their alkyl sidechain length. Because the electric and optical properties of organic conjugate molecules rely heavily on their conjugated structure and the conjugated length, altering the alkyl sidechain length of the material used for the PT layer may not strongly affect such properties. Therefore, all PT derivatives utilized here should share a similar band structure. Figure 3-1b and c indicated similar

optical properties of all the PT derivatives in the visible light frequency range. All PT derivatives showed an identical orange color in solution (Fig 3-1b). Measuring UV-Vis absorption of PT thin films indicated a common major absorption peak around 510 nm and a shoulder peak around 600 nm (Fig 3-1c).[23-25] Bandgap of a PT derivative determines its hole-extracting nature at its contact with perovskite. Because of the similar absorption behavior in the visible range, the different PT derivatives utilized here are expected to have a similar band structure. A different band alignment can affect charge carrier transportation across the interface by changing open-circuit voltage, or it can even create a barrier to charge transport, and therefore affect the overall PCE in a solar cell device. Here, because of the identical bandgap alignment in all the PT derivatives studied, the bandgap effect on PCE can be neglected. Since all the four PT derivatives showed almost identical UV-Vis spectral features, we believe that they should have similar bulk structure. Previous studies showed controversial results on the side chain length and hole mobility correlation for thiophene based materials. Some stated that longer sidechains have lower hole mobility, while it was also suggested that on certain substrates, chain length does not appreciably affect mobility. Here in our case, because the HTL film thickness is only 100 nm, we believed that the bulk PT mobility difference can be ignored.[26]

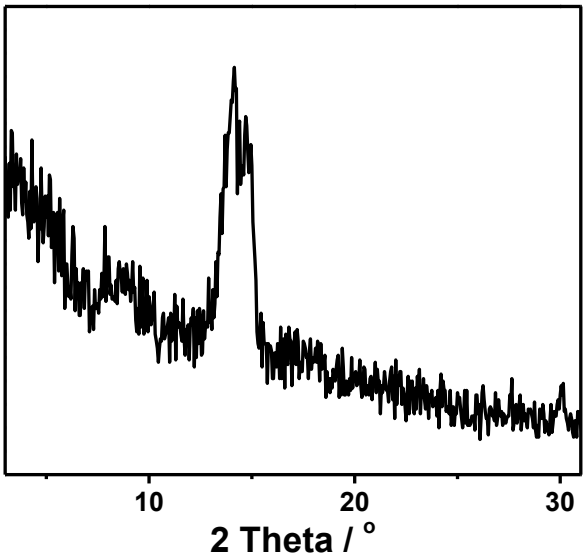

Figure 3-2 GIXRD spectra of P3HT on perovskite surface

Bulk structures of different materials will also affect the efficiency of charge carriers transported across these films, and therefore have an impact on solar cell PCE. Figure 3-1d shows X-ray diffraction patterns of fabricated perovskite solar cells without silver electrodes. These X-ray diffraction patterns contain large contributions from the perovskite (110) plane.[24,27,28] Figure 3-1e shows an enlarged section of Figure 3-1d with 2 theta ranging from 4.0° to 6.0°. This range was chosen based on previously reported poly (3-hexylthiophene) (P3HT) X-ray diffraction patterns, where polycrystalline P3HT was shown to have an X-ray diffraction peak around 5.2°.[29-33] In this study, none of the PT derivatives showed any visible X-ray diffraction pattern on top of the perovskite surface, indicating low crystallinity of the HTL prepared with all PT derivatives. Most organic semiconducting polymers are polycrystalline, but the observed X-ray diffraction pattern here showed that all the PT films are mostly amorphous with a very low degree of

crystallinity. In addition to powder X-ray diffraction, grazing incidence X-ray diffraction (GIXRD) was also used to study bulk structures within the PT. GIXRD is believed to have better sensitivity for thin film materials since X-rays propagate through the film. However, no visible peak of any PT layers was observed (Figure 3-2 presents the GIXRD results). Both powder X-ray diffraction and GIXRD results suggest that crystallinity inside the PT layer was very low. We therefore conclude that the PT polymers were mostly amorphous with minimal degree of crystallinity, and such a conclusion can be generalized to all PT derivatives used in this study.

Beside the bulk properties of the PT HTL, X-ray diffraction patterns can also be used to study perovskite thin film orientation. According to Figure 3-1d, the perovskite film has the (110) crystal plane in parallel to the film surface (defined as the x-y plane). While the optical properties and bulk properties can be studied with UV-visible spectroscopy and X-ray diffraction, information regarding the interfacial molecular structure is still lacking. As we reported above, both optical and bulk properties of different HTLs prepared with PT derivatives with different side chain lengths are nearly identical.

We then studied molecular structures of PT derivatives at the interface between the HTL and perovskite. As stated in the introduction section, molecular orientation at buried interfaces can be deduced by the signals detected using sum frequency generation spectroscopy (SFG) with different polarization combinations of the input and signal photons. To facilitate analysis of the interfacial structures at the PT/perovskite interface, a PMMA capping layer was deposited on top of the PT layer. Dichloromethane (DCM), a poor solvent for P3HT, was chosen for casting PMMA in an effort to minimize any changes to P3HT layer in a P3HT/PCBM bilayer organic solar cell.[24,34]

With the PMMA capping layer, Fresnel coefficients of different $\chi^{(2)}$ components as a function of PT film thickness at both interface I (the PMMA/PT interface) and interface II (the

PT/perovskite interface) are shown in Figure 3-3. Detected SFG signals from the layered structures shown in Figure 3-3c are originated from both interface I and II. In order to extract the SFG response from only interface II (or the $\chi^{(2)}$ component of interface II), SFG spectra were collected from samples with at least two different PT film thicknesses. Here, thicknesses of 60 nm and 100 nm were chosen for study. Corresponding Fresnel coefficient values of both interfaces at the PT film thickness of 60 nm and 100 nm can be obtained from Figure 3-3 (χ_{ssp} probes χ_{yyz}, χ_{sps} probes χ_{yzy}). These values are used to deduce the value of $\chi^{(2)}$ from interface II.

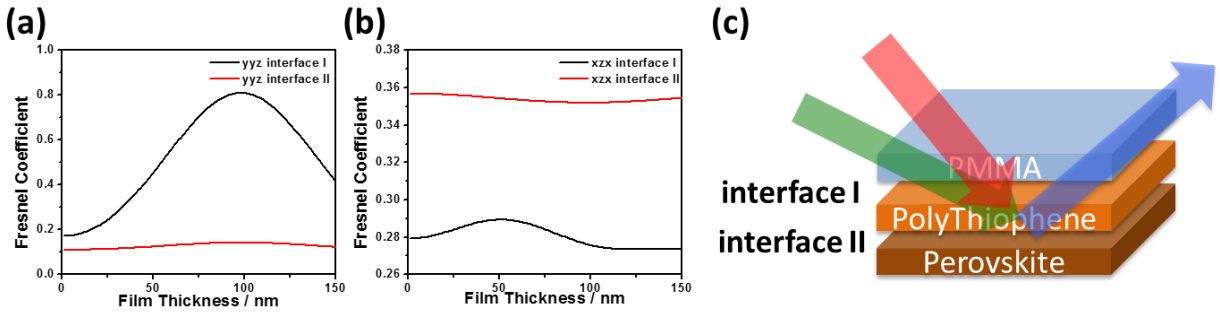

Figure 3-3 (a) Fresnel coefficient of the χ_{yyz} component as a function of the PT layer film thickness (PMMA/PT/perovskite tri-layer sample); (b) Fresnel coefficient of χ_{yzy} component as a function of PT layer film thickness (PMMA/PT/perovskite tri-layer sample); (c) Illustration of interface I and interface II defined in the SFG experiment. All three layers are separated for clarity.

Figure 3-4 shows SFG spectra of both ssp and sps polarizations collected from all PT derivatives. The peaks of interest are the C=C symmetric stretches in the thiophene five-member ring at 1430 cm^{-1}; and such a symmetric five-member thiophene ring has a C_{2v} symmetry. It has been extensively studied that such a C=C symmetric stretch has a net transition dipole moment pointing perpendicular to the planar PT backbone. The smaller shoulder at 1375 cm^{-1} is the C-C v_s

(ring) stretch, and both peaks are consistent with previous studies.[35-37] It is worth mentioning that the SFG spectra have contributions from both interfaces I and II. By incorporating the calculated Fresnel coefficients into the overall SFG spectra, one can selectively deduce and reconstruct the χ_{yyz} and χ_{yzy} components from the interface of interest. Here, we are more interested in the interface between PT and perovskite: interface II. Using the fitted data, we can calculate the ratio of χ_{yyz}/χ_{yzy} for interface II, from which we can deduce the orientation of the PT at that interface. Figure 3-4k shows the correlation between deduced χ_{yyz}/χ_{yzy} value and the PT back orientation.

Interestingly, the measured χ_{yyz}/χ_{yzy} ratio showed an increasing trend with increasing length of the PT alkyl sidechain. The smallest χ_{yyz}/χ_{yzy} measured is 0.36 with P3HT, while the largest χ_{yyz}/χ_{yzy} is 3.72 obtained with P3DDT. Using these experimentally-measured χ_{yyz}/χ_{yzy} values and their correlations, plotted in Figure 3-4k, we can determine the backbone orientations of PT molecules at the buried PT/perovskite interface. The P3HT polythiophene backbone orientation was deduced to be roughly 20° with respective to the surface normal, increasing to about 60° for P3DDT. Apparently, the thiophene backbone of P3HT adopts a more normal (up-right) orientation on the perovskite (110) crystal plane, and P3DDT's thiophene backbone lies more tangentially (flat). The angles of P3OT and P3DT lie in between those of P3HT and P3DDT. Therefore, for PT molecules on the perovskite (110) plane, in all the four PT derivatives examined here, the shorter the alkyl side chain, the more up right orientation the PT's backbone would have. We have not investigated the behavior of the PT side chain at the buried PT/perovskite interface, because perovskite methyl groups may also contribute to the C-H stretching signals, which will overlap with the side chain SFG signal. Here it is more important to study the thiophene backbone because in organic semiconductors, only the conjugated system is responsible for charge carrier extraction and transportation. We believe that this thiophene backbone will be the dominant factor for the

entire hole extraction process across the PT/perovskite interface. Detailed fitting parameters can be found in the original publication.[38]

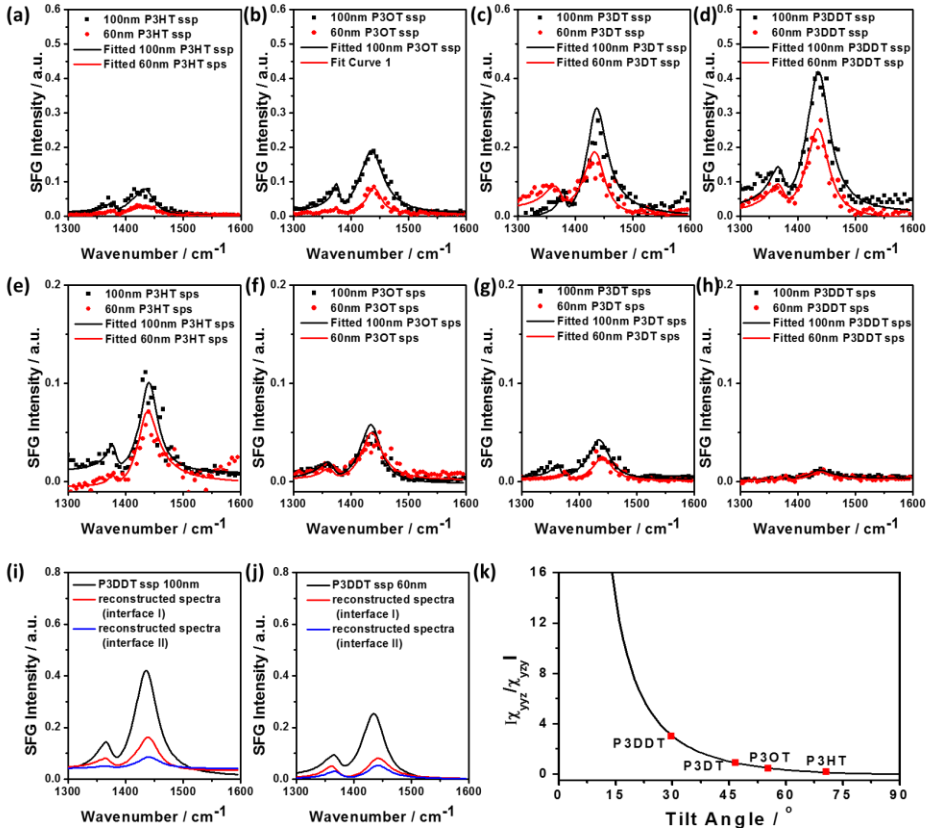

Figure 3-4 SFG ssp spectra collected from a PT thin film sandwiched between PMMA and perovskite: (1) P3HT, (b) P3OT, (c) P3DT, and (d) P3DDT; SFG sps spectra collected from the same samples: (e) P3HT, (f) P3OT, (g) P3DT and (h) P3DDT; The reconstructed spectra including the overall spectrum and the spectra for interfaces I and II for P3DDT, ssp: (i) P3DDT film of 100 nm, (j) P3DDT film of 60 nm. (k) χ_{yyz}/χ_{yzy} ratio as a function of the tilt angle of the net transition dipole of the thiophene ring C=C stretch (with respect to the surface normal)

	1435 cm^{-1} Peak	
	Peak width	Peak Amplitude

P3HT ssp 100nm	22.0	7.48
P3HT ssp 60nm	22.2	5.50
P3HT sps 100nm	22.1	6.85
P3HT sps 60nm	21.9	5.91

Table 3-1 Fitting parameters of Figure 3-4 a, e

	1435 cm^{-1} Peak	
	Peak width	Peak Amplitude
P3OT ssp 100nm	22.0	9.68
P3OT ssp 60nm	22.0	7.26
P3OT sps 100nm	22.0	5.28
P3OT sps 60nm	22.0	4.80

Table 3-2 Fitting parameters of Figure 3-4 b, f

	1435 cm^{-1} Peak	
	Peak width	Peak Amplitude
P3DT ssp 100nm	22.0	12.32
P3DT ssp 60nm	22.0	9.24
P3DT sps 100nm	22.0	4.40
P3DT sps 60nm	22.0	3.72

Table 3-3 Fitting parameters of Figure 3-4 c, g

	1435 cm^{-1} Peak	
	Peak width	Peak Amplitude
P3DDT ssp 100nm	22.0	15.43
P3DDT ssp 60nm	22.0	12.10
P3DDT sps 100nm	22.0	3.52
P3DDT sps 60nm	22.0	3.08

Table 3-4 Fitting parameters of Figure 3-4 d, h

3.2.3. Perovskite Photovoltaics' Power Conversion Efficiency and Other Electronic Properties

After we characterized the optical properties of the HTL on perovskite using UV-Vis spectroscopy, the bulk structure and crystallinity using X-ray diffraction, and the interface structure using SFG, we fabricated perovskite solar cell devices with a structure shown in Figure 3-5 to test how various PT derivatives would affect overall device PCE. Detailed fabrication methods were reported in the Materials and Methods (3.2.1.) section above. Figure 3-5 shows the

PCE from the champion cell made with each PT derivative. All PT derivatives showed almost identical V_{oc} around 0.8 V, with FF factors calculated at or above 50% (Detailed V_{oc}, J_{sc}, FF values are listed in Table 3-5). While the bandgap difference between the HTL (ETL) and the photoactive layer is believed to dominate V_{oc} in a solar cell, the above result proves the same bandgap alignment for different solar cells made using different PTs as reported in Figure 3-1. Interestingly, different solar cells using different PTs have very different J_{sc} values. P3HT with the most edge up orientation has a J_{sc} of 21.22 mA while P3DDT with the most lying down orientation has a J_{sc} of 9.3 mA.

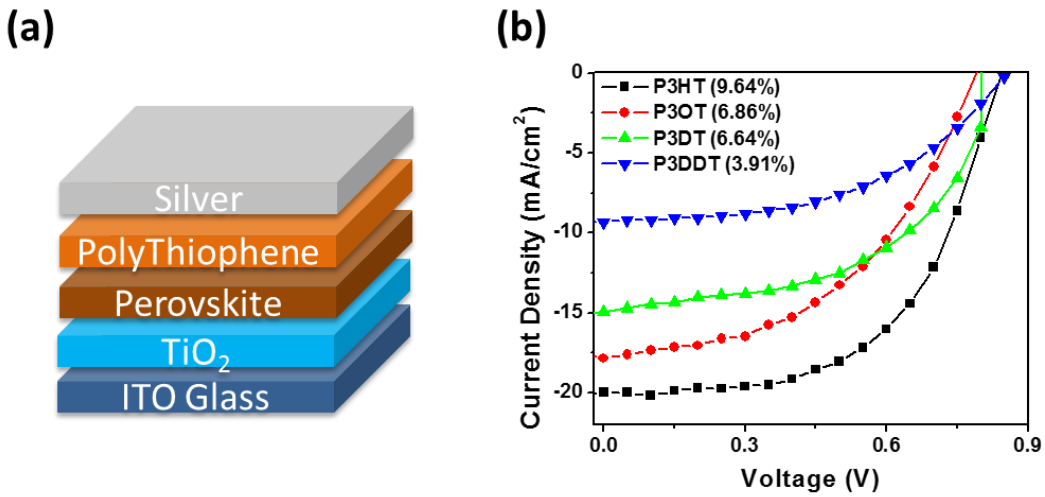

Figure 3-5 (a) Schematic showing the cross section of a fabricated perovskite solar cell; (b) J-V curves under AM 1.5 illumination of solar cell devices fabricated with various PT derivatives.

HTL material	V_{oc} (V)	J_{sc} (mA/mc^2)	FF	PCE (%)
P3HT	0.82	19.97	58.88%	9.64
P3OT	0.79	17.84	48.66%	6.86
P3DT	0.83	14.96	53.43%	6.64
P3DDT	0.85	9.31	49.44%	3.91

Table 3-5 Photovoltaic performance of perovskite solar cells fabricated with different HTL materials.

3.2.4. Further Discussion

For a photovoltaic device, the interface between the perovskite layer and HTL is where holes are extracted. Solar cells prepared with different PT derivatives having different side chains in this study contain identical ETL and perovskite layers. The different PT orientations at the interface in these solar cells affect the hole transporting process. Because holes are transported through HOMO-HOMO orbitals, the relative orientation between HOMO-HOMO orbitals as a result of different PT orientations becomes the key for solar cell performance. According to previously studied HOMO electron orbitals of both P3HT and lead iodine based perovskite,[39,40] HOMO-HOMO electron orbital would overlap better with a lying down PT thiophene backbone orientation. Therefore, an edge-on thiophene backbone would lead to a greater offset of HOMO-HOMO between perovskite and PTs. Our experimental data obtained above shows that the solar cell made with PT with a more normal (edge-on or standing up) thiophene backbone orientation at the interface has 2 times higher J_{sc} than that made of PT with a more tangential (lying down) thiophene backbone. We therefore believe that an off-set HOMO-HOMO alignment between the perovskite

and HTL is better for hole extraction at such an interface, while a more overlapped HOMO-HOMO between perovskite and HTL would possibly lead to more electron-hole recombination at the interface, meaning that holes extraction at the perovskite/HTL interface is far less efficient.

To better understand the charge carrier lifetime and trap density, transient photovoltage (TPV) and transient photocurrent (TPC) experiments were performed on devices fabricated with P3HT and P3DDT respectively (Figure 3-6). As TPV results show, the device fabricated with P3HT has a longer charge carrier lifetime compared to that fabricated with P3DDT. The TPC result shows a longer decay for the device fabricated with P3DDT compared to that of P3HT, indicating a more dense trapping state in the device fabricated with P3DDT. Because the TPC experiment was performed on an entire photovoltaic device, it is difficult to distinguish the trap at the perovskite/PT interface from the trap in the PT layer (bulk). If the trapping state at the interface plays a role, the orientation of PT backbone may also have a direct correlation with the abundance of the trapping state.[3,41-44]

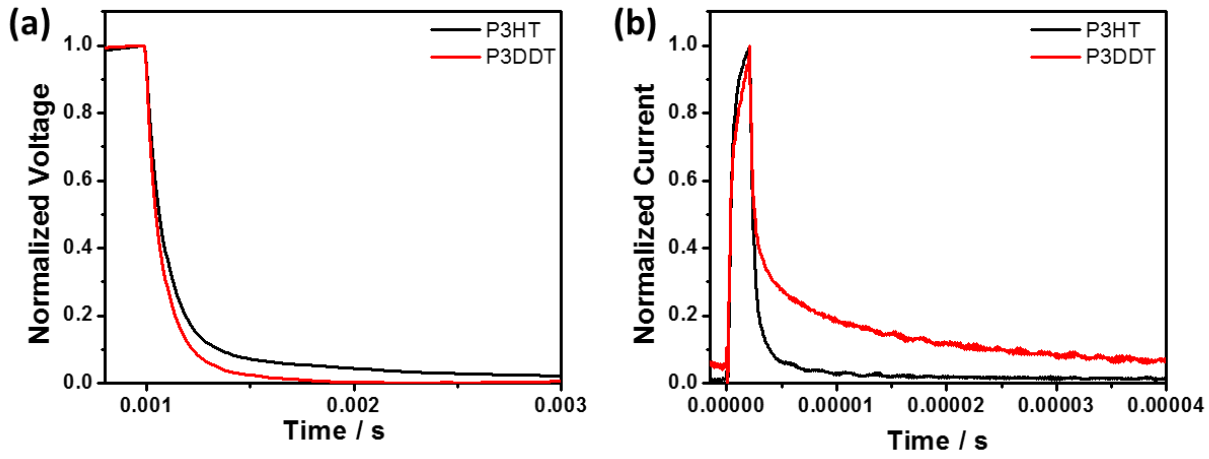

Figure 3-6 (a) Transient photovoltage of devices fabricated with P3HT and P3DDT under illumination; (b) Transient photocurrent of devices fabricated with P3HT and P3DDT under illumination. (All TPC and TPV measurements are conducted under the same intensity illumination)

Previous studies have investigated interfacial structures in photovoltaic applications. For example, Alex A. L. et al. proposed a LUMO-LUMO offset between CuPc and C_{60} can have four times different electron transfer rate in different orientations, [20] with a similar claim being made by Rand B. P. et al.[21] We believe that the optimized orientation of PT molecules at interfaces for photovoltaic applications are different case by case, but this orientation may result in different electron orbital alignments, which is the key to answering why molecular orientation is crucial to photovoltaic device performance.

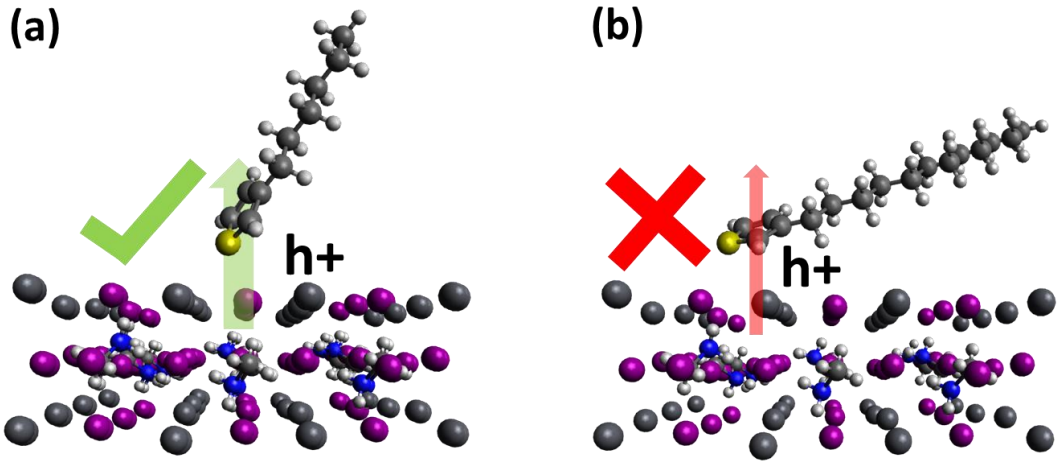

Figure 3-7 Illustration of hole extraction ability of (a) PTs with shorter alkyl sidechain and (b) PTs with longer alkyl sidechain at the HTL/perovskite interface.

3.3. Conclusion

We have investigated the interfacial orientations of PT molecules with different side chain lengths at the PT/perovskite buried interface and their correlation with the performance of perovskite photovoltaic devices. In addition to the interfacial structure, the optical properties, bulk structures, and surface morphologies of the PT layers were also studied. Interestingly, all PT derivatives with different side chain lengths showed identical UV-vis absorption spectra in the wavelength range of 350 nm-750 nm, demonstrating similar band structure of all PT derivatives. No signals could be detected from these PT layers using XRD and GIXRD, indicating that such PT materials have a dominant amorphous structure in bulk (or exhibit very low crystallinity).

Our SFG studies showed that the orientation of the PT thiophene backbone at the buried PT/perovskite interface depends on their alkyl side chain length. PCE measurements indicated that the performance of perovskite solar cells varies with PT side chain length. Therefore, we believe that the orientation of the PT thiophene backbone at the perovskite interface is correlated to perovskite solar cell performance. It was found that normally (standing up) and tangentially (lying down) thiophene backbone orientations lead to different J_{sc} values (up to two times) while keeping V_{oc} similar. V_{oc} of a solar cell is determined primarily by the bandgap energy difference, so similar V_{oc} values measured in this study further validate the similar band structures of different PTs. The J_{sc} values measured for more than two times difference between the longest and shortest polythiophene side chains (P3HT: 20.0 mA/cm^2; P3DDT: 9.3 mA/cm^2) indicate a strong correlation of the hole extraction efficiency and the PT backbone orientation at the HTL/perovskite interface. Our data indicated that a more normal orientation of HTL backbone at the HTL/perovskite interface is better for hole extraction efficiency.

We believe that this is the first study to correlate the buried interfacial structure in a perovskite solar cell to its performance. It was found that interfacial molecular orientation influences solar cell PCE. If the interfacial orientation of the thiophene backbone could be more perpendicular to the interface, the solar cell performance should be improved. We believe that, in the future, the rational design of the buried interface in solar cells will result in performance improvements. This research again demonstrates the power of SFG to probe buried interfaces. While for solar cell research, this study only studied the HTL/photoactive layer interface of perovskite solar cells, it is believed (and already demonstrated to some extent) that other interfaces (photoactive/ETL, donor/acceptor, etc.) in different photovoltaic materials and structures will also have a strong impact on charge carrier dynamics across the interface. We believe that it is feasible to apply SFG to probe such interfaces to understand the structural and functional relations of these interfaces and their impacts on the entire device. Such knowledge will have broader impacts on the research field of photovoltaics in the future.

3.4. Reference

(1) Kojima, A.; Teshima, K.; Shirai, Y.; Miyasaka, T. *Journal of the American Chemical Society* **2009**, *131*, 6050.

(2) Snaith, H. J. *The Journal of Physical Chemistry Letters* **2013**, *4*, 3623.

(3) Zhou, H.; Chen, Q.; Li, G.; Luo, S.; Song, T.-b.; Duan, H.-S.; Hong, Z.; You, J.; Liu, Y.; Yang, Y. *Science* **2014**, *345*, 542.

(4) Abrusci, A.; Stranks, S. D.; Docampo, P.; Yip, H.-L.; Jen, A. K.-Y.; Snaith, H. J. *Nano letters* **2013**, *13*, 3124.

(5) Conings, B.; Baeten, L.; De Dobbelaere, C.; D'Haen, J.; Manca, J.; Boyen, H. G. *Advanced Materials* **2014**, *26*, 2041.

(6) Meng, L.; You, J.; Guo, T.-F.; Yang, Y. *Accounts of chemical research* **2015**.

(7) Jeon, N. J.; Noh, J. H.; Kim, Y. C.; Yang, W. S.; Ryu, S.; Seok, S. I. *Nature materials* **2014**, *13*, 897.

(8) Guo, Y.; Liu, C.; Inoue, K.; Harano, K.; Tanaka, H.; Nakamura, E. *Journal of Materials Chemistry A* **2014**, *2*, 13827.

(9) Docampo, P.; Ball, J. M.; Darwich, M.; Eperon, G. E.; Snaith, H. J. *Nature communications* **2013**, *4*.

(10) Lee, M. M.; Teuscher, J.; Miyasaka, T.; Murakami, T. N.; Snaith, H. J. *Science* **2012**, *338*, 643.

(11) Liu, M.; Johnston, M. B.; Snaith, H. J. *Nature* **2013**, *501*, 395.

(12) Xing, Y.; Sun, C.; Yip, H.-L.; Bazan, G. C.; Huang, F.; Cao, Y. *Nano Energy* **2016**, *26*, 7.

(13) Bai, Y.; Chen, H.; Xiao, S.; Xue, Q.; Zhang, T.; Zhu, Z.; Li, Q.; Hu, C.; Yang, Y.; Hu, Z. *Advanced Functional Materials* **2016**, *26*, 2950.

(14) Liao, W.; Zhao, D.; Yu, Y.; Grice, C. R.; Wang, C.; Cimaroli, A. J.; Schulz, P.; Meng, W.; Zhu, K.; Xiong, R. G. *Advanced Materials* **2016**.

(15) Liao, W.; Zhao, D.; Yu, Y.; Shrestha, N.; Ghimire, K.; Grice, C. R.; Wang, C.; Xiao, Y.; Cimaroli, A.; Ellingson, R. J. *Journal of the American Chemical Society* **2016**.

(16) Kim, J.; Kim, G.; Kim, T. K.; Kwon, S.; Back, H.; Lee, J.; Lee, S. H.; Kang, H.; Lee, K. *Journal of Materials Chemistry A* **2014**, *2*, 17291.

(17) Hsiao, Y.-S.; Charan, S.; Wu, F.-Y.; Chien, F.-C.; Chu, C.-W.; Chen, P.; Chen, F.-C. *The Journal of Physical Chemistry C* **2012**, *116*, 20731.

(18) Huang, J.-H.; Yang, C.-Y.; Ho, Z.-Y.; Kekuda, D.; Wu, M.-C.; Chien, F.-C.; Chen, P.; Chu, C.-W.; Ho, K.-C. *Organic Electronics* **2009**, *10*, 27.

(19) Wu, J.-L.; Chen, F.-C.; Hsiao, Y.-S.; Chien, F.-C.; Chen, P.; Kuo, C.-H.; Huang, M. H.; Hsu, C.-S. *ACS nano* **2011**, *5*, 959.

(20) Ayzner, A. L.; Nordlund, D.; Kim, D.-H.; Bao, Z.; Toney, M. F. *The journal of physical chemistry letters* **2014**, *6*, 6.

(21) Rand, B. P.; Cheyns, D.; Vasseur, K.; Giebink, N. C.; Mothy, S.; Yi, Y.; Coropceanu, V.; Beljonne, D.; Cornil, J.; Brédas, J. L. *Advanced Functional Materials* **2012**, *22*, 2987.

(22) Shen, Y. *Nature* **1989**, *337*, 519.

(23) Winokur, M.; Spiegel, D.; Kim, Y.; Hotta, S.; Heeger, A. *Synthetic Metals* **1989**, *28*, 419.

(24) Vanlaeke, P.; Swinnen, A.; Haeldermans, I.; Vanhoyland, G.; Aernouts, T.; Cheyns, D.; Deibel, C.; D'Haen, J.; Heremans, P.; Poortmans, J. *Solar energy materials and solar cells* **2006**, *90*, 2150.

(25) Anglin, T. C.; Lane, A. P.; Massari, A. M. *Journal of Materials Chemistry C* **2014**, *2*, 3390.

(26) Perepichka, I. F.; Perepichka, D. F. *Handbook of thiophene-based materials: applications in organic electronics and photonics*; Wiley Online Library, 2009; Vol. 2.

(27) Erb, T.; Zhokhavets, U.; Gobsch, G.; Raleva, S.; Stühn, B.; Schilinsky, P.; Waldauf, C.; Brabec, C. J. *Advanced Functional Materials* **2005**, *15*, 1193.

(28) Ma, W.; Yang, C.; Gong, X.; Lee, K.; Heeger, A. J. *Advanced Functional Materials* **2005**, *15*, 1617.

(29) Brinkmann, M.; Rannou, P. *Advanced Functional Materials* **2007**, *17*, 101.

(30) Do Hwan Kim, Y. D. P.; Jang, Y.; Yang, H.; Kim, Y. H.; Han, J. I.; Moon, D. G.; Park, S.; Chang, T.; Chang, C.; Joo, M. *Adv. Funct. Mater* **2005**, *15*, 77.

(31) Dudenko, D.; Kiersnowski, A.; Shu, J.; Pisula, W.; Sebastiani, D.; Spiess, H. W.; Hansen, M. R. *Angewandte Chemie International Edition* **2012**, *51*, 11068.

(32) Xiao, M.; Zhang, X.; Bryan, Z. J.; Jasensky, J.; McNeil, A. J.; Chen, Z. *Langmuir* **2015**, *31*, 5050.

(33) Yamamoto, K.; Ochiai, S.; Wang, X.; Uchida, Y.; Kojima, K.; Ohashi, A.; Mizutani, T. *Thin Solid Films* **2008**, *516*, 2695.

(34) Lee, K. H.; Schwenn, P. E.; Smith, A. R.; Cavaye, H.; Shaw, P. E.; James, M.; Krueger, K. B.; Gentle, I. R.; Meredith, P.; Burn, P. L. *Advanced Materials* **2011**, *23*, 766.

(35) Yun, J.-J.; Peet, J.; Cho, N.-S.; Bazan, G. C.; Lee, S. J.; Moskovits, M. *Applied Physics Letters* **2008**, *92*, 251912.

(36) Anglin, T. C.; Speros, J. C.; Massari, A. M. *The Journal of Physical Chemistry C* **2011**, *115*, 16027.

(37) Gao, Y.; Grey, J. K. *Journal of the American Chemical Society* **2009**, *131*, 9654.

(38) Xiao, M.; Joglekar, S.; Zhang, X.; Jasensky, J.; Ma, J.; Cui, Q.; Guo, L. J.; Chen, Z. *Journal of the American Chemical Society* **2017**, *139*, 3378.

(39) Prajongtat, P.; Wargulski, D. R.; Unold, T.; Dittrich, T. *The Journal of Physical Chemistry C* **2016**, *120*, 3876.

(40) Wong, F.; Perez, G.; Bonilla, M.; Colon-Santana, J. A.; Zhang, X.; Sharma, P.; Gruverman, A.; Dowben, P. A.; Rosa, L. G. *RSC Advances* **2014**, *4*, 3020.

(41) Li, Z.; Gao, F.; Greenham, N. C.; McNeill, C. R. *Advanced Functional Materials* **2011**, *21*, 1419.

(42) Li, Z.; Lakhwani, G.; Greenham, N. C.; McNeill, C. R. *Journal of Applied Physics* **2013**, *114*, 034502.

(43) McNeill, C. R.; Hwang, I.; Greenham, N. C. *Journal of applied physics* **2009**, *106*, 024507.

(44) Xiao, Z.; Dong, Q.; Bi, C.; Shao, Y.; Yuan, Y.; Huang, J. *Advanced Materials* **2014**, *26*, 6503.

CHAPTER 4 Interfacial Molecular Structure And Adhesion

Materials covered in this chapter were submitted for publication. This research was collaborated with Dr. Carol Mohler, Dr. Christopher Tucker and Dr. Brian Walther at Dow Chemical. They provided samples and helped for data interpretation.

4.1. Background and Motivation

Polyolefins are used in a broad range of applications, from components in high performance footwear to multilayer thin films in food packaging.[1-5] Yet the non-polar nature of the polyolefin surface can create challenges in achieving sufficient adhesion to more polar surfaces such as metals, paints, primers and inks. For example, in multilayer food packaging applications, polyolefins must adhere to dissimilar barrier materials such as poly (ethylene terephthalate) (PET), ethylene vinyl alcohol (EVOH), nylon or metal. Furthermore, polymer processing can influence interlayer adhesion, where resins produced by blown films can exhibit different adhesive properties than those prepared by cast extrusion.

To address these adhesion challenges, one approach has been to use functional polymers such as maleic anhydride (MAH)-grafted polyolefins as adhesion promoters or "tie layers", designed to promote adhesion between the polyolefin and the polar surface through hydrogen bonding, polar-polar interactions or covalent bonding.[6-9] However the specific mechanism of adhesion at the interfaces is not well understood, whether between the polyolefin and the tie-layer,

or the tie-layer and the polar surface. In collaboration with Dow Corning and Dow Chemical, we wish to to build a fundamental understanding of the interfacial molecular structure of polyolefins such as polyethylene, the effect of grafting polar substances such as MAH into the polymer backbone and relate that to the adhesive properties.

Quantitative measurements of the adhesion strength to various polymers are relatively straightforward, but understanding interfacial failure mechanisms of polymer materials is usually more challenging. Numerous experimental approaches have been used to study polymer interfaces post-failure. For example, scanning electron microscopy and atomic force microscopy techniques are useful in determining the physical morphology of a failed interface, while methods such as X-ray photoelectron spectroscopy can give information on elemental composition on both interfaces after adhesive failure.[10-12] One important assumption in these approaches is that the failed interface (with two exposed surfaces) and the original buried interface are identical. However, this assumption may not be true because the interfacial failure could lead to the structural changes of the original buried interface, which is highly likely. Therefore, to understand the true origins of interfacial failure, it is necessary to examine the structure of the original buried interface in-situ.

In recent years, we have used a nonlinear optical method, sum frequency generation vibrational spectroscopy (SFG), to study molecular structures at solid-solid interfaces, including "buried" polymer-polymer or polymer-metal interfaces.[13-27] SFG is capable of detecting molecular species at interfaces or in bonded parts, without the need to debond the article. In this research, SFG is applied to investigate the interfacial molecular structure of a linear low density polyethylene (LLDPE) and a maleic anhydride (MAH) grafted linear low density polyethylene in-situ. The adhesion strength of both polymers to silica and nylon was also determined. The molecular structures of the polymers at the interface obtained from SFG studies are correlated to

the adhesion strength, providing insight into the relationship between the chemical groups at the interface, their orientation and their effect on adhesive properties.[15,18,19,23,28-31]

4.2. Structure and Adhesion Property of Polyethylene at Different Interfaces

4.2.1. Materials and Sample Preparation

Two LLDPE samples were studied in this research. One LLDPE (EO) is an ethylene-octene copolymer with a density of 0.87 g/mL, 1.0 melt index (2.16kg at 190^{o}C). The other sample (EOgMAH) is an ethylene-octene copolymer with a maleic anhydride graft level of 1.1% by weight (0.870 g/mL density, 3.0 melt index (2.16kg at 190^{o}C)). They were provided in pellet form from Dow Chemical. The Ultramid™ C33 nylon (white pellets, BASF) is a blend of Nylon 6 and Nylon 66. All materials were used as received.

For the SFG experiments, a silica prism was brought to temperature 165°C for EO (or 185°C for EOgMAH). The pellet (EO or EOgMAH) was placed on the prism and heated for 10 minutes until it softened and then was firmly pressed against the prism to ensure good physical contact between the PE and silica. The sample was then cooled to ambient temperature (22 ^{o}C) for the SFG experiment. The PE/nylon samples were prepared in a similar fashion on silica prisms previously coated with nylon. The Nylon coating was prepared via spin-coating an Ultramid™ C33 solution (5 mg/mL in m-Cresol) at 2000 rpm for 60 seconds on a prism substrate. Samples for adhesion testing were prepared in a similar fashion as described above, except that a silica window was used as a substrate instead of a silica prism.

4.2.2. SFG Measurements and Data Analysis

SFG theory, SFG experimental details, and the SFG equipment used in this study have been presented in chapter 1 and published previously.[21,22,27,32-60] Figure 4-1 shows the SFG experimental

geometry used in this study to collect SFG spectra from the PE/silica interface or the PE/polymer interface.

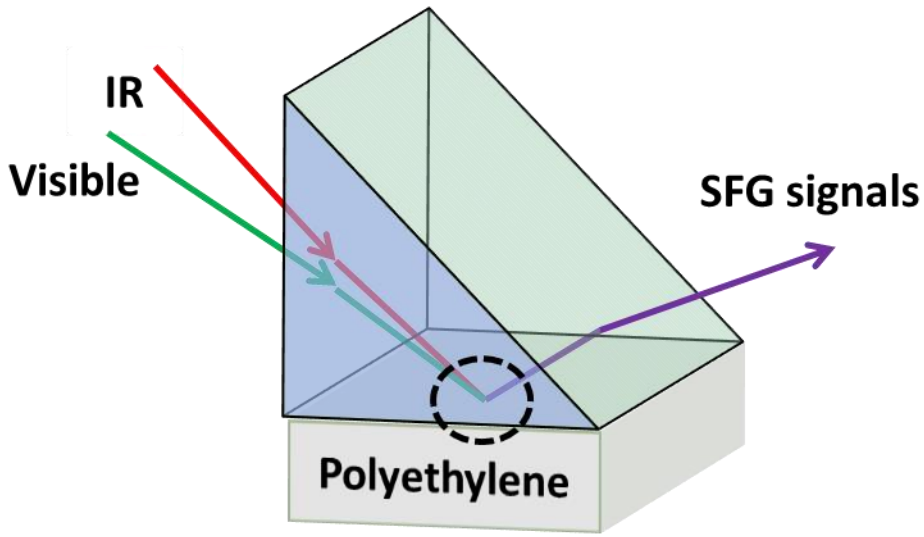

Figure 4-1. Diagram of sample geometry for SFG experiments. The buried interface being investigated is indicated by the dashed circle, and represents the interface either between the silica prism and polyethylene or between nylon and polyethylene.

We discussed the SFG orientation analysis methodology in chapter 1. The chemical groups of interest in this study are the methylene groups in the backbone of the polyethylene polymer, which have C_{2v} symmetry. In this case we have:[61]

$$\chi^{(2)}_{yyz,ss} = \frac{N_s}{2}\left(\beta_{aac,ss}\cos^2\phi + \beta_{bbc,ss}\sin^2\phi + \beta_{ccc,ss}\right)\cos\theta + \frac{N_s}{2}\left(\beta_{aac,ss}\sin^2\phi + \beta_{bbc,ss}\cos^2\phi - \beta_{ccc,ss}\right)\cos^3\theta \quad (4\text{-}1)$$

$$\chi^{(2)}_{zzz,ss} = N_s\left(\beta_{aac,ss}\sin^2\phi + \beta_{bbc,ss}\cos^2\phi\right)\cos\theta - N_s\left(\beta_{aac,ss}\sin^2\phi + \beta_{bbc,ss}\cos^2\phi - \beta_{ccc,ss}\right)\cos^3\theta \quad (4\text{-}2)$$

$$\chi^{(2)}_{yyz,as} = -N_s\beta_{aca,as}\sin^2\phi\left(\cos\theta - \cos^3\theta\right) \quad (4\text{-}3)$$

$$\chi^{(2)}_{zzz,as} = 2N_s\beta_{aca,as}\sin^2\phi\left(\cos\theta - \cos^3\theta\right) \quad (4\text{-}4)$$

where θ and ϕ are the tilt and twist angles, respectively, of a methylene group at an interface (Figure 4-2) necessary to deduce the orientation of a methylene group at an interface. The calculated $\chi_{yyz,ss}/\chi_{zzz,ss}$ ratio as a function of methylene orientation (defined by the tilt and twist angles) is shown in Figure 4-2. The $\chi_{yyz,ss}/\chi_{zzz,ss}$ ratio can also be measured experimentally. By comparing the experimentally obtained ratio to the generated $\chi_{yyz,\ ss}/\chi_{zzz,\ ss}$ ratio map shown in Figure 4-2b, the twist and tilt angles which match the experimental data can be determined. The same analysis can be performed on an independently measured $\chi_{yyz,ss}/\chi_{yyz,as}$ ratio (Figure 4-2c) to infer the matching orientation angles for the $\chi_{yyz,ss}/\chi_{yyz,as}$ ratio measurement. The overlapped regions obtained from the two independent measurements satisfy both independent measurements, which provide more accurately measured orientation angle regions compared to those obtained by only one measurement. More details about this method can be found in previous publications.[62,63]

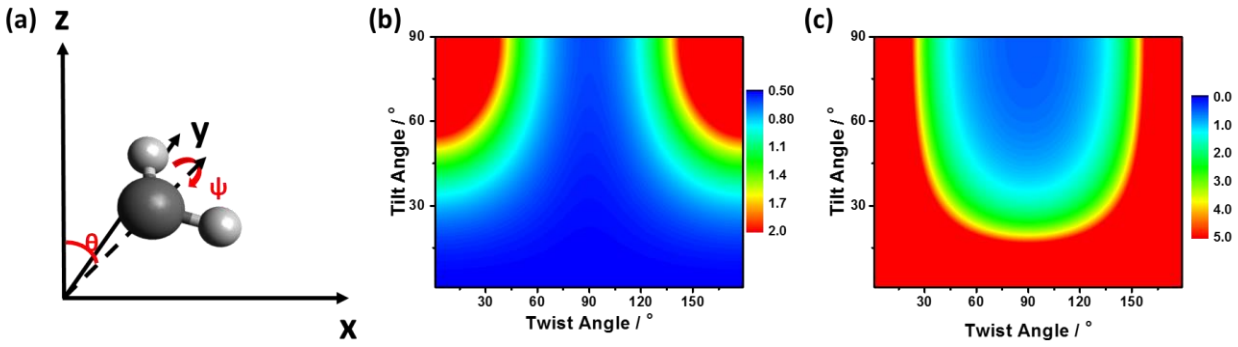

Figure 4-2. (a) Defined tilt angle θ and twist angle ψ of a methylene CH_2 group; Calculated values of (b) $\chi_{yyz,ss}/\chi_{zzz,ss}$ ratio of methylene symmetric C-H stretching vibration mode and (c) $\chi_{yyz,ss}/\chi_{yyz,as}$ ratio of methylene group plotted as functions of tilt angle θ and twist angle ψ. The tilt angle is zero when the principal axis of the CH_2 group is perpendicular to the surface (xy plane). The twist angle

zero is defined as following: When the tilt angle is 90°, the two C-H bonds are lying down on the xy plane surface.

4.2.3. Structure of Polyethylene at Different Interfaces

CH Stretching Region

Figures 4-3a and 4-3d show the SFG spectra collected from the EO/silica interface and the EOgMAH/silica interface, respectively. SFG spectra collected from the EO/silica interface could be fitted using three peaks at 2852 cm^{-1}, 2900 cm^{-1} and 2928 cm^{-1}, which are contributed by the methylene symmetric C-H stretch, methylene Fermi resonance, and methylene asymmetric C-H stretch, respectively,[64] indicating that the EO/silica interface is dominated by the methylene groups of the PE backbone. The SFG spectra collected from the EOgMAH/silica interface are more complicated, which could be fitted using five peaks. Apart from the 2852 cm^{-1}, 2900 cm^{-1} and 2928 cm^{-1} peaks contributed from the methylene -CH_2 backbone, two methyl C-H stretching peaks at 2877 cm^{-1} (CH_3 symmetric stretching) and 2945 cm^{-1} (-CH_3 Fermi resonance) were also needed to fit the spectra. These bands may support the existence of methyl containing additives in the grafted polymer that migrate to the interface, and are not present (or do not migrate to the interface) in the ungrafted polymer. In addition to the presence of the methyl groups, these additional bands may however also arise from differences in crystallinity between the higher molecular weight (higher melt index) grafted polymer compared to its ungrafted counterpart. It is known that high molecular weight polyethylene polymers can form ordered films with higher crystallinity, which is reflected in narrower bands in their SFG spectrum.[65] The additional bands observed in the SFG of grafted polyethylene (Figure 4-3a, d) also appear to be narrower than those observed in the ungrafted polymer. The distinctive chain folding feature of the polymer observed in crystalline polyethylene

films results in a high density of *gauche* conformers at the surface folds, which causes a blue-shift and narrowing of the spectral features.

Additional information can be obtained about the orientation of these molecules at the interface, by varying the polarization of the input beams. All the spectral fitting parameters are listed in the Table 4-1 for the *ssp* and *ppp* spectra collected from the EO/silica interface. The $\chi_{yyz,ss}/\chi_{zzz,ss}$ and $\chi_{yyz,ss}/\chi_{yyz,as}$ ratios (0.81 and 2.8) can be obtained from the spectral fitting results. Comparing each measured ratio to the calculated orientation dependent ratio map shown in Figure 4-2 deduces the most likely orientation angle ranges. These two measured ratios are obtained from independent measurements, and correspond to different orientation angle regions. The finally deduced orientation angles should satisfy both ratios, which should be in the overlapped orientation angle regions deduced from these two orientation angle regions. Figure 4-3b shows the deduced orientation angle regions of the methylene groups at the EO/silica interface from the methylene symmetric C-H stretch $\chi_{yyz,ss}/\chi_{zzz,ss}$ ratio. Figure 4-3c displays such regions obtained from the methylene C-H symmetric and asymmetric stretch $\chi_{yyz,ss}/\chi_{yyz,as}$ ratio in the *ssp* spectra. Figure 4-4a shows the overlapped regions of the possible regions in Figures 3b and 3c, given a 20% error. The error analysis for this approach was published in detail previously.[62] Similarly, SFG spectra collected from the EOgMAH/silica interface shown in Figure 4-3d can be fitted (fitting parameters can be found Table 4-1). Figures 4-3e and 4-3f displayed the possible orientation angle regions, while Figure 4-4b represents the overlapped orientation angle regions shown in Figures 4-3e and 4-3f (showing the methylene orientations at the EOgMAH/silica interface). Figure 4-4a and b indicate that methylene groups adopt an orientation parallel to the silica interface (lying down in the plane of the interface) regardless of MAH-grafting, however the most probable tilt angle of the methylene groups at the EO/silica interface is slightly larger than that of the grafted

EOgMAH/silica interface (85° vs 75° relative to the surface normal). The most likely methylene twist angles at the two polymer/silica interfaces were slightly different as well: 65° or 115° at the EO/silica interface, and 50° or 130° at the EOgMAH/silica interface. ($\chi_{yyz,ss}/\chi_{zzz,ss}$ and $\chi_{yyz,ss}/\chi_{yyz,as}$ ratios 0.63 and 2.0)

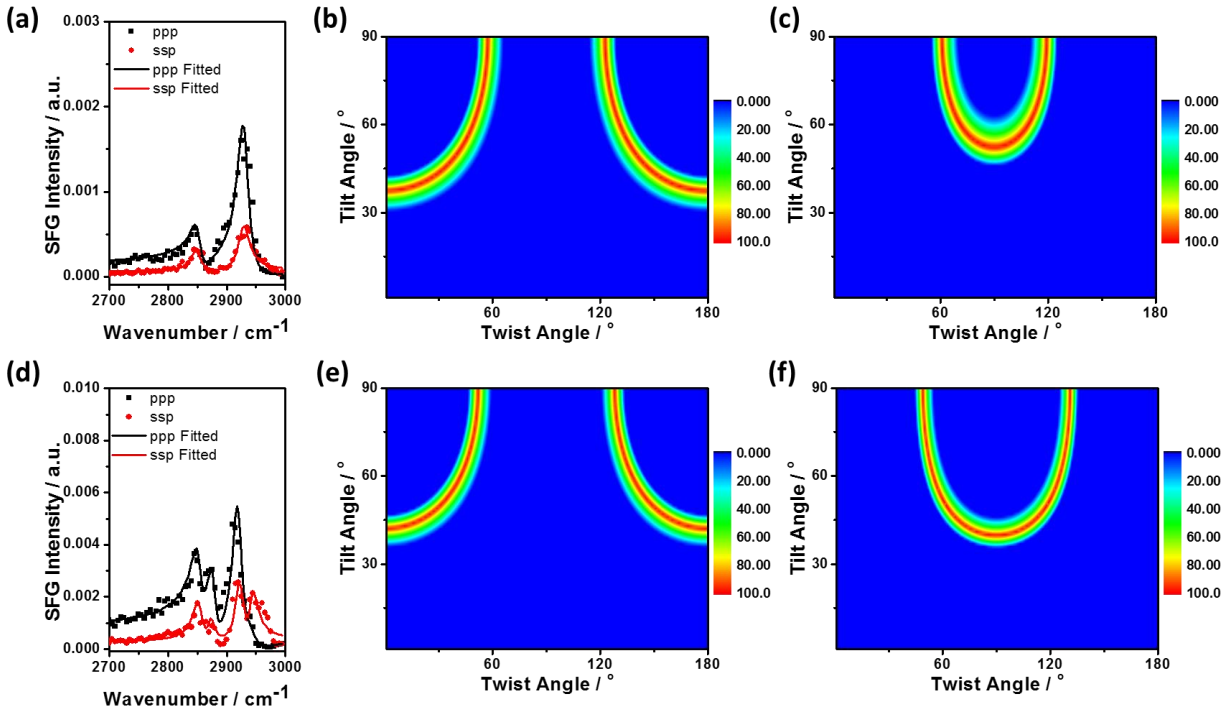

Figure 4-3 (a) SFG spectra collected from the EO/silica interface; Possible methylene orientation at the EO/silica interface deduced from methylene $\chi_{yyz,ss}/\chi_{zzz,ss}$ (b) and from $\chi_{yyz,ss}/\chi_{yyz,as}$ (c); (d) SFG spectra collected from the EOgMAH/silica interface; Possible methylene orientation at the EOgMAH/silica interface deduced from methylene $\chi_{yyz,ss}/\chi_{zzz,ss}$ (e) and from $\chi_{yyz,ss}/\chi_{yyz,as}$ (f).

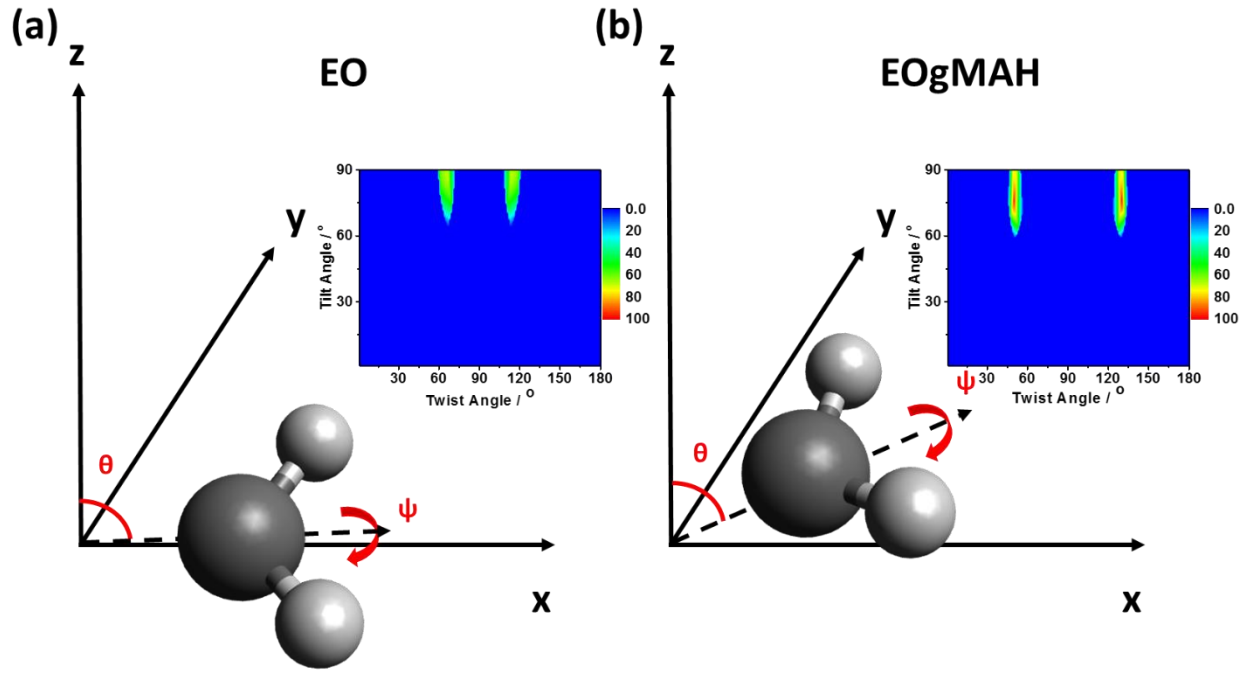

Figure 4-4 (a) Most probable orientation of the methylene groups at the EO/silica interface (determined from overlap on Figure 4-3b & c, and a schematic showing the methylene orientation; (b) Deduced most possible methylene orientation at the EOgMAH/silica interface by overlapping 3e and 3f, and the schematic showing the methylene orientation.

ppp fitting details		ssp fitting details	
Amplitude 1	0.138	Amplitude 1	0.165
Wave number	2852	Wave number	2848
Width	10	Width	10
Amplitude 2	0.4832	Amplitude 2	-0.28
Wave number 2	2928	Wave number 2	2928
Width 2	12	Width	12

Table 4-1 Fitting parameters for Fig 4-3a

ppp fitting details	ssp fitting details

Amplitude 1	0.28	Amplitude 1	0.39
Wavenumber 1	2852	Wavenumber 1	2853
Width 1	10	Width 1	10.7
Amplitude 2	0.3	Amplitude 2	0.16
Wavenumber 2	2877	Wavenumber 2	2872
Width 2	9.1	Width 2	7
Amplitude 3	0.65	Amplitude 3	-0.4
Wavenumber 3	2920	Wavenumber 3	2922
Width 3	10.1	Width 3	9.2
Amplitude 4	0.13	Amplitude 4	-0.25
Wavenumber 4	2940	Wavenumber 4	2943
Width 4	9.9	Width 4	8.3

Table 4-2 Fitting parameters for Fig 4-3d

The molecular composition and orientation of molecular groups at the interface of polyethylene and more polar substrates such as nylon, is also of interest. However, SFG measurements of PE/nylon interfaces are more complex to analyze since nylon may also contribute to the C-H stretching signals, overlapping with signals generated from PE itself.

To ensure that SFG signals from nylon can be distinguished from that of PE at the PE/nylon interface, the nylon/air interface alone was first studied. Figure 4-5a shows the SFG *ssp* and *ppp* spectra collected from the nylon/air interface. The 2850 cm^{-1} peak is assigned as the methylene C-H symmetric stretch, the 2930 cm^{-1} peak the methylene Fermi resonance, and the 2955 cm^{-1} signal is the asymmetric C-H stretch of methylene. According to the spectral fitting results, $\chi_{yyz,ss}/\chi_{zzz,ss}$ and $\chi_{yyz,ss}/\chi_{yyz,as}$ ratios (0.81 and 2.8) can be deduced. From such ratios, the most likely orientation angle regions of methylene groups on nylon in air can be determined using the methodology

presented above, as shown in Figure 4-5b. Figure 4-5b shows that the most likely methylene tilt angle at the nylon/air interface is around 40°, and the twist angle is around 40° or 140°, significantly different from the orientation angles at the PE/silica interface. The methylene groups of polyethylene appear to stand up more and are more twisted at the nylon surface than at the silica interface. The interactions between the methylene groups in the polyethylene and other functionalities in nylon near the surface (even if not at the surface) influence the methylene orientation in nylon on the surface.

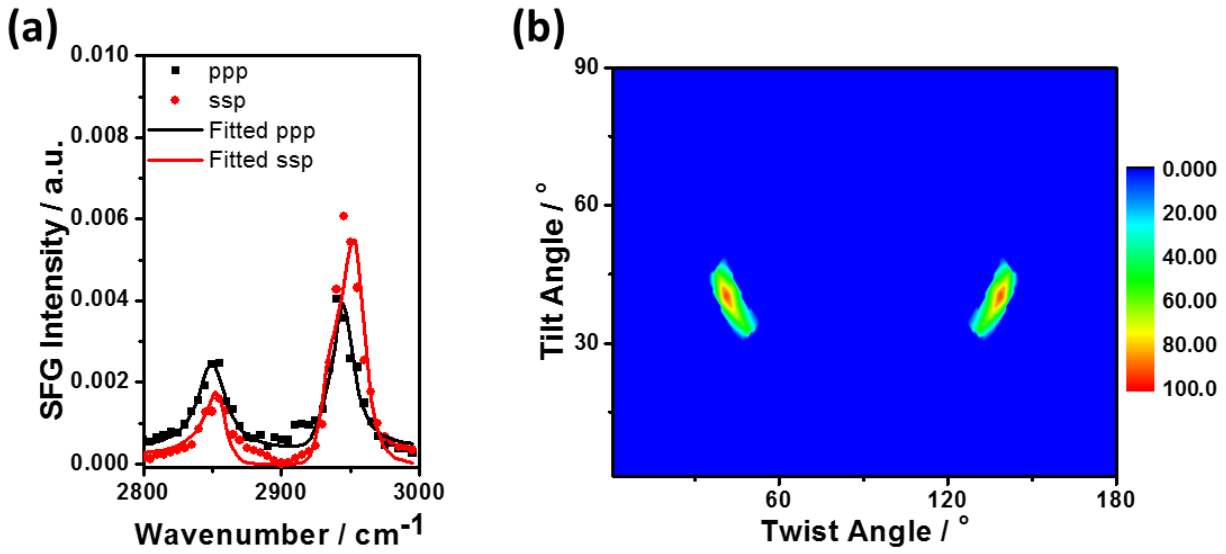

Figure 4-5 (a) SFG spectra collected from the nylon/air interface; (b) deduced most likely orientation of methylene at the nylon/air interface.

ppp fitting details		ssp fitting details	
Amplitude 1	0.554	Amplitude 1	0.34
Wavenumber 1	2850	Wavenumber 1	2855
Width 1	12	Width 1	8.8

Amplitude 2	0.3	Amplitude 2	-0.4
Wavenumber 2	2925	Wavenumber 2	2930
Width 2	10	Width 2	10
Amplitude 3	0.59	Amplitude 3	0.75
Wavenumber 3	2945	Wavenumber 3	2955
Width 3	9.03	Width 3	10

Table 4-3 Fitting parameters for Fig 4-5

Since SFG spectra collected from the PE/nylon interface contain contributions from both PE and nylon, it is challenging to obtain the PE contribution directly. To simplify the analysis, the surface structure of nylon in air is assumed to be similar to that at the PE interface. This assumption enables the nylon contribution to the spectra to be extracted. It is noted that this assumption may not be completely accurate, because the interactions at the air surface and PE interface can be different. However it is critical to separate the signals from the methylene groups in PE from those in nylon at the nylon/PE interface and this provides a useful first approximation.

Figure 4-6a shows the SFG spectra collected from the EO/nylon interface. Using the nylon signal contribution deduced from the nylon/air interface, the PE signal contribution at the PE/nylon interface from the total spectra could be deduced, as shown in Figure 4-6b and Figure 4-6c. Using such signal contributions, we could deduce the $\chi_{yyz,ss}/\chi_{zzz,ss}$ and $\chi_{yyz,ss}/\chi_{yyz,as}$ ratios (0.81 and 1.3). It is important to note that, the SFG signals from methylene groups of nylon and of EO at the EO/nylon interface have opposite phases; this is determined by comparing the signal contribution from the nylon and the total spectra collected from the PE/nylon interface. This interesting feature arises since the experimentally observed methylene CH_2 symmetric stretch signal at 2850 cm^{-1} from the EO/nylon interface is impossible to fit if the signals from the PE and nylon methylene

groups interfere constructively. Figure 4-7a and 7b show the possible orientation angle regions deduced by the $\chi_{yyz,ss}/\chi_{zzz,ss}$ and $\chi_{yyz,ss}/\chi_{yyz,as}$ ratios respectively. Figure 4-7c displays the overlapped region from the regions shown in Figure 4-7a and 7b, which is the finally deduced orientation angle region for PE methylene groups at the EO/nylon interface. A schematic of the above methylene orientation is shown in Figure 4-7d. Here the spectra are mainly contributed by methylene groups, indicating that the interface is dominated by methylene groups.

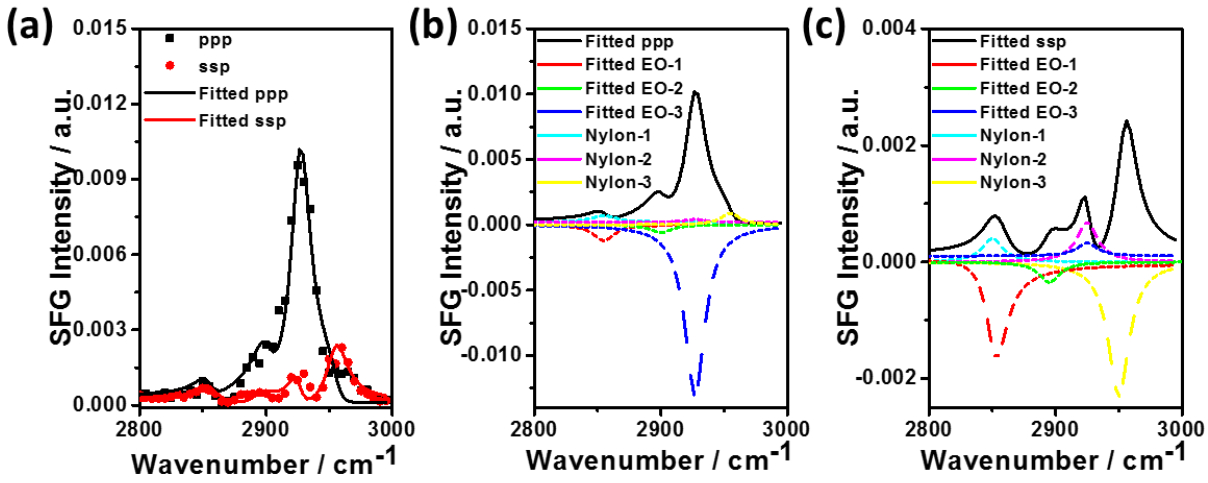

Figure 4-6 (a) SFG spectra collected from the EO/nylon interface; (b) The deduced SFG *ppp* signal contribution from EO at the EO/nylon interface; (c) The deduced SFG *ssp* signal contribution from EO at the EO/nylon interface. The black lines show the fitted total spectra. Other fitted peaks (broken lines) are from EO and Nylon.

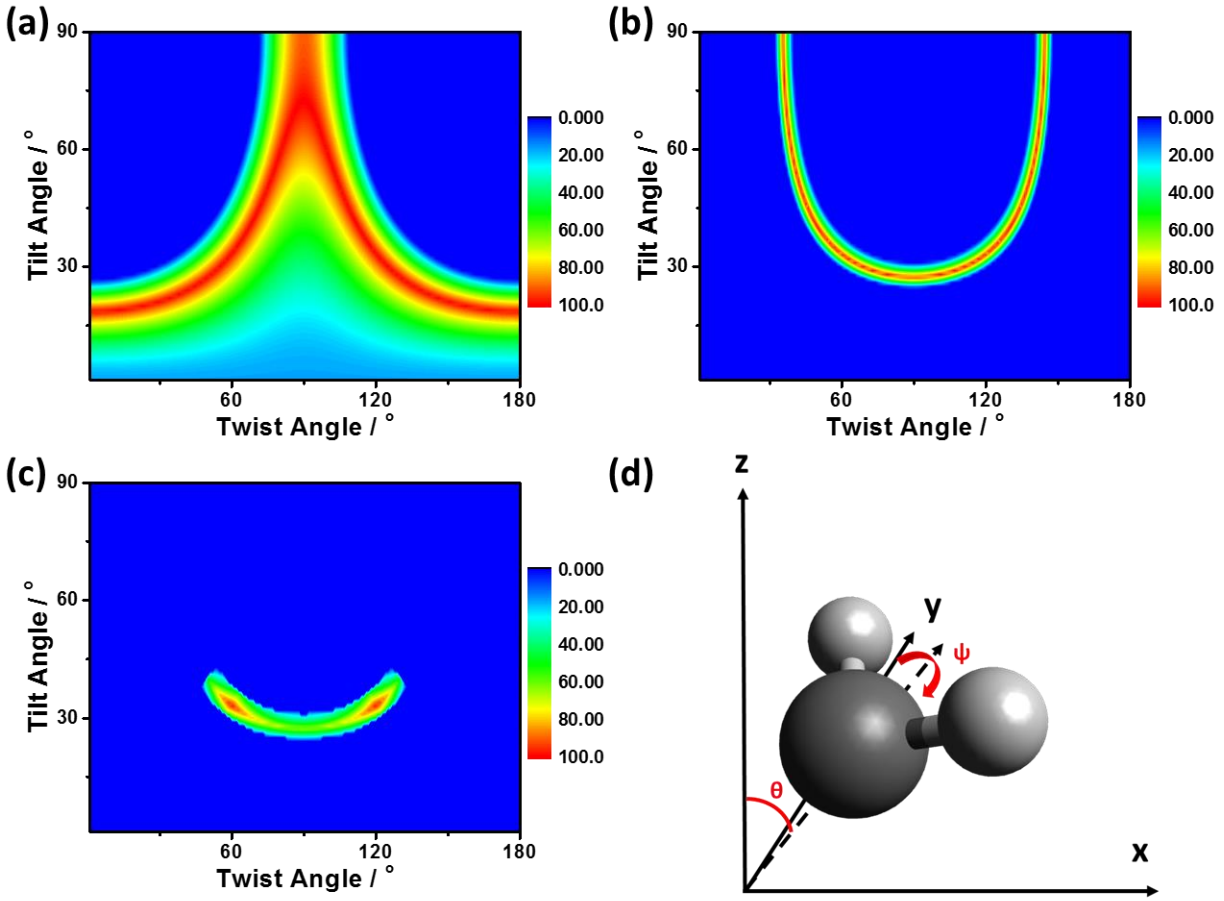

Figure 4-7 The deduced orientation angle ranges of methylene groups at the EO/nylon interface from the $\chi_{yyz,ss}/\chi_{zzz,ss}$ ratio (a) and the $\chi_{yyz,ss}/\chi_{yyz,as}$ ratio (b); (c) The overlapped region from those in Figure 4-7a and Figure 4-7b; (d) A schematic of the methylene orientation at the EO/nylon interface and the deduced orientation angle region from SFG (results from Figure 4-7c).

ppp fitting details		ssp fitting details	
Amplitude 1	-0.35	Amplitude 1	-0.5
Wavenumber 1	2855	Wavenumber 1	2855
Width 1	10	Width 1	10

Amplitude 2	-0.25	Amplitude 2	-0.1872
Wavenumber 2	2900	Wavenumber 2	2895
Width 2	10.2	Width 2	10
Amplitude 3	-1.1	Amplitude 3	0.35
Wavenumber 3	2927	Wavenumber 3	2925
Width 3	9.63	Width 3	7

Table 4-4 Fitting parameters for Fig 4-6a

Figure 4-8a shows the *ssp* SFG spectrum collected from the EOgMAH/nylon interface. Using a similar approach to that described above, we determined the SFG signal contribution from EOgMAH methylene groups at the interface by deducting the signal contribution from nylon at the EOgMAH/nylon interface (again by assuming the same nylon structure at the nylon/air interface and EOgMAH/nylon interface). Figure 4-8a shows the SFG *ssp* spectrum from the EOgMAH/nylon interface did not exhibit methylene symmetric stretch signal at 2850 cm^{-1}, in contrast to the observations for EO at the nylon interface. Such experimental data indicated that the signals from the methylene symmetric stretching at 2850 cm^{-1} from nylon and from EOgMAH were perfectly cancelled. Detailed fitting parameters of the SFG *ssp* spectrum collected from the EOgMAH/nylon interface can be found in Table 4-5. This shows that the tilt angles from the methylene groups of EOgMAH and nylon have opposite absolute orientations. Therefore, the disappearance of the methylene symmetric stretch signal provided the tilt angle information of methylene groups from EOgMAH at the interface. Instead of using both $\chi_{yyz,ss}/\chi_{zzz,ss}$ and $\chi_{yyz,ss}/\chi_{yyz,as}$ ratios to obtain the most likely methylene group orientation angle regions for EOgMAH at the EOgMAH/nylon interface, here we can use the tilt angle of the methylene groups and the measured $\chi_{yyz,ss}/\chi_{yyz,as}$ ratio (0.6 and 2.0) to deduce the EOgMAH methylene orientation. It is noted that SFG

spectra collected from the EOgMAH/nylon interface appear to contain the methyl contribution, showing that the interface has methyl groups as well, or contributions from gauche conformers as described earlier.

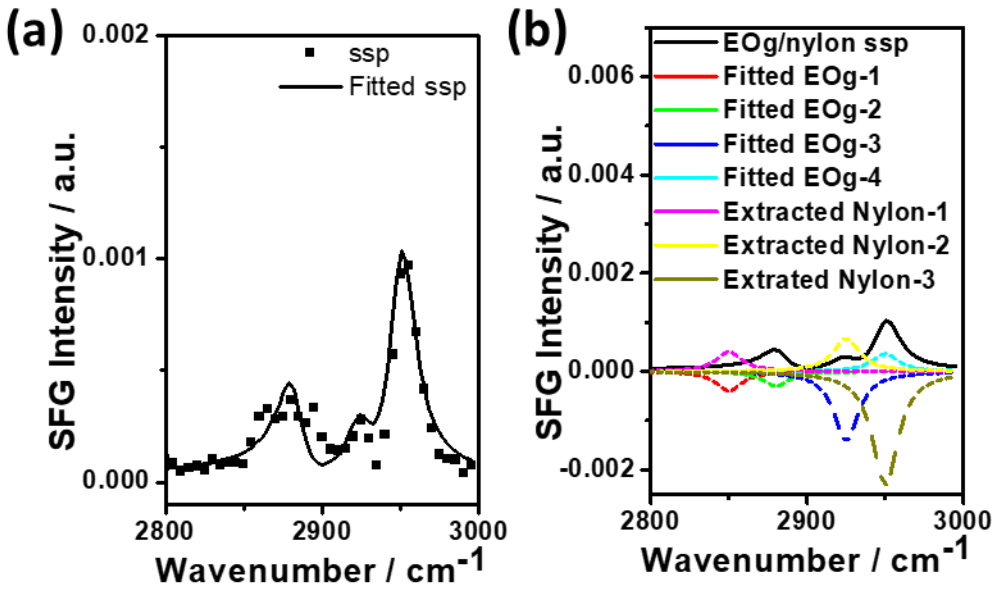

Figure 4-8 (a) SFG *ssp* spectrum collected from the EOgMAH/nylon interface; (b) the deduced SFG signal contribution from EOgMAH at the EOgMAH/nylon interface. The black lines show the fitted total spectra. Other fitted peaks (broken lines) are from EOgMAH and Nylon. (EOg in figure is abbreviation for EOgMAH)

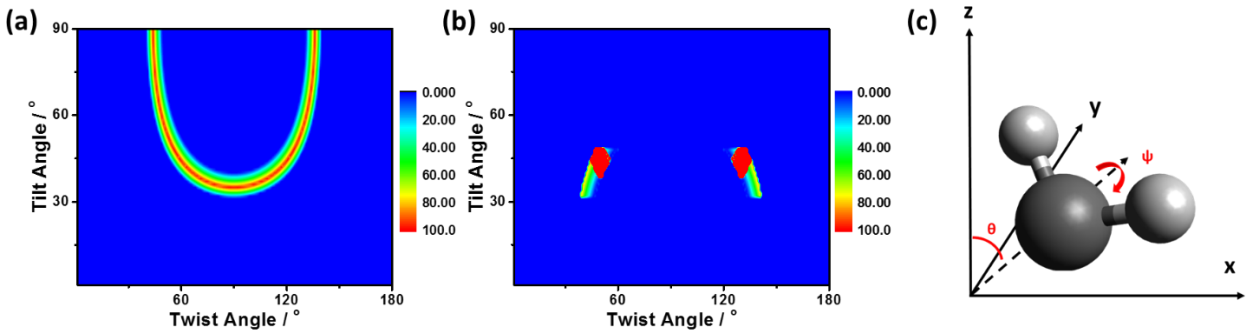

Figure 4-9 (a) The deduced orientation angle region of EOgMAH methylene groups from the $\chi_{yyz,ss}/\chi_{yyz,as}$ ratio; (b) The overlapped region from those in Figure 4-9a and Figure 5b; (c)A schematic of the methylene orientation at the EOgMAH/nylon interface

ssp fitting details	
Amplitude 1	-0.17
Wavenumber 1	2880
Width 1	10
Amplitude 2	-0.55
Wavenumber 2	2925
Width 2	9.58
Amplitude 3	-0.26
Wavenumber 3	2950
Width 3	9.8

Table 4-5 Fitting parameters for Fig 4-7a

The methylene structures of both EO and EOgMAH at the buried PE/nylon interfaces can therefore be compared. The results indicate that methylene groups in both grafted and ungrafted polyethylene stand up more towards the surface normal at nylon interfaces, compared to those at

silica interfaces. EO methylene showed a slightly smaller tilt angle compared to EOgMAH, and the most likely twist angles of the two were determined to be 45° for EO and 55° for EOgMAH (Figure 4-9). Methylene groups in these materials adopt different configurations at a silica versus a nylon interface, and show different behavior with grafting.

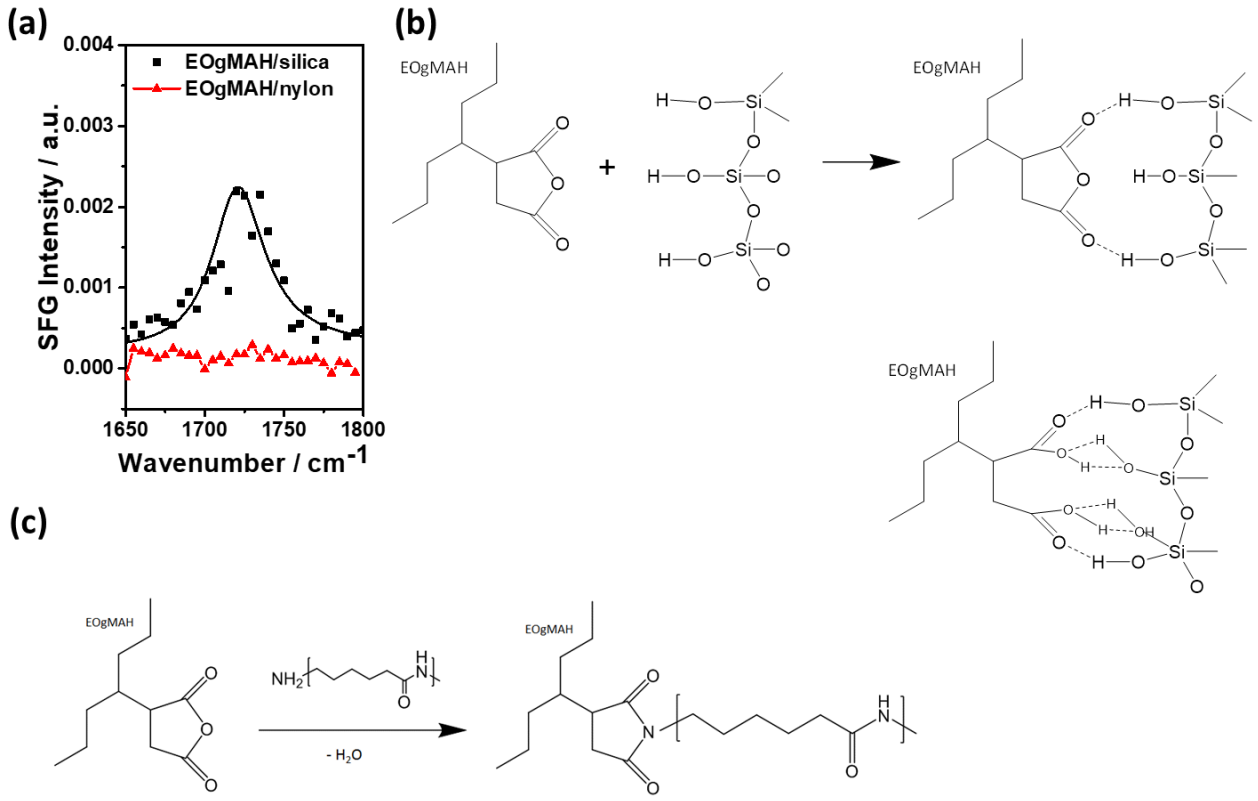

Figure 4-10 (a) SFG spectra of the MAH C=O functional groups at the EOgMAH/silica and EOgMAH/nylon interfaces; proposed reaction of maleic anhydride groups in EOgMAH with (b) silica surface, (c) nylon surface.

C=O Stretching Region

In addition to the SFG spectra collected from the interfaces in the C-H stretching frequency regions, we also studied SFG C=O stretching frequency regions to probe the interfacial MAH structure (Figure 4-10a). Since EO does not contain any MAH groups, no SFG signal was detected

in the C=O stretching region whether at silica or nylon interface (not shown). In contrast an SFG C=O stretching signal was observed at the EOgMAH/silica interface at ~1725 cm^{-1}, in agreement with other studies of grafted MAH polyolefins,[66,67] and indicates the C=O groups are ordered at the silica interface.

Silica particles are reported to bond to maleic anhydride grafted polypropylene, [68,69] preventing both agglomeration of silica particles in composites and facilitating break up of existing silica aggregates. Bonding is proposed to occur by reaction of the nucleophilic free surface hydroxyl groups with the maleic anhydride, or by hydrogen bonding between free surface hydroxyls and the carbonyl groups in the grafting group (Figure 4-10b). These interactions would be expected to create an ordered molecular interface at the silica/EOgMAH interface, since the carbonyl groups are uniformly directed to the silica surface and their orientation perpendicular to the surface held in place by bonds.

However a C=O signal was not detected at the nylon/EOgMAH interface. This indicates the C=O groups are either disordered or not present at the nylon/EOgMAH interface. Since grafting maleic anhydride to polyolefins such as polyethylene or polypropylene is well-known to increase their adhesion to polar substrates such as nylon, it more likely that carbonyl groups are present at the EOgMAH/nylon interface but that their orientation is random. The reaction of grafted maleic anhydride groups with a typical polyamine (Nylon 66) is shown in Figure 4-10c, where the anhydride ring opens, and an imide ring is formed with release of water. This reaction bonds the EOgMAH polymer to the nylon surface, at periodic points on the nylon polymer chain. Since bonding occurs through only one point on the anhydride (compared to two or more interactions with silanol groups above), there is more flexibility in the orientation and configuration of the imide group with respect to the surface. Furthermore, the orientation of amine

(and carbonyl) groups on the nylon surface is affected by the crystal structure, extent of crystallinity, and the method of film formation.

Nylon is a semi-crystalline polymer consisting of amorphous regions and regions of high crystallinity created by hydrogen bonding between polar groups on adjacent chains. The amine groups near the surface in the amorphous regions may be randomly oriented, but those in regions of high crystallinity may have some degree of ordering. However this ordering itself may differ depending on the crystalline structure. In both the major crystalline forms of nylon reported (α and γ)[70–72] hydrogen bonding occurs between the carbonyl and amine group, but the orientation of the amine with respect to the methylene groups differs. For hydrogen bonding between anti-parallel fully extended polymer chains (α crystalline form), the amide group is in the same plane as the methylene groups; in the γ form, hydrogen bonds are formed between parallel pleated chains and the amide groups are almost perpendicular to the methylene groups. Additional crystalline phases intermediate in structure to the α and γ forms have also been reported, with different hydrogen bonding patterns and chain conformations.[70-72] Furthermore the lamella of crystalline portions of the film are connected by loops which can extend from the surface[72] also yielding the potential for variation in the orientation of surface amine groups.

The method of film preparation can also have a significant influence on the extent of crystallinity and orientation of amine groups on the nylon surface. In packaging applications nylon films are typically produced by casting or blowing films. Besides mechanical stresses inducing film orientation, the cooling rate in these processes can also affect the extent of crystallinity; rapid cooling tends to produce amorphous films and faster cooling rates yield more crystalline films. Highly oriented polyamide film can be produced by extrusion and rapid quenching, followed by reheating and either uniaxial or biaxial stretching; alignment of the polymer chains is achieved by

this approach[73] and thus orientation of surface groups. Therefore the extent of crystallinity of the polymer and the method of film preparation can be expected to play significant roles in the surface orientation of amine groups in nylon films.

In this study, nylon films were prepared on silica substrates by spin-coating from an organic solvent (*m*-cresol). It is known that spin-coating polymers from solution can influence the orientation of molecular species at the surface. For example, the surface molecular structure of spin-coated polymers containing phenyl groups (polyphenylmethacylate, polysulfone, polybenzylmethacrylate, polybisphenol A carbonate) was reported to be affected both by polymer molecular structure and by casting solvent.[74] Polymers with phenyl groups in more mobile side chains produced films with high coverage of surface phenyl groups, presumably due to ability of side-chain reorientation during the rapid solvent evaporation phase of spin-coating. Polymers with less mobile phenyl functionality incorporated into the polymer backbone resulted in films with phenyl group orientation perpendicular to the surface for aromatic solvents, but the phenyl groups were oriented randomly or parallel to the surface when non-aromatic solvents were used.

Similarly the importance of casting solvent and solvent removal method on the surface structure of polymers such as poly(methyl methacrylate) has also been reported.[75] SFG and contact angle goniometry studies showed that cast films of these polymers had equilibrium surface conformations with orientation of methylene groups in the surface plane in a well-ordered structure. Spin-coated films showed an additional dependence of chain entanglement on the ratio of methylene to ester methyl groups on the polymer surface, since entanglements may inhibit the rapidity of polymer chain re-conformation needed to achieve an equilibrium configurations during solvent evaporation.

Since the method used to prepare the nylon surface was not designed to provide an oriented surface and the extent of crystallinity of the nylon was not controlled in this study, it is not unexpected that a random orientation of anhydride carbonyl groups was observed for EOgMAH films on spin-coated nylon surfaces. Further investigations using film preparation methods to produce surfaces of known amine orientation would be useful in the future to fully understand how the anhydride group of the grafted polymer interacts with the amine.

4.2.4. Adhesion Property of Polyethylene at Different Interfaces

The adhesion strengths were determined for grafted and ungrafted polyethylene at silica and nylon interfaces. The trends are shown in graphical form in Figure 4-11.

As expected there is lower adhesion of ungrafted polyethylene films to polar surfaces such as nylon than for ungrafted polyethylene films. Also, as expected, grafting MAH groups onto the polyethylene backbone improves the adhesion to both nylon and silica surfaces. Furthermore, the best adhesion was observed for grafted polyethylene on silica surface, where the C=O groups appear to be ordered at the interface. The silica surface is likely to have pendant silanol groups, which may show sufficient mobility to react with the maleic anhydride and form a bond which increases adhesion and promotes ordering as shown in Figure 4-10b above. While C=O groups are not observed at the grafted polyethylene/nylon interface, these samples still showed improved adhesion compared to ungrafted polyethylene (though not as high as adhesion of grafted polyethylene to silica). It is known the maleic anhydride group will ring open in typical packaging applications using multi-layer films, and forms covalent bonds with nylon. In this study there is no spectroscopic evidence of bonding between the maleic anhydride and nylon, since the low graft levels precluded detection of bonding-related wavelength shifts. Nevertheless it is concluded that

the presence of MAH grafting does improve adhesion to both silica and nylonsurfaces, and it is hypothesized that ordered C=O groups at the interface improve polyethylene adhesion. It is also noted that the best adhesion is observed when the methylene groups in polyethylene lie in the plane of the interface, rather than out of the plane (standing up). While it is known that the presence of methyl groups at the interface is usually detrimental to adhesion,[14,15] the detection of apparent methyl groups at both the silica and nylon interfaces does not seem a dominant effect and good adhesion can be achieved.[14,15]

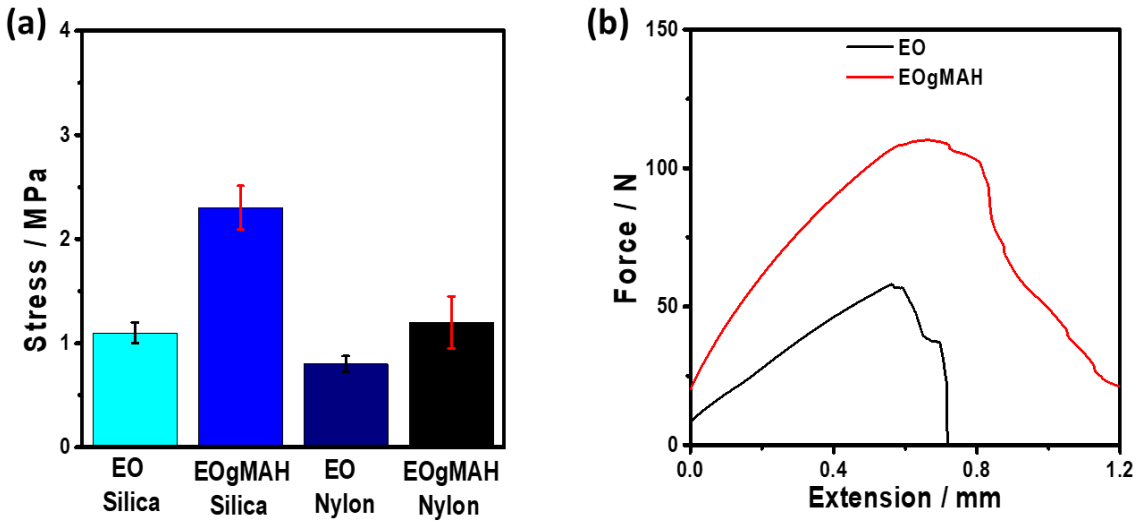

Figure 4-11 (a) Adhesion strength data measured (with the same PE film thickness) from the PE/silica and PE/nylon interfaces; (b) Typical strain-stress curves of EO and EOgMAH measured during adhesion failure at PE/silica interface;

4.3. Conclusion

	EO/silica	EOgMAH/silica	EO/nylon	EOgMAH/nylon
Adhesion strength (MPa)	1.1±0.1	2.3±0.2	0.8±0.1	1.2±0.3
Methylene Group	Yes	Yes	Yes	Yes
Methylene orientation	Lying down 90°	Tilting 75°	Upright 30°	Upright 45°
Methyl	No	Yes	No	Yes
MAH	No	Yes, ordered	No	Disordered

Table 4-6 Summary of adhesion properties and interfacial environments at different PE/silica and PE/nylon interfaces

To summarize the insights obtained on the molecular structures and chemical groups present at the buried silica and nylon interfaces with grafted and ungrafted polyethylene polymers, we can see:

1) Silica interfaces: EO and EOgMAH have different chemical compositions and different methylene structures at silica interfaces. For ungrafted polyethylene, the silica interface is dominated by polyethylene methylene groups, while for grafted polyethylene the silica interface shows substantial contributions from methyl groups (and/or gauch methylene chains) in addition to methylene groups. The methylene groups of EOgMAH tilt more toward the surface normal (stand up from the surface) compared to ungrafted polyethylene. In addition, ordered C=O groups were observed for grafted polyethylene at the silica interface.

2) Nylon interfaces: EO and EOgMAH have different chemical compositions and structures at nylon interfaces. Again the EO/nylon interface is dominated by the methylene groups, but nylon interfaces with grafted polyethylene have contributions from methyl and methylene groups. In this

case the methylene groups of both grafted and ungrafted polyethylene stand up more compared to polymer silica interfaces. Furthermore C=O groups observed from grafted polyethylene are apparently randomly ordered at nylon interfaces, in contrast to the ordering observed at silica interfaces.

The molecular compositions and orientations of grafted and ungrafted polyethylene films were determined at both silica and nylon buried interfaces using the unique spectroscopic probe SFG. Methylene groups from the polyethylene were observed at the interfaces for both grafted and ungrafted polymers, as well as strong evidence of methyl containing species (perhaps additives) at both interfaces for grafted polyethylene films. The introduction of MAH grafting to the polyethylene improves the adhesion to both hydrophilic (silica) and hydrophobic (nylon) interfaces, and ordered C=O groups are detected at the silica interface. MAH grafting improved the adhesion to nylon to a somewhat lesser degree and no C=O bonds were observed at the interface. This means either no C=O groups are present at the interface or they are at the interface and are disordered; the latter explanation is more likely considering the observed improvement in adhesion. It is however hypothesized that ordering of the C=O groups at the interface improves polyethylene adhesion.

MAH grafting also influences the orientation of the methylene groups at the interface and may play a role in the adhesion mechanism. The best adhesion is observed when the methylene groups in polyethylene lie in the plane of the interface, rather than out of the plane (standing up). The presence of methyl groups at the interface was observed here and though previously thought to decrease adhesion in some polymeric systems, to the contrary methyl groups do not seem to significantly degrade adhesion of the systems reported here. The insights gained here on the

relationship of interfacial molecular structure and adhesion will be leveraged to continue to design new polymers with improved adhesion to dissimilar surfaces.

4.4. Reference

(1) de Abreu, D. P.; Losada, P. P.; Angulo, I.; Cruz, J. *European Polymer Journal* **2007**, *43*, 2229.

(2) Robertson, G. L. *Food packaging: principles and practice*; CRC press, 2016.

(3) Appendini, P.; Hotchkiss, J. H. *Innovative Food Science & Emerging Technologies* **2002**, *3*, 113.

(4) Palmans, A. R.; Eglin, M.; Montali, A.; Weder, C.; Smith, P. *Chemistry of Materials* **2000**, *12*, 472.

(5) Rodríguez-Pérez, M. *Crosslinking in Materials Science* **2005**, 97.

(6) Alexander, M.; Zhou, X.; Thompson, G.; Duc, T.; McAlpine, E.; Tielsch, B. *Surface and interface analysis* **2000**, *30*, 16.

(7) Lapique, F.; Redford, K. *International journal of adhesion and adhesives* **2002**, *22*, 337.

(8) Brewis, D.; Briggs, D. *Polymer* **1981**, *22*, 7.

(9) Rieth, L. R.; Eaton, R. F.; Coates, G. W. *Angewandte Chemie International Edition* **2001**, *40*, 2153.

(10) Van Ooij, W.; Kleinhesselink, A.; Leyenaar, S. *Surface Science* **1979**, *89*, 165.

(11) Yamanaka, K.; Inoue, T. *Polymer* **1989**, *30*, 662.

(12) Ryschenkow, G.; Arribart, H. *The Journal of Adhesion* **1996**, *58*, 143.

(13) Ulrich, N. W.; Myers, J. N.; Chen, Z. *RSC Advances* **2015**, *5*, 105622.

(14) Zhang, C.; Myers, J. N.; Chen, Z. *Langmuir* **2014**, *30*, 12541.

(15) Zhang, C.; Hankett, J.; Chen, Z. *ACS applied materials & interfaces* **2012**, *4*, 3730.

(16) Ulrich, N. W.; Andre, J.; Williamson, J.; Lee, K.-W.; Chen, Z. *Physical Chemistry Chemical Physics* **2017**, *19*, 12144.

(17) Zhang, C.; Myers, J. N.; Chen, Z. *Soft Matter* **2013**, *9*, 4738.

(18) Chen, Z. *Progress in polymer science* **2010**, *35*, 1376.

(19) Chen, Z.; Shen, Y.; Somorjai, G. A. *Annual review of physical chemistry* **2002**, *53*, 437.

(20) Xiao, M.; Joglekar, S.; Zhang, X.; Jasensky, J.; Ma, J.; Cui, Q.; Guo, L. J.; Chen, Z. *Journal of the American Chemical Society* **2017**, *139*, 3378.

(21) Xiao, M.; Zhang, X.; Bryan, Z. J.; Jasensky, J.; McNeil, A. J.; Chen, Z. *Langmuir* **2015**, *31*, 5050.

(22) Xiao, M.; Jasensky, J.; Zhang, X.; Li, Y.; Pichan, C.; Lu, X.; Chen, Z. *Physical Chemistry Chemical Physics* **2016**, *18*, 22089.

(23) Zhang, X.; Myers, J. N.; Huang, H.; Shobha, H.; Chen, Z.; Grill, A. *Journal of Applied Physics* **2016**, *119*, 084101.

(24) Lu, X.; Li, D.; Kristalyn, C. B.; Han, J.; Shephard, N.; Rhodes, S.; Xue, G.; Chen, Z. *Macromolecules* **2009**, *42*, 9052.

(25) Lu, X.; Myers, J. N.; Chen, Z. *Langmuir* **2014**, *30*, 9418.

(26) Lu, X.; Shephard, N.; Han, J.; Xue, G.; Chen, Z. *Macromolecules* **2008**, *41*, 8770.
(27) Lu, X.; Zhang, C.; Ulrich, N.; Xiao, M.; Ma, Y. H.; Chen, Z. *Anal Chem* **2017**, *89*, 466.
(28) Tse, M. F. *Journal of Applied Polymer Science* **2014**, *131*.
(29) Liang, G.; Xu, J.; Bao, S.; Xu, W. *Journal of Applied Polymer Science* **2004**, *91*, 3974.
(30) Hasegawa, N.; Kawasumi, M.; Kato, M.; Usuki, A.; Okada, A. *Journal of Applied Polymer Science* **1998**, *67*, 87.
(31) Gaylord, N. G.; Mehta, M. *Journal of Polymer Science: Polymer Letters Edition* **1982**, *20*, 481.
(32) Wang, J.; Chen, C.; Buck, S. M.; Chen, Z. *The Journal of Physical Chemistry B* **2001**, *105*, 12118.
(33) Shen, Y. *Nature* **1989**, *337*, 519.
(34) Okur, H. I.; Kherb, J.; Cremer, P. S. *Journal of the American Chemical Society* **2013**, *135*, 5062.
(35) Shen, Y. *Annual Review of Physical Chemistry* **1989**, *40*, 327.
(36) Eisenthal, K. *Chemical Reviews* **1996**, *96*, 1343.
(37) Richmond, G. *Chemical Reviews* **2002**, *102*, 2693.
(38) Geiger, F. M. *Annual review of physical chemistry* **2009**, *60*, 61.
(39) Roy, S.; Covert, P. A.; FitzGerald, W. R.; Hore, D. K. *Chemical reviews* **2014**, *114*, 8388.
(40) Zhu, H.; Jha, K. C.; Bhatta, R. S.; Tsige, M.; Dhinojwala, A. *Langmuir* **2014**, *30*, 11609.
(41) Li, Q.; Hua, R.; Cheah, I. J.; Chou, K. C. *The Journal of Physical Chemistry B* **2008**, *112*, 694.
(42) Wang, J.; Clarke, M. L.; Chen, Z. *Analytical chemistry* **2004**, *76*, 2159.
(43) Tian, K.; Zhang, B.; Ye, S.; Luo, Y. *The Journal of Physical Chemistry C* **2015**, *119*, 16587.
(44) Yu, T.; Zhou, G.; Hu, X.; Ye, S. *Langmuir* **2016**, *32*, 11681.
(45) Dhar, P.; Khlyabich, P. P.; Burkhart, B.; Roberts, S. T.; Malyk, S.; Thompson, B. C.; Benderskii, A. V. *The Journal of Physical Chemistry C* **2013**, *117*, 15213.
(46) Dutta, C.; Benderskii, A. V. *The journal of physical chemistry letters* **2017**, *8*, 801.
(47) Saito, K.; Peng, Q.; Qiao, L.; Wang, L.; Joutsuka, T.; Ishiyama, T.; Ye, S.; Morita, A. *Physical Chemistry Chemical Physics* **2017**, *19*, 8941.
(48) Calchera, A. R.; Curtis, A. D.; Patterson, J. E. *ACS applied materials & interfaces* **2012**, *4*, 3493.
(49) Sohrabpour, Z.; Kearns, P. M.; Massari, A. M. *The Journal of Physical Chemistry C* **2016**, *120*, 1666.
(50) Lovering, K. A.; Bertram, A. K.; Chou, K. C. *The Journal of Physical Chemistry Letters* **2017**, *8*, 871.
(51) Hu, D.; Chou, K. C. *Journal of the American Chemical Society* **2014**, *136*, 15114.
(52) Sugimoto, S.; Inutsuka, M.; Kawaguchi, D.; Tanaka, K. *ACS Macro Letters* **2017**, 85.
(53) Itagaki, N.; Oda, Y.; Hirata, T.; Nguyen, H. K.; Kawaguchi, D.; Matsuno, H.; Tanaka, K. *Langmuir* **2017**, *33*, 14332.

(54) Dhar, P.; Plymale, N. T.; Malyk, S.; Lewis, N. S.; Benderskii, A. V. *The Journal of Physical Chemistry C* **2017**, *121*, 16872.
(55) Hu, X.; Tan, J.; Ye, S. *The Journal of Physical Chemistry C* **2017**, *121*, 15181.
(56) Tan, J.; Zhang, B.; Luo, Y.; Ye, S. *Angewandte Chemie* **2017**, *129*, 13157.
(57) Yang, W.-C.; Hore, D. K. *The Journal of Physical Chemistry C* **2017**, *121*, 28043.
(58) Jarisz, T. A.; Jena, K. C.; Dixon, M. C.; Hore, D. K. *The Journal of Physical Chemistry C* **2017**, *121*, 16879.
(59) Horowitz, Y.; Han, H.-L.; Ross, P. N.; Somorjai, G. A. *Journal of the American Chemical Society* **2016**, *138*, 726.
(60) Kennedy, G.; Melaet, G.; Han, H.-L.; Ralston, W. T.; Somorjai, G. A. *ACS Catalysis* **2016**, *6*, 7140.
(61) Hirose, C.; Akamatsu, N.; Domen, K. *Applied Spectroscopy* **1992**, *46*, 1051.
(62) Boughton, A. P.; Yang, P.; Tesmer, V. M.; Ding, B.; Tesmer, J. J.; Chen, Z. *Proceedings of the National Academy of Sciences* **2011**, *108*, E667.
(63) Zhang, C.; Chen, Z. *The Journal of Physical Chemistry C* **2013**, *117*, 3903.
(64) Zhang, D.; Shen, Y.; Somorjai, G. A. *Chemical Physics Letters* **1997**, *281*, 394.
(65) Zhang, D.; Shen, Y. R.; Somorjai, G. A. *Chemical Physics Letters* **1997**, *281*, 394.
(66) Novák, I.; Borsig, E.; Hrčková, L. u.; Fiedlerová, A.; Kleinová, A.; Pollák, V. *Polymer Engineering & Science* **2007**, *47*, 1207.
(67) Tse, M. F.; Hu, W.; Yeganeh, M. S.; Zhang, D. *Journal of Applied Polymer Science* **2004**, *93*, 323.
(68) Bikiaris, D. N.; Vassiliou, A.; Pavlidou, E.; Karayannidis, G. P. *European Polymer Journal* **2005**, *41*, 1965.
(69) Bula, K.; Jesionowski, T. *Composite Interfaces* **2010**, *17*, 603.
(70) Holmes, D. R.; Bunn, C. W.; Smith, D. J. *Journal of Polymer Science* **1955**, *17*, 159.
(71) Murthy, N. *Polym Commun* **1991**, *32*, 301.
(72) Li, Y.; Goddard, W. A. *Macromolecules* **2002**, *35*, 8440.
(73) Sibilia, J. P. *Journal of Polymer Science Part A-2: Polymer Physics* **1971**, *9*, 27.
(74) Myers, J. N.; Zhang, C.; Chen, C.; Chen, Z. *Journal of Colloid and Interface Science* **2014**, *423*, 60.
(75) Xu, J.; Liu, Y.; He, J.; Zhang, R.; Zuo, B.; Wang, X. *Soft Matter* **2014**, *10*, 8992.

CHAPTER 5 Application Of Multimodal SFG System To Study Complex Interfaces

Materials covered in this chapter were published in *Chem. Sci.*, **2018**, 9, 1789 and *Langmuir*, **2018**, 34, 2057. This research was in collaboration with Prof. Charles Brooks' group and Prof. Kenichi Kuroda's group.

5.1. Background and Motivation

In the above chapters, SFG has been shown to be a powerful technique to study complicated surfaces and interfaces. However, majority of the systems studied by SFG have homogeneous surfaces and interfaces (e.g., surfaces and interfaces of polymer thin films and polymer brushes, water/oxide interfaces, and chemically immobilized proteins/peptides etc.). In this chapter, a microscope-SFG platform will be introduced along with two application. Both the abilities to study heterogeneous samples and to test functions of interfacial molecules *in situ* of this analytical platform will be demonstrated.

Details about the Microscope-SFG setup have been published previously.[1] Briefly, to allow enough working space for an optical microscopic system, an "inverted" total internal reflection SFG sample geometry was used in this study (Figure 5-1a). Both the visible (532nm) and tunable infrared (IR) beams were spatially and temporally overlapped onto the prism surface using two

CaF_2 lenses. A right angle CaF_2 prism substrate was placed on a three-axis translational stage: both positions on the x-y plane and the height of the sample can be fine-tuned. The optical microscopic system was sitting above the prism substrate to allow visual monitoring of the sample and the laser spot (for SFG signal detection) *in situ*. A 40x objective and a telescope were used to magnify the image onto a CCD camera. While keeping the optical microscope stationary, the three-axis translational stage mentioned above allowed full freedom to move the sample to find an ideal position for data collection. The microscope can also be used to collect fluorescence image, which can be used to test functions of molecules at interfaces. Here the system was used to identify dead bacteria at the interface killed by the surface immobilized antimicrobial peptides.

5.2. Interaction Mechanism between Single Layered MoS_2 and Biological Molecules

5.2.1. Locating Mechanically Exfoliated Single Layered MoS_2 via Microscope-SFG

Using AFM, we determined the location of a monolayer MoS_2 with the help of neighboring thick multilayered MoS_2 regions (Figure 5-1). Such a location of the monolayer MoS_2 could be identified using the microscope-SFG with the help of the multilayered MoS_2 regions. Then both the visible and infrared beams were focused onto this region to collect SFG spectra (Figure 5-1). Structural information such as molecular orientation of surface peptides on a single layer MoS_2 could then be measured via SFG.

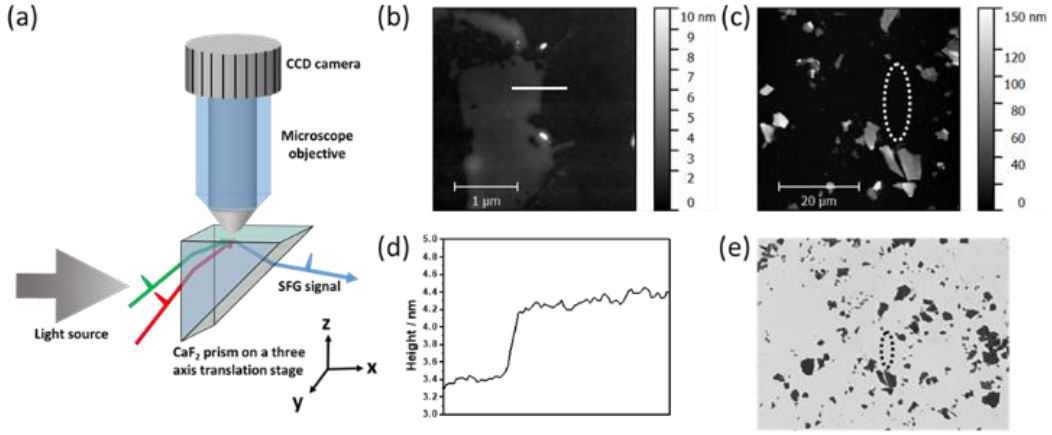

Figure 5-1 (a) Schematic of the optical microscope-SFG setup; (b-c) AFM images of mechanically exfoliated MoS_2 flakes with different magnifications. (d) Thickness measured by AFM indicates that the MoS_2 flake in (b) is a monolayer. (e) Optical image of MoS_2 on a CaF_2 prism surface (The circle is the focus of the visible beam for SFG data collection). According to the positions of the multilayered MoS_2 flakes below the circle in AFM (c) and optical (e) images, we can identify the monolayer MoS_2 sample in the circle.

5.2.2. Elucidating Interaction Mechanism between Single Layered MoS_2 and Alpha-Helical Peptide *via* Site-Specific Mutation

The sequence of a native cecropin-melittin hybrid peptide is shown in Figure 5-2, where charged, hydroxyl group containing, hydrocarbon side chain containing, and aromatic ring containing amino acids are labeled in red (most hydrophilic), blue (hydrophilic), black (hydrophobic), and green (most hydrophobic) respectively.[2]

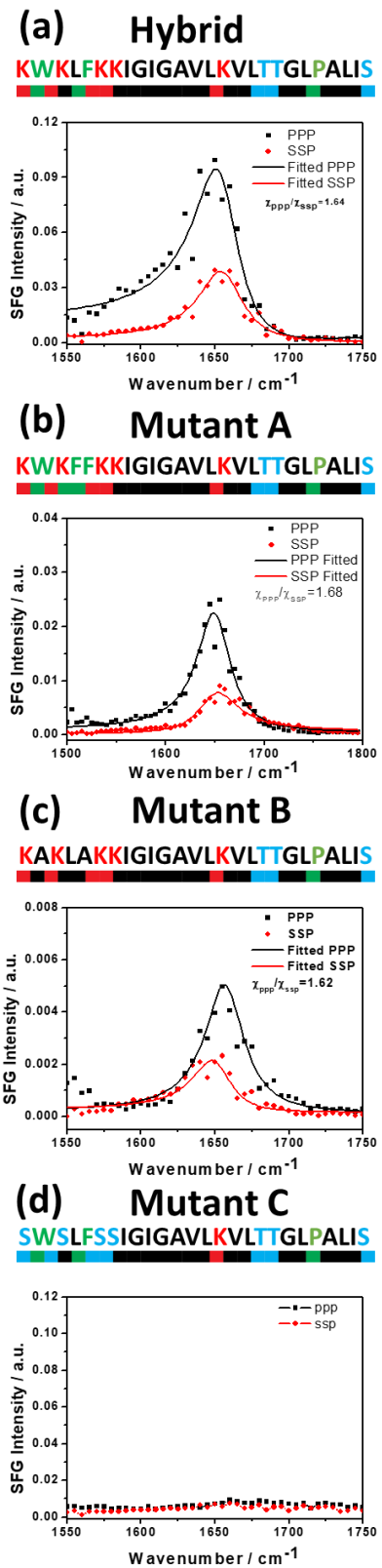

Figure 5-2 Primary sequence of the native cercropin-melittin hybrid peptide (a), mutant A

(b), mutant B (c) and mutant C (d). SFG spectra collected from the interface between MoS_2 and solutions of wild-type cecropin-melittin hybrid peptide (a), mutant A (b), mutant B (c) and mutant C (d).

SFG ssp (s-polarized signal, s-polarized input visible, p-polarized input IR beams) and ppp spectra were collected from single layer MoS_2/hybrid peptide solution interface (Figure 5-2a). Because no SFG signal could be detected from the bare CaF_2/peptide solution interface (not shown), such signals must be contributed from the peptides on MoS_2. Both SFG spectra exhibit a distinct 1650 cm^{-1} amide I peak, indicating that hybrid peptide adopts an alpha-helical secondary structure on the MoS_2 surface, with a non-parallel orientation. According to the ssp and ppp SFG amide I spectra, the orientation of the adsorbed hybrid peptide on MoS_2 was determined to be 15 to 25 degrees for the alpha helix vs. the surface normal using the method published previously (Figure 5-3).[3]

To better understand the interaction this cecropin-melittin hybrid peptide has with MoS_2, we performed molecular dynamics simulations. Simulation results showed that the C-terminus of this peptide readily interacted with MoS_2 and the remaining residues that

were solvent accessible were at a calculated tilt angle of 20.9° from the surface normal (Figure 5-4, agreeing with the experimental data quite well.

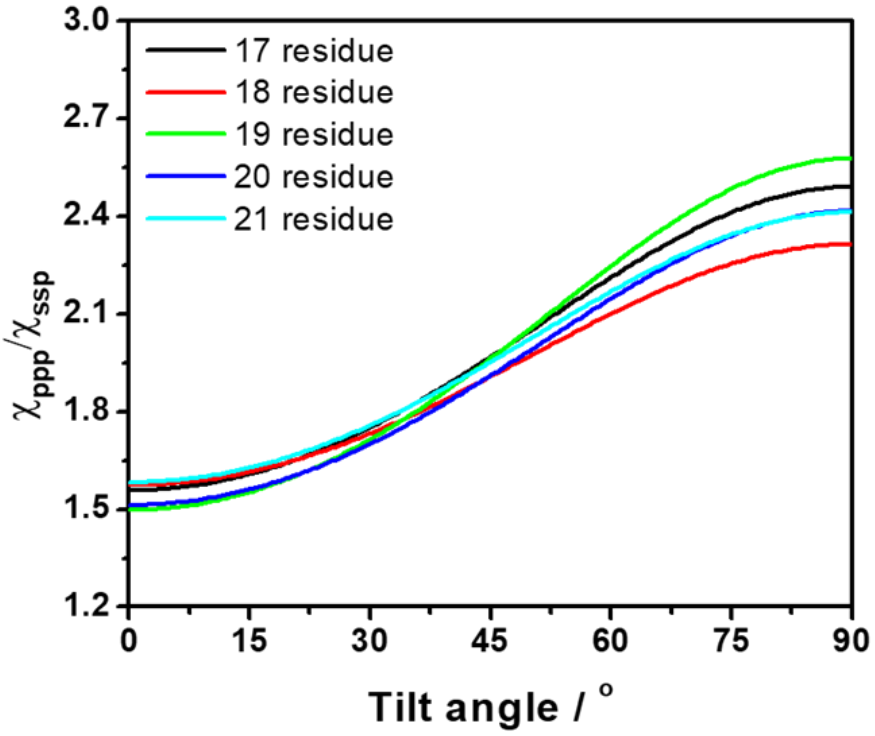

Figure 5-3 Dependence of the tilt angle on the measured SFG signal strength χ_{ppp}/χ_{ssp} ratio for several different lengths of alpha-helical peptide (17-21 residues).

A cecropin-melittin hybrid peptide has nine amino acid residues in the C-terminus region including one aromatic group containing residue, five non-aromatic hydrophobic groups, and three hydroxyl containing hydrophilic residues. The N-terminus region of the cecropin-melittin hybrid peptide has two aromatic containing amino acids, three hydrophobic (non-aromatic containing) residues, and four charged residues. The N-terminus has one more aromatic functionality containing residue. If the aromatic group containing amino acid played the dominant role in surface-peptide interaction as previously

reported for graphene,[13] the peptide should interact with the MoS_2 surface with its N-terminus. But this was not what was observed in our molecular dynamics simulations: our simulation data indicated that the C-terminus was interacting with the MoS_2 surface. We therefore believe that the aromatic amino acid/surface interaction did not play the major role for peptide/MoS_2 interaction. Instead, the general hydrophobic interactions play the major role: N-terminus is more hydrophilic because of its more charged groups, and therefore prefers to stay in the aqueous environment rather than on the surface. The C-terminus has overall more hydrophobic groups, which leads to the adsorption of C-terminus on the surface.

To further understand the peptide-MoS_2 physio-adsorption process, we designed three cecropin-melittin hybrid peptide mutants (Figure 5-2) and studied their interactions with the MoS_2 surface. For all three mutants, only the N-terminus of the peptide was modified which was previously identified as primarily driven into solution for MoS_2 interactions. Mutant A has one extra aromatic residue at the N-terminus. The goal of using this mutant is to examine whether one additional aromatic residue could increase the interaction with MoS_2 to change the peptide orientation to a lying-down pose, as previously observed in peptide-graphene interaction.[13] SFG amide I signals were successfully detected from mutant A on MoS_2 surface (Figure 5-2b), indicating a nonparallel pose in α-helical conformation, which matched the MD simulation data (Figure 5-4b). The simulation results again indicated that the C-terminus binds to the MoS_2 surface, while the N-terminus points away from the MoS_2 surface into the solution. Both the SFG experimental ratio and the simulation data showed an almost identical orientation of mutant A compared to the native

hybrid peptide, showing no strong interaction between the mutant A N-terminus (with one extra aromatic residue) and MoS_2.

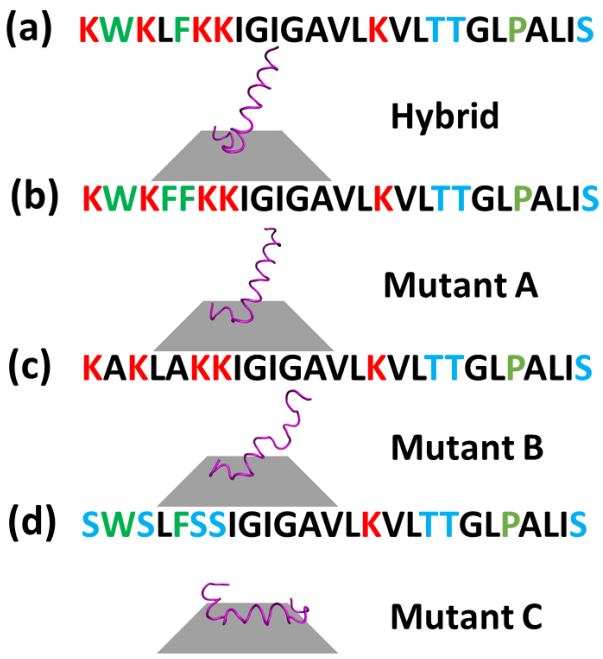

Figure 5-4 (a-d) Simulation results of cecropin-melittin hybrid peptide, mutant A, mutant B and mutant C on an MoS_2 surface.

The above study on mutant A indicated that likely the aromatic amino acid–MoS_2 interaction is not stronger than the nonaromatic amino acid–MoS_2 interaction. We want to know whether this is true vice versa and see whether the replacement of the aromatic amino acids with nonaromatic hydrophobic residues affects the peptide/MoS_2 interaction. Here the aromatic residues were all mutated to non-aromatic hydrophobic groups near the N-terminus in mutant B. SFG spectra were successfully collected from the mutant B on MoS_2

(Figure 5-2c); its orientation was measured to be 15° to 25° versus the surface normal as well, similar to that deduced from the MD simulation results (α-helix with a tilt angle of 29.7°, Figure 5-4c) and also similar to the case of the wild-type peptide presented above. The similar structure of mutant B on MoS_2 to that of wild type hybrid indicated that the

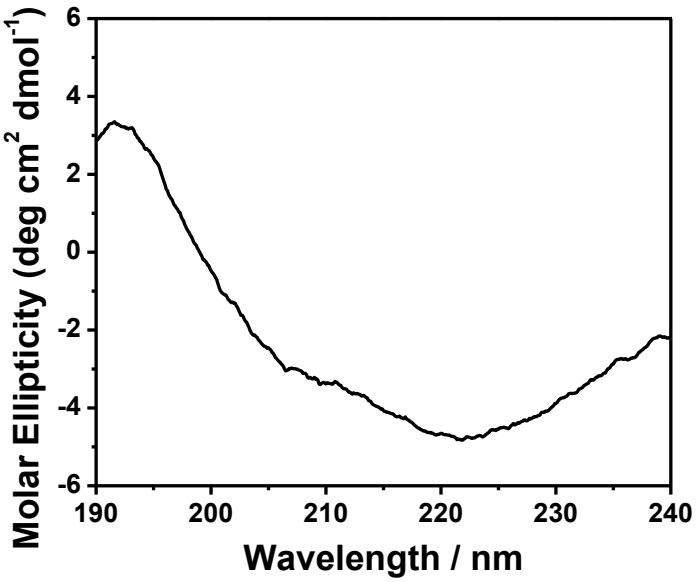

amino acids with nonaromatic functional groups do not interact with the MoS_2 surface greater than the aromatic hydrophobic amino acids.

Figure 5-5 CD spectrum of mutant C on MoS_2

We then studied the effect of charged amino acids on N-terminus by replacing charged residues with serine (mutant C). If the hydrophilic hydroxyl groups interact with water less favorably than charged residues, mutant C might lie down on the surface. Indeed, no discernable SFG amide I signal could be detected from the interface between MoS_2 and the mutant C solution. The absence of SFG signal could be because (1) no peptide was adsorbed onto the MoS_2 surface, or (2) all adsorbed peptides were lying down. To differentiate between these two possibilities, circular dichroism (CD) spectroscopy, sensitive to only

secondary structure and not orientation, was used. CD data demonstrated that mutant C was present on the MoS_2 surface with an alpha helical secondary structure (Figure 5-5). Above finding was also validated by molecular dynamics simulation (Figure 5-4d).

	Native	Mutant A	Mutant B
Amplitude ppp	6.4.0	3.06	1.13
Wavenumber ppp	1650	1650	1657
Width ppp	21.9	20.7	16.2
Amplitude ssp	3.9	2.14	0.71
Wavenumber ssp	1650	1650	1650
Width ssp	20.1	22.1	16.0

Table 5-1 Parameters for the SFG peak fitting in Figure 5-2

5.2.3. Conclusion

In conclusion, we applied a unique analytical platform to combine an optical microscope with an SFG spectrometer to study peptide interactions that occur on heterogeneous MoS_2 surfaces. This study elucidated the detailed molecular interactions between a cecropin-melittin hybrid peptide and MoS_2 surface. We found that the aromatic amino acids do not have substantial effect on peptides interacting with MoS_2 surface. With three rationally designed peptide mutants: mutant A, B and C, more details about the peptide interactions on MoS_2 were deduced. It was found that the charged groups in the N-terminus region are needed for the peptide to more favorably interact with the aqueous environment to ensure

a “standing-up” peptide pose on MoS_2. SFG experimental results and MD simulation results showed excellent agreement, validating the conclusions obtained in this research: The wild-type hybrid peptide, mutant A, and mutant B were all able to favorably interact with MoS_2 via their C-terminus while tilting at around 20° and being solvent accessible. Mutant C, on the other hand, lay down on the MoS_2 surface completely. This fundamental research on the hybrid peptide/MoS_2 interactions lay a foundation for future investigations on the interactions between other peptides and MoS_2, providing insight into the rational design of MoS_2 based biosensors using peptides and proteins. The different mechanisms of the peptide – MoS_2 interactions elucidated in this research compared to the previously reported peptide - graphene interactions clearly indicated that it is necessary to study peptide-2D material interactions when different 2D materials were chosen for sensor design. In biosensing applications, it is necessary to control the substrate surface–active biosensing unit interactions to optimize the sensing selectivity and sensitivity. This research also further demonstrated the power of using microscope-SFG system to study heterogeneous surfaces and interfaces.

5.3. Studying Antimicrobial Mechanism of Surface Immobilized Peptides *in Situ*

5.3.1. Background and Motivation

Medical device caused healthcare associated infections (HAIs) increased rapidly in the United States, with 1.7 million cases occurred in a recent year.[4] Such infections could happen because of bacterial adherence, growth and proliferation on the surfaces of medical devices, and the contact with and implantation of such medical devices into patients’ body. One approach to

decrease the HAIs incidence is to use antimicrobial surfaces for medical devices to prevent bacteria from adhering or kill bacteria that were already adhered.[5]

Conventional antimicrobial approaches include the use of antibiotics; however, many bacteria could develop drug resistance against such traditional antibiotics. Recently extensive research has been performed to use surface immobilized antimicrobial peptides (AMPs) as antimicrobial coatings. AMPs exhibit excellent activity in bacteria killing and superior biocompatibility (not kill mammalian cells). Molecular antimicrobial mechanisms of AMPs against bacteria in free solution have been extensively studied and several modes of action of AMPs have been proposed.[6-9] It is well believed that AMPs' functions are influenced by the peptide charge, conformation, hydrophobicity and amphipathicity. However, the antimicrobial mechanisms for surface immobilized AMPs have not been studied, due to the lack of appropriate tools to probe AMP-bacteria interactions.

As discussed in the previous chapters, SFG vibrational spectroscopy is a second order nonlinear optical spectroscopy with submonolayer surface specificity.[10-27] SFG has been applied to investigate numerous surfaces and interfaces to elucidate molecular structures of many molecules such as biological molecules like peptides and proteins, polymers, and water at interfaces.[16,28-30] SFG has also been used to probe molecular structures of surface immobilized AMPs. Effects of peptide surface immobilization sites (e.g., via C- or N-terminus), chemical environments (e.g., air vs. water), immobilization strategies, and surface hydrophobicity on surface immobilized AMP conformation and orientation have been elucidated by SFG as well as supplemented molecular dynamics simulation studies.[5,31-34] However, the in-situ interactions between surface immobilized AMPs and live bacteria have not been investigated using SFG. Here,

using the microscope-SFG analytical platform with an SFG spectrometer and a fluorescence,[1,35] for the first time we monitored the AMPs' behavior on surface while interacting with live bacterial cell surfaces, and followed the antimicrobial action of peptides at the same time.

5.3.2. Materials and Methods

Antimicrobial peptide surface preparation:

Here we studied molecular interactions between surface immobilized MSI-78 and live *E. coli* cells. MSI-78 is a synthetic analogue of the most widely studied AMP family magainin 2. MSI-78 has been reported to adopt alpha helical structure upon binding to bacterial cell membranes, as well as when immobilized onto a substrate surface without any interaction with bacterial cell membranes,[5] which makes it an ideal candidate for SFG structural characterization.

The MSI-78 peptide molecules were covalently immobilized onto a self-assembled monolayer terminated with maleimide groups on a CaF_2 prism surface with silica coating. The immobilization was carried out via the thiol-maleimide linkage between the cysteine of the N-terminus cysteine modified MSI-78 peptide and the maleimide terminated SAM. The SAM was prepared on a silica surface via a two-step procedure: A silica coated (200nm) right-angle CaF_2 prism was placed in an alkyne terminated silane solution for 24 h to prepare an alkyne terminated SAM. This SAM was then immersed in a 120 mM azido-PEG3-maleimide linker solution (prepared by mixing 25 mg linker kits in 560 mL DMSO for 1 h, followed by dissolving into 20 mL pH 8.0 phosphate buffer at a concentration of 50 mM). The above reaction was catalyzed with 100 μM copper (II) and reducing agent (+)-sodium L-ascorbate in the solution for 12 hours at room

temperature. The prepared maleimide surface was then immersed in a MSI-78 peptide solution (with 1:1 TCEP premixed to break inter-peptide disulfate bond) with a concentration of 5 μM.

Bacteria activity testing:

We used the LIVE/DEAD™ BacLight™ Bacterial Viability Kits to perform the bacteria testing with *E. coli* BL21 (DE3). The dye concentration of 0.6 μL/mL of the component A and B each (five times dilution compared to the suggested amount) was used in the experiment to minimize the effect of the dyes on the bacteria activity. To allow a maximum amount of bacteria to be stained, the bacteria were stained for 15 min prior to test. The microscope-SFG experiments were performed by injecting 20 μL of the stained bacteria solution onto the right-angle CaF_2 prism with immobilized peptides. The sample was covered with a cover slit to minimize the water evaporation during the experiment.

5.3.3. Antimicrobial Mechanism of Surface Immobilized Peptide

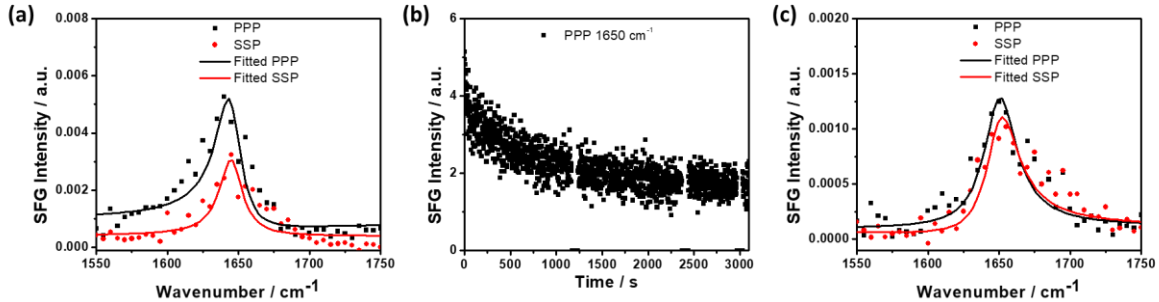

Figure 5-6 (a) SFG ppp and ssp spectra and the fitted results of surface immobilized MSI-78 in contact with water; (b) time-dependent observation of ppp signal at 1650 cm^{-1} after the surface immobilized MSI-78 in contact with E-coli solution; (c) SFG ppp and ssp spectra and fitted results

of surface immobilized MSI-78 while interacting with bacteria (collected after surface immobilized MSI-78 in contact with E-coli solution for 1 hour).

Surface immobilized AMP structure (e.g., conformation or orientation) can be probed by SFG amide I signal. It has been demonstrated that the SFG peak centered near 1650 cm^{-1} originates from alpha helical structure in peptide/protein.[30] By fitting the ssp (s-polarized SFG signal, s-polarized input visible beam, and p-polarized input IR input beam) and ppp SFG amide I signals collected from the peptides, χ_{ppp} and χ_{ssp} could be measured. By taking the χ_{ppp}/χ_{ssp} ratio, tilt angle θ of an interfacial alpha helical structure can be then deduced. (θ is defined as the angle between the surface normal and the main axis of the target alpha helical structure). Detailed correlation of alpha helical structure orientation and SFG signal strength ratio has been published previously.[3,36,37]

Figure 5-6a shows the SFG ppp and ssp amide I spectra collected from surface immobilized MSI-78 in an aqueous environment before contacting with bacteria. The deduced χ_{ppp}/χ_{ssp} ratio from the fitting results of the SFG spectra is 1.62. According to the relationship between the measured χ_{ppp}/χ_{ssp} ratio of an alpha-helical peptide and the peptide orientation, the orientation of surface immobilized MSI-78 could be determined to be around 10^{o}, indicating that the alpha helical structure of the N-terminus immobilized MSI-78 adopts a standing-up orientation on the surface. Figure 5-6b shows the time-dependent SFG ppp signal intensity observed at 1650 cm^{-1} after adding *E. coli* onto the immobilized AMP surface. The SFG time-dependent result shows that the SFG ppp signal intensity at 1650 cm^{-1} generated by the surface immobilized peptides decreased as a function of time upon contacting *E. coli*, and reached a plateau after 3000 s. Both the orientation and number of surface immobilized MSI-78 molecules could affect the observed SFG signal

intensity. Here the peptides were chemically immobilized on the SAM surface on silica; the peptide coverage on SAM was unlikely changed after bacteria contact. We therefore decided to measure the surface immobilized peptide orientation after the signal stabilized to see how the peptide-bacteria interaction could change the peptide orientation. Figure 5-6c shows the ppp and ssp spectra collected from the surface immobilized MSI-78/bacteria solution interface 3000 s after the initial peptide-bacteria solution contact. The fitted SFG results indicated that the measured χ_{ppp}/χ_{ssp} ratios for surface immobilized peptides in buffer (before bacteria contacting) and in contact with bacteria for 3000 s are markedly different (before: 1.62, after: 1.16, detailed fitting parameters listed in Table 5-2). This clearly indicated that the surface immobilized AMP had a structural (e.g., orientation) change upon contacting *E-coli* bacteria. Based on the correlation between the χ_{ppp}/χ_{ssp} ratio and the alpha helix tilt angle θ (Figure 5-3), it is impossible to find a tilt angle θ which could satisfy the measured χ_{ppp}/χ_{ssp} ratio of the surface immobilized MSI-78 after contacting *E-coli*; the ratio is lower than the lowest possible ratio in the curve. It is worth mentioning that the correlation plotted in Fig 5-3 was deduced under the delta orientation angle assumption. That is, all the MSI-78 molecules are assumed to adopt the same tilt angle. As we published previously, for a Gaussian distribution, the lowest possible χ_{ppp}/χ_{ssp} ratio is higher than that of a delta distribution. Therefore here the measured χ_{ppp}/χ_{ssp} ratio of surface immobilized MSI-78 after contacting *E-coli* could not be described by a Gaussian orientation function as well.[3]

	Width	Amplitute	Wavenumber
ppp (Fig 5-6a)	14.1	0.99	1645 cm^{-1}
ssp (Fig 5-6a)	14.0	0.68	1646 cm^{-1}
ppp (Fig 5-6c)	13.9	0.48	1650 cm^{-1}
ssp (Fig 5-6c)	14.0	0.42	1650 cm^{-1}

Table 5-2 Fitting parameters of the SFG spectra in Figure 5-6

	Width	Amplitute	Wavenumber
ppp (Fig 5-8a)	14.0	-0.51	1647 cm^{-1}
ssp (Fig 5-8b)	13.9	-0.25	1647 cm^{-1}

Table 5-3 Fitting parameters of the negative SFG peaks (blue dashed line) in Fig 5-8a and Fig 5-8b

As we published previously, such a measured ratio likely indicates a multiple orientation distribution of alpha helical peptides. For example, such a ratio may be caused by a peptide orientation distribution with two orientation angles of different absolute (up or down) orientations of alpha helical peptides.[3] Our observation here could be interpreted by the existence of two types of surface immobilized MSI-78 peptides after contacting the bacteria solution: Some of the peptides were not interacting with bacteria, therefore they adopt the original standing up pose. The rest of the peptides interacting with the bacteria could bend towards the surface. Unfortunately, it is impossible to characterize the detailed structure of the "bent" peptides after interacting with the bacteria, instead, here we assume that the peptides contacting with bacteria point to a different absolute direction. With such a picture and based on the two independent measurements (the measured ppp/ssp SFG signal strength ratio from peptides in contact with bacteria and the signal strength ratio of the SFG spectra from the peptides before and after bacteria contact) as well as the orientation of the peptides before bacteria contact, we could deduce two unknowns: (1) the ratio of the peptides not contacting vs. contacting bacteria of ~1.5 (60% not contacting, 40% contacting); (2) the orientation of the peptides in contact with bacteria: the χ_{ppp}/χ_{ssp} ratio of the second MSI-78 pose was calculated to be 2.04, showing the orientation angle is about ~110^{o} vs. the surface normal. Figure 5-8 shows the signal contributions of the two types of peptides to the overall observed

spectra collected from the surface immobilized peptide/bacteria solution interface as well as the schematic showing the peptide orientations. The fitting results of the facing down peaks are listed in Table 5-3. These spectra fitting parameters as well as formulas (will also be presented in more detail below) used for above quantitative deductions can also be found in original publication.[38] From the optical microscopic study on the bacteria deposited surface, we could observed that bacteria cover slightly less than 50% of the surface, showing that the above SFG conclusion is reasonable.

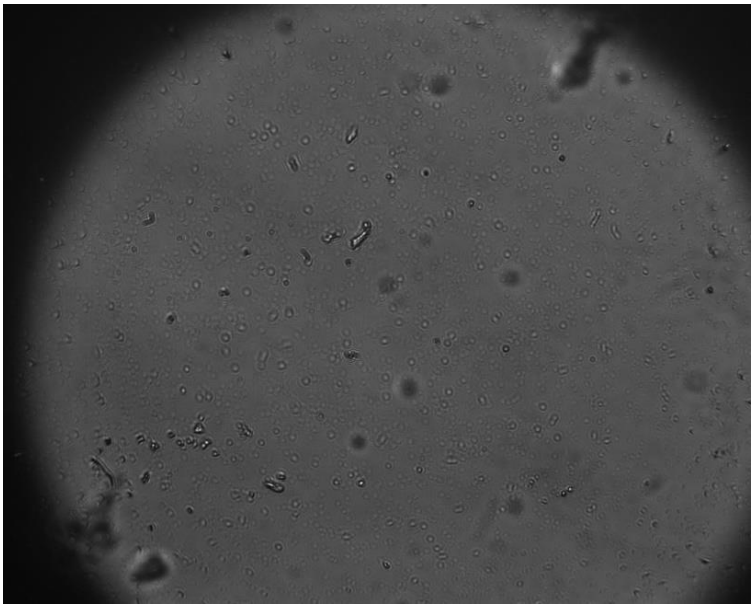

Figure 5-7 Optical image of E-coli on the surface

Here I briefly present how we could obtain the above conclusion that 60% of the surface immobilized peptides do not contact bacteria and 40% of the surface immobilized peptides contact bacteria. For an α-helical peptide, we have:

$$\chi_{yyz} = \chi_{A,yyz} + \chi_{E,yyz} = \left(\frac{1}{2}N[(1+r)\cos(\theta) - (1-r)cos^3(\theta)]\beta_{ccc}\right) + (-N(\cos(\theta) - cos^3(\theta))\beta_{aca}) \quad (5\text{-}1)$$

$$\chi_{zzz} = \chi_{A,zzz} + \chi_{E,zzz} = (N[r\cos(\theta) + (1-r)cos^3(\theta)]\beta_{ccc}) + (2N(\cos(\theta) - cos^3(\theta))\beta_{aca}) \quad (5\text{-}2)$$

Assuming that the coverage of bacteria contacting peptides is N_1 with orientation angle θ_1 (already known from the ppp/ssp signal strength ratio of the SFG spectra collected from the surface immobilized peptides in contact with buffer), then the coverage of bacteria non-contacting peptides is 1-N_1 (with orientation angle θ_2). The two unknowns are N_1 and θ_2). Based on the eqns 5-1 and 5-2, we can construct two new eqns for the measured ppp/ssp SFG signal strength ratio from peptides in contact with bacteria and the signal strength ratio of the SFG spectra from the peptides before and after bacteria contact. Therefore the two unknowns can be solved. The calculated population distribution between the two poses are 60.9% (Fig 5-8 c-1, 1-N_1)) and 39.1% (Fig 5-8 c-2, N_1), and θ_2 is 110^o.

SFG results provided insightful orientation information of the surface immobilized MSI-78 while interacting with *E-coli*. As discussed above, MSI-78 is an antimicrobial peptide. Its sequence is GIGKFLKKAKKFGKAFVKILKK, with 9 cationic lysine residues. The modes of antimicrobial actions of many AMPs free in solution have been extensively examined.[6-9] Different modes such as Barrel-stave Pore model and Toroidal Pore model in which peptides form pores in the bacteria cell membrane or Carpet Model and Detergent Model in which the AMPs adhere and lie down onto the cell membrane.[6-9] Among all different models proposed, the electrostatic force plays a vital role.[39-41] The positive charged AMPs have strong attractive forces with negatively

charged bacteria cell membrane, therefore AMPs can strongly adhere to the bacteria cell member for action.

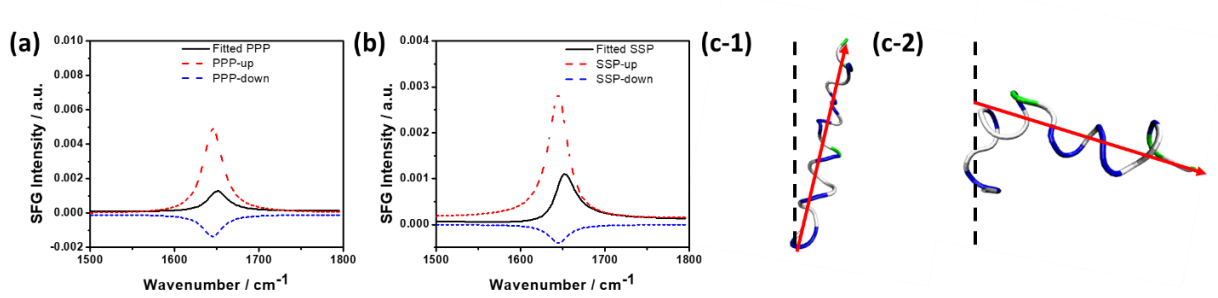

Figure 5-8 (a, b) Contributions of the PPP and SSP signals of two types of MSI-78 peptides at the surface immobilized peptides/*E-coli* solution interface. Up: from peptides not contacting with bacteria; down: from peptides contacting with peptides. (c-1,2) Schematic of orientations of the two types of surface immobilized AMPs (not contacting bacteria and contacting bacteria). Black dashed line: surface normal; red arrow: alpha helical peptide dipole direction.

The mode of action of MSI-78 in free solution has been examined and published.[42] We believe that the mode of action of MSI-78 in free solution could not be used to interpret surface immobilized peptide-bacteria interactions. The surface immobilized MSI-78 peptide has a length of 3.6 nm. Even if it stands on the surface vertically, it could not penetrate through the cell wall or outer cell membrane of bacteria. Therefore, they could not reach the bacteria inner cell membrane to form pores. For AMPs in free solution with either a Barrel-stave Pore model and a Toroidal Pore model, the ability of drilling a hole on membranes originates from AMPs' freedom in solution. Here the surface immobilized AMPs do not have such freedom, and the length of MSI-78 does not allow it to fully extend into the bacteria inner cell membrane and create a hole. Therefore, we believe that the mode of action of surface immobilized MSI-78 to kill bacteria is neither through

Barrel-stave Pore model nor through Toroidal Pore model. Instead, here the charge interaction should play a major role in bacteria killing.

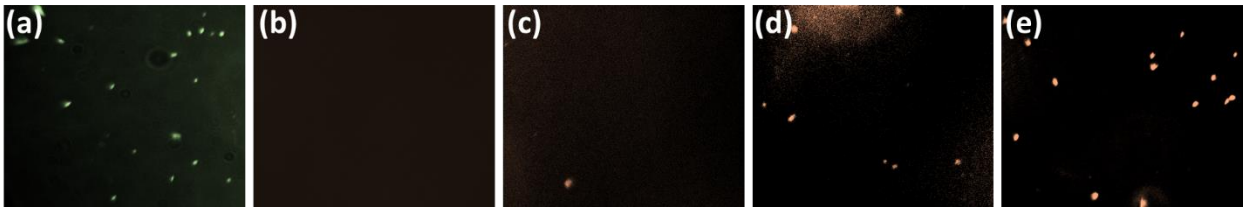

Figure 5-9 (a) Live E-coli; (b) Dead E-coli at 0min; (c) Dead E-coli at 20min; (d) Dead E-coli at 40min; (e) Dead E-coli 60min

Beside the above structure information of surface immobilized peptides while interacting with bacteria which we could extract from the SFG results, the antimicrobial behavior of surface immobilized AMP was also examined simultaneously by monitoring the *E. coli* killing process under a fluorescence microscope.

To determine bacterial cell death, the *E. coli* cells adhered on the surface were monitored in the presence of propidium iodide (PI), which can enter cells with damaged cell membranes and stain the cells by binding to DNA molecules inside the cells. Therefore, the red fluorescence signal detected from the bacterial cells reflects the disruption of the inner (cytoplasmic) membrane of these *E. coli* cells. To minimize the impact of dye molecules to the *E. coli* cells and potentially the SFG signal contribution from dye molecules, we only partially stained the *E. coli* with small amount of dye (five times dilution compared to the suggested concentration).

Figure 5-9a-e showed live *E. coli* and dead *E. coli* on surface immobilized MSI-78 at different time points. Fluorescence images showed that only very few bacteria were dead in the first 20 min. More bacteria began to die starting from 40 min, and significant number of bacteria died after 60 min. The fluorescence activity images measured show that the bacteria could be killed by the surface immobilized peptide contacting. Such contacting varied the peptide orientation, leading to SFG signal intensity decrease.

The time-dependent SFG signal change can be interpreted in two ways: (1). The bacteria attached to the surface quickly, but the bacteria killing was slow. The peptides slowly bent to kill bacteria or after the bacteria were killed, the peptides changed orientation, leading to SFG signal decrease. (2) The bacteria attached to the surface slowly, but the bacteria killing process was fast. The orientation change of peptides quickly happened when in contact with the bacteria to kill bacteria. Then the slow SFG signal time dependent change was caused by the slow adhesion rate of bacteria to the surface.

The current fluorescence assay does not provide enough evidence on differentiating the above two possibilities, but some previous studies suggested that even though factors like surface roughness, surface charge, and bacterial strain might affect adhesion of bacteria onto a surface, the overall rate of bacteria deposition onto a surface was not fast, could be hours.[43-45] Therefore we believe the above possibility (2) is better for us to use to explain the SFG time-dependent results: The bacteria slowly attached to a surface, interacting with the peptides. The peptides changed orientations and killed the bacteria due to the charged interactions.

In summary, combining SFG with fluorescent microscopy, the in-situ observation on structure and activity of surface immobilized AMPs interacting with bacteria has been achieved. Upon bacteria contact, the surface immobilized peptides changed orientation (likely to a bent structure pointing to the other direction) and kill bacteria. We believe that this is the first time to measure the structure and function of surface immobilized peptides while interacting with live bacteria in situ at the same time to understand the structure-function relationships of surface immobilized AMPs, which is important for future development of surface immobilized AMPs with improved performance.

5.4. Conclusion

In conclusion, the Microscope-SFG multimodal system was demonstrated to be a powerful platform to study heterogenous surfaces/interface and to examine interfacial molecular function in situ. Firstly, using AFM and the microscope set up in the Microscope-SFG Platform, specific areas with monolayer MoS_2 films could be located for later studies on detailed interaction mechanism between MoS_2 monolayer surface and alpha-helical peptide using SFG. Secondly, antimicrobial mechanism of surface immobilized peptides was studied by combining fluorescent imaging and SFG to probe the structure and function of the surface immobilized peptides to understand the structure-function relationships. The methodology developed in this research is general and we expect such an analytical platform to be applied to study many different surfaces and interfaces, which will greatly impact the research on heterogeneous surfaces/interfaces and structure-function relationships of surfaces/interfaces.

5.5. Reference

(1) Zhang, C.; Jasensky, J.; Leng, C.; Del Grosso, C.; Smith, G. D.; Wilker, J. J.; Chen, Z. *Optics letters* **2014**, *39*, 2715. (2) Monera, O. D.; Sereda, T. J.; Zhou, N. E.; Kay, C. M.; Hodges, R. S. *Journal of peptide science* **1995**, *1*, 319.

(3) Nguyen, K. T.; Le Clair, S. V.; Ye, S.; Chen, Z. *The Journal of Physical Chemistry B* **2009**, *113*, 12169.

(4) Vertes, A.; Hitchins, V.; Phillips, K. S. *Analytical Chemistry* **2012**, *84*, 3858.

(5) Li, Y.; Wei, S.; Wu, J.; Jasensky, J.; Xi, C.; Li, H.; Xu, Y.; Wang, Q.; Marsh, E. N. G.; Brooks, C. L.; Chen, Z. *The Journal of Physical Chemistry C* **2015**, *119*, 7146.

(6) Yeaman, M. R.; Yount, N. Y. *Pharmacological reviews* **2003**, *55*, 27.

(7) Wimley, W. C. *ACS chemical biology* **2010**, *5*, 905.

(8) Park, C. B.; Kim, H. S.; Kim, S. C. *Biochemical and biophysical research communications* **1998**, *244*, 253.

(9) Shai, Y. *Biochimica et Biophysica Acta (BBA)-Biomembranes* **1999**, *1462*, 55.

(10) Shen, Y. *Annual Review of Physical Chemistry* **1989**, *40*, 327.

(11) Shen, Y. *Nature* **1989**, *337*, 519.

(12) Chen, Z.; Shen, Y.; Somorjai, G. A. *Annual review of physical chemistry* **2002**, *53*, 437.

(13) Richmond, G. *Chemical Reviews* **2002**, *102*, 2693.

(14) Weidner, T.; Apte, J. S.; Gamble, L. J.; Castner, D. G. *Langmuir* **2009**, *26*, 3433.

(15) Roy, S.; Covert, P. A.; FitzGerald, W. R.; Hore, D. K. *Chemical reviews* **2014**, *114*, 8388.

(16) Yu, T.; Zhou, G.; Hu, X.; Ye, S. *Langmuir* **2016**, *32*, 11681.

(17) Saito, K.; Peng, Q.; Qiao, L.; Wang, L.; Joutsuka, T.; Ishiyama, T.; Ye, S.; Morita, A. *Physical Chemistry Chemical Physics* **2017**, *19*, 8941.

(18) Dhar, P.; Khlyabich, P. P.; Burkhart, B.; Roberts, S. T.; Malyk, S.; Thompson, B. C.; Benderskii, A. V. *The Journal of Physical Chemistry C* **2013**, *117*, 15213.

(19) Dutta, C.; Benderskii, A. V. *The journal of physical chemistry letters* **2017**, *8*, 801.

(20) Yan, E. C.; Fu, L.; Wang, Z.; Liu, W. *Chemical reviews* **2014**, *114*, 8471.

(21) Adhikari, N. M.; Premadasa, U. I.; Cimatu, K. L. *Physical Chemistry Chemical Physics* **2017**, *19*, 21818.

(22) Premadasa, U. I.; Adhikari, N. M.; Baral, S.; Aboelenen, A. M.; Cimatu, K. L. A. *The Journal of Physical Chemistry C* **2017**, *121*, 16888.

(23) Tan, J.; Zhang, B.; Luo, Y.; Ye, S. *Angewandte Chemie* **2017**, *129*, 13157.

(24) van der Post, S. T.; Hsieh, C. S.; Okuno, M.; Nagata, Y.; Bakker, H. J.; Bonn, M.; Hunger, J. *Nat. Commun.* **2015**, *6*, 8384.

(25) Lis, D.; Backus, E. H.; Hunger, J.; Parekh, S. H.; Bonn, M. *Science* **2014**, *344*, 1138.

(26) Okur, H. I.; Kherb, J.; Cremer, P. S. *Journal of the American Chemical Society* **2013**, *135*, 5062.

(27) Troiano, J. M.; McGeachy, A. C.; Olenick, L. L.; Fang, D.; Liang, D.; Hong, J.; Kuech, T. R.; Caudill, E. R.; Pedersen, J. A.; Cui, Q.; Geiger, F. M. *Journal of the American Chemical Society* **2017**, *139*, 5808.

(28) Xiao, M.; Joglekar, S.; Zhang, X.; Jasensky, J.; Ma, J.; Cui, Q.; Guo, L. J.; Chen, Z. *J. Am. Chem. Soc* **2017**, *139*, 3378.

(29) Hsieh, C.-S.; Okuno, M.; Hunger, J.; Backus, E. H. G.; Nagata, Y.; Bonn, M. *Angewandte Chemie International Edition* **2014**, *53*, 8146.

(30) Wang, J.; Even, M. A.; Chen, X.; Schmaier, A. H.; Waite, J. H.; Chen, Z. *Journal of the American Chemical Society* **2003**, *125*, 9914.

(31) Wei, S.; Zou, X.; Cheng, K.; Jasensky, J.; Wang, Q.; Li, Y.; Hussal, C.; Lahann, J.; Brooks III, C. L.; Chen, Z. *The Journal of Physical Chemistry C* **2016**, *120*, 19078.

(32) Wang, Q.; Wei, S.; Wu, J.; Zou, X.; Sieggreen, O.; Liu, Y.; Xi, C.; Brooks III, C. L.; Chen, Z. *The Journal of Physical Chemistry C* **2015**, *119*, 22542.

(33) Wang, Z.; Han, X.; He, N.; Chen, Z.; Brooks III, C. L. *The Journal of Physical Chemistry B* **2014**, *118*, 5670.

(34) Han, X.; Liu, Y.; Wu, F.-G.; Jansensky, J.; Kim, T.; Wang, Z.; Brooks, C. L.; Wu, J.; Xi, C.; Mello, C. M.; Chen, Z. *The Journal of Physical Chemistry B* **2014**, *118*, 2904.

(35) Zhang, C.; Jasensky, J.; Wu, J.; Chen, Z. In *SPIE BiOS*; International Society for Optics and Photonics: 2014, p 894712.

(36) Yang, P.; Boughton, A.; Homan, K. T.; Tesmer, J. J.; Chen, Z. *Journal of the American Chemical Society* **2013**, *135*, 5044.

(37) Liu, Y.; Ogorzalek, T. L.; Yang, P.; Schroeder, M. M.; Marsh, E. N. G.; Chen, Z. *Journal of the American Chemical Society* **2013**, *135*, 12660.

(38) Xiao, M.; Jasensky, J.; Foster, L.; Kuroda, K.; Chen, Z. *Langmuir* **2018**, *34*, 2057.

(39) Radzishevsky, I. S.; Rotem, S.; Bourdetsky, D.; Navon-Venezia, S.; Carmeli, Y.; Mor, A. *Nature biotechnology* **2007**, *25*, 657.

(40) Vaidyanathan, S.; Chen, J.; Orr, B. G.; Banaszak Holl, M. M. *Molecular pharmaceutics* **2016**, *13*, 1967.

(41) Vaidyanathan, S.; Orr, B. G.; Banaszak Holl, M. M. *Accounts of chemical research* **2016**, *49*, 1486.

(42) Hallock, K. J.; Lee, D.-K.; Ramamoorthy, A. *Biophysical Journal* **2003**, *84*, 3052.

(43) Mafu, A. A.; Plumety, C.; Deschênes, L.; Goulet, J. *International journal of microbiology* **2010**, *2011*.

(44) Otto, K.; Silhavy, T. J. *Proceedings of the National Academy of Sciences* **2002**, *99*, 2287.

(45) Terada, A.; Yuasa, A.; Kushimoto, T.; Tsuneda, S.; Katakai, A.; Tamada, M. *Microbiology* **2006**, *152*, 3575.

(46) Xiao, M.; Wei, S.; Li,Y.; Jasensky, J.; Chen, J.; Brooks, CL III.; Chen, Z. *Chemical Science* **2018**, *9*, 1769.

CHAPTER 6 Conclusions And Future Work

6.1. Conclusions and Future works

This thesis research successfully elucidated molecular structures of buried interfaces in many important applications, such as semiconductor polymers, solar cells, polymer adhesives, 2D materials, as well as antimicrobial coatings, and reveled the structure-function correlations of these buried interfaces. More specifically, this thesis research provided in-depth understanding on: (1) the effects of the casting solvent, dielectric layer, or semiconductor polymer sidechain on surface, bulk and interface structure of polymer based organic semiconductors;[1,2] (2) the correlation between the performance of perovskite-based photovoltaics and the molecular structures of semiconductor polymers at the polymer hole transporting layer/perovskite layer interface;[3] (3) the effects of the interfacial molecular structure on adhesion property of polyethylene based polymer adhesives at different interfaces; and (4) interactions between heterogeneous 2D material surface and biological molecules as well as antimicrobial mechanisms of surface immobilized AMPs.[4,5]

First, the solvent effect on the prepared P3HT films was systematically studied. It was discovered that using chlorobenzene (good solvent) with acetone (bad solvent) blend to prepare a semiconductor polymer P3HT film made the P3HT backbone lie down at both the polymer film surface and buried polymer/substrate interface. Besides the casting solvent, it was also found that

the P3HT backbone orientation at the P3HT film/dielectric layer could be mediated by the dielectric layer surface: the P3HT polymer backbone stands up more on a hydrophobic dielectric layer surface, and lies down more on a hydrophilic dielectric layer surface. Such a trend remained the same for a different polythiophene molecule with a side chain containing a charged end group. It is well known that in many applications of semiconductor polymer films, the surface/interfacial structure plays a dominating role. This research demonstrated that it is feasible to rationally design and control surface/interfacial structures of semiconductor polymer films by carefully choosing the casting solvent composition, substrate hydrophobicity, and polymer side chain hydrophobicity.

This research only investigated the effects of casting solvent, dielectric layer, and semiconductor polymer side chain hydrophobicity on polymer based organic semiconductors. There are many other factors that could greatly alter the performance of organic semiconductors, which have not been studied in this thesis. Such research could be performed in the future:

1. The effects of small molecule additives in the casting solvent (used for semiconductor film preparation) on the surface/interfacial structures of the prepared polymer film can be explored. For example, a lithium-based salt (LiTFSi) is known to enhance the property of solvent casted organic semiconductor films,[6] but the impact of such additives in the solvent on the semiconductor polymer film surface/interface structure has not yet been examined. SFG study in this case can provide valuable insights to the surface/interfacial structural variations of the semiconductor polymer film induced by the addition of LiTFSi to the solvent for polymer film preparation.

2. The effects of polymer film deposition rate and temperature on the molecular structures of surfaces/interfaces of polymer semiconductor films prepared by vapor deposition can be investigated. This thesis only focused on the solvent processed organic semiconductor films. The vapor-deposition based polymer semiconductors have not been discussed. For semiconductor

polymer films prepared by vapor deposition, the deposition rate and substrate temperature can greatly alter the performance of the deposited films, even the film morphology.[7] Understanding surface and interfacial molecular structures of polymer films prepared by vapor deposition and the effects of different factors on such structures could greatly improve the performance of such polymer films, aiding in the development and fabrication of high-performance organic semiconductor devices *via* vapor-deposition;

3. The composition of the polymer side chain can be further varied to gain a more in-depth understanding of the polymer side-chain effect on the surface/interfacial structures of semiconductor polymer films. Both the side-chain length and the chemical composition of the end group of the polymer side chains can be changed.

4. Other semiconductor polymers beyond PT should be studied using SFG. This thesis studied PT, one of the most widely used solvent-processed organic semiconductors. Recently, many new semiconducting conductor polymer materials with excellent performance were synthesized. For example, a better hole transporting molecule PTB7 (than PT) was reported recently[8]. With the methodology established in this thesis, further study can be carried out on new materials like PTB7 to gain a deeper understanding on the behavior of such molecules at the interface.

This thesis research also presented exciting results on the interfacial structures of semiconductor polymers used in perovskite photovoltaics. Specifically, it probed the interface between the hole transport semiconductor polymer layer and the perovskite photoactive layer. By deconvoluting SFG signals contributed from the two interfaces of a buried polymer film, interface I and interface II (see chapter 3 for details), we successfully determined the interfacial molecular structure at the interface of interest. By using PT derivatives with various side chain lengths, it was

found that a more edge on PT backbone at the HTL/perovskite interface facilitates the hole transport across the HTL/perovskite interface. We believed that a more edge on PT backbone will eventually cause a better HOMO-HOMO orbital offset between the PT and the perovskite, therefore minimized the interfacial charge recombination. This is the first time to elucidate molecular structures of buried interfaces in solar cells using SFG and correlated such interfacial structure to solar cell device performance. The research provides a general method to probe and deconvolute molecular orientations at buried interfaces in situ in thin film based photovoltaic devices.

Possible future works on this topic include:

1. Elucidation of the ETL/perovskite interface - Therefore we could gain a complete picture of the interfacial molecular structure and its correlation to the charge transportation in perovskite photovoltaics;

2. Investigation of other materials beyond the hole transport layer based polymers in solar cell applications - Recent development showed that TPB[9,10] has a great potential to serve as the electron transport layer in organic photovoltaic application. No study has been conducted on the structure of TPB at a molecular level due to its complication. SFG is a perfect technique to elucidate the molecular structure of TPB at the interfaces and correlate the performance of TPB in a working solar cell with such molecular structural information;

3. Study of surface /interfacial structures of semiconductor polymers beyond solar cell, in other devices such as organic light emitting diode (OLED) - One important topic in the OLED community is to gain a directional emission. Such a behavior of OLED molecules is strongly related to the orientation of the OLED molecules at interface (charge accumulation effect).[11]

Understanding of the correlations between the emission profile of the OLED molecules and the orientation of these molecules at interface could greatly help to improve the OLED performance by controlling the interfacial orientation.

In this thesis, besides the SFG studies on polymer semiconductors, SFG was also applied to elucidate interfacial structures of polymer-based adhesives. In collaboration with Dow Chemical, interfacial structures of two polyethylene derivatives were studied at both the PE/silica interface and PE/nylon interface. Combining with adhesion results at these interfaces, it was concluded that: (1) The same PE at different interfaces could have different dominating chemical functional groups; (2) Interfacial methyl groups decrease the interfacial adhesion strength; (3) For the same PE derivative, C=O groups induced by grafted MAH could show up or disappear at different interfaces; and (4) The more lying down the methylene groups at the interface, the stronger the adhesion strength. This research provides important knowledge on polymer adhesion by examining buried interfacial structures in situ. Previously, people separate the buried interfaces – destroy the interface – here, this method studies interface in situ, which is nondestructive, more accurate, and generally applicable.

For the future direction of this topic, the following research can be proposed:

1. It is important to explore the sample preparation temperature effect on the polymer's adhesion strength and the effects of different grafted functional groups beside MAH on adhesion

2. Other polymer adhesives based on polypropylene, epoxy, and PDMS can be examined. Methyl and methylene groups widely exist in these molecules, making SFG an ideal tool to study their interfacial structure nondestructively.[12-14]

The last topic presented in this thesis is the example applications of microscope-SFG. It was shown that the microscope-SFG platform can not only study heterogeneous surfaces such as mechanically exfoliated MoS_2 surfaces, it can also be used to monitor biological process occurred on the surface *in situ*. On a MoS_2 surface, we used the microscope-SFG to elucidate the interaction mechanism between a series of *de novo* designed alpha helical peptides and the single layered MoS_2 flakes. It was found that the charged amino acids interact with aqueous solution more favorably, while the amino acids with alkyl side-chains interact with the MoS_2 surface more favorably. This study provided a detailed interaction mechanism between biological molecules and single layered MoS_2 for the first time. Such an understanding would greatly benefit further design and fabrication of MoS_2 based biological sensing devices. In the study using the microscope-SFG to monitor the biological process, we were not only able to image the live/dead bacteria on the antimicrobial surface, but also were able to use SFG to monitor the antimicrobial peptide molecular behavior on the surface. SFG results suggest that upon contacting bacteria, surface immobilized peptides adopted an orientation change (from standing up to lying down), providing new insight to mechanism study of surface immobilized antimicrobial peptide. For the first time, such a mechanism provided by SFG showed the common and different behaviors of free AMPs in aqueous environment and surface immobilized AMPs.

Future directions:

1. Interactions between MoS_2 and more complicated biological molecules such as enzymes and other proteins can be investigated using the microscope-SFG platform.

2. Other 2D materials beyond MoS_2 and their interactions with various biological molecules can be studied. For example single layered WS_2 and black phosphorus prepared *via* mechanical exfoliation can be studied in the future.

3. Other heterogeneous surfaces/interfaces can be examined using the microscope-SFG platform – e.g., polymer blend surfaces with domains;

4. Antimicrobial mechanisms of other AMPs (cecropins, melitins etc.) immobilized on different substrates beyond SAMs (e.g., on CVD based polymer thin films) can be investigated.

5. Structure-function relations of surface immobilized enzymes, where the structure of enzymes can be studied via SFG, and the activity information of enzymes can be achieved *via* optical/fluorescence microscope, can be examined in detail.

Various topics in this thesis cover many disciplines including chemistry, materials science and engineering, physics, and biology, showing that SFG is a powerful and versatile analytical tool. It is believed that with better experimental design and advanced technical development, SFG as a unique nonlinear vibrational spectroscopic tool will play an increasingly vital role in many current and emerging research projects.

6.2. References

(1) Xiao, M.; Zhang, X.; Bryan, Z. J.; Jasensky, J.; McNeil, A. J.; Chen, Z. *Langmuir* **2015**, *31*, 5050.

(2) Xiao, M.; Jasensky, J.; Zhang, X.; Li, Y.; Pichan, C.; Lu, X.; Chen, Z. *Physical Chemistry Chemical Physics* **2016**, *18*, 22089.

(3) Xiao, M.; Joglekar, S.; Zhang, X.; Jasensky, J.; Ma, J.; Cui, Q.; Guo, L. J.; Chen, Z. *Journal of the American Chemical Society* **2017**, *139*, 3378.

(4) Xiao, M.; Wei, S.; Li, Y.; Jasensky, J.; Chen, J.; Brooks, C.; Chen, Z. *Chemical Science* **2018**, *9*, 1769.

(5) Xiao, M.; Jasensky, J.; Foster, L.; Kuroda, K.; Chen, Z. *Langmuir* **2018**, *34*, 2057.

(6) Mabrouk, S.; Bahrami, B.; Gurung, A.; Reza, K. M.; Adhikari, N.; Dubey, A.; Pathak, R.; Yang, S.; Qiao, Q. *Sustainable Energy & Fuels* **2017**, *1*, 2162.

(7) Yang, J.; Nguyen, T.-Q. *Organic Electronics* **2007**, *8*, 566.

(8) Lu, L.; Yu, L. *Advanced Materials* **2014**, *26*, 4413.

(9) Wu, Q.; Zhao, D.; Schneider, A. M.; Chen, W.; Yu, L. *Journal of the American Chemical Society* **2016**, *138*, 7248.

(10) Jung, I. H.; Zhao, D.; Jang, J.; Chen, W.; Landry, E. S.; Lu, L.; Talapin, D. V.; Yu, L. *Chemistry of Materials* **2015**, *27*, 5941.

(11) Kondakov, D. Y.; Sandifer, J. R.; Tang, C. W.; Young, R. H. *Journal of Applied Physics* **2003**, *93*, 1108.
(12) Encinas, N.; Abenojar, J.; Martínez, M. A. *International Journal of Adhesion and Adhesives* **2012**, *33*, 1.
(13) Zanni-Deffarges, M. P.; Shanahan, M. E. R. *International Journal of Adhesion and Adhesives* **1995**, *15*, 137.
(14) Jin, M.; Feng, X.; Xi, J.; Zhai, J.; Cho, K.; Feng, L.; Jiang, L. *Macromolecular Rapid Communications* **2005**, *26*, 1805.